Comparing energy and entropy formulations for cosmic ray hydrodynamics

Master Thesis

in

Astrophysics

submitted by

Matthias Weber

Supervisor:
Prof. Dr. Christoph Pfrommer

First Referee:
Prof. Dr. Christoph Pfrommer

Second Referee:
apl. Prof. Dr. Achim Feldmeier

Institute of Physics and Astronomy
University of Potsdam
August 8, 2022

Abstract

Cosmic rays (CRs) play an important role in many astrophysical systems. Acting on plasma scales to galactic environments, CRs are usually modelled as a fluid, using the CR energy density as the evolving quantity. This method comes with the flaw that the corresponding CR evolution equation is not in conservative form, as it contains an adiabatic source term that couples CRs to the thermal gas. In the absence of non-adiabatic changes, instead evolving the CR entropy density is a physically equivalent option that avoids this potential numerical inconsistency. In this work, we study both approaches for evolving CRs in the context of magneto-hydrodynamic simulations using the moving-mesh code Arepo. We investigate the performance of both methods in a sequence of shock-tube tests with various resolutions and shock Mach numbers. We find that the entropy-conserving scheme performs best for the idealized case of purely adiabatic CRs across the shock, while both approaches yield similar results at lower resolution. In this setup, both schemes operate well and almost independently of the shock Mach number. Taking active CR acceleration at the shock into account, the energy-based method proves to be numerically much more stable and significantly more accurate in determining the shock velocity, in particular at low resolution, which is more typical for astrophysical large-scale simulations. For a more realistic application, we simulate the formation of several isolated galaxies at different halo masses and find that both numerical methods yield almost identical results, with differences far below common astrophysical uncertainties.

Kurzzusammenfassung

Kosmische Strahlung (KS) spielt in vielen astrophysikalischen Systemen eine bedeutende Rolle. Da sie sowohl auf Plasmaskalen als auch auf galaktischen Maßstäben wirkt, modelliert man die KS für gewöhnlich als Fluid, wobei die Energiedichte der KS als Entwicklungsgröße verwendet wird. Diese Methodik birgt jedoch den Nachteil, dass die entsprechende Entwicklungsgleichung der KS nicht in konservativer Form vorliegt, da sie einen adiabatischen Quellterm enthält, welcher die KS mit dem thermischen Gas koppelt. In Abwesenheit nicht-adiabatischer Quellterme ist die Entwicklung der Entropiedichte der KS eine physikalisch gleichwertige Option, welche diese potenzielle numerische Inkonsistenz vermeidet. In der vorliegenden Arbeit werden beide Ansätze zur Entwicklung von KS im Rahmen von magneto-hydrodynamischen Simulationen unter Verwendung des *Moving-Mesh-Codes* Arepo untersucht. Die Leistungsfähigkeit beider Methoden wird in einer Reihe von Stoßrohr-Simulationen mit unterschiedlichen Auflösungen und Stoß-Mach-Zahlen verglichen. Das entropieerhaltende Schema liefert für den idealisierten Fall rein adiabatischer KS in der Stoßzone die besten Ergebnisse, während bei geringerer Auflösung beide Ansätze zu ähnlichen Resultaten führen. In dieser Konstellation arbeiten beide Verfahren nahezu unabhängig von der Stoß-Mach-Zahl zuverlässig. Unter Einbeziehung aktiver Beschleunigung der KS am Stoß erweist sich die energiebasierte Methode als numerisch wesentlich stabiler und erheblich genauer bei der Bestimmung der Stoßgeschwindigkeit, insbesondere bei geringer Auflösung, die für astrophysikalische Großraumsimulationen charakteristisch ist. Als realistischere Anwendung wird die Entstehung mehrerer isolierter Galaxien mit unterschiedlichen Halo-Massen simuliert. Es zeigt sich, dass beide numerischen Methoden nahezu identische Resultate liefern, deren Diskrepanzen deutlich unterhalb der üblichen astrophysikalischen Unsicherheiten liegen.

The presented results are based on Weber et al. (2022), which was submitted to MNRAS. I use the present work to give a solid theoretical background to the used arguments and to detail the numerical framework.

Contents

1 Introduction

Cosmic rays (CRs) represent the non-thermal particle population of an astrophysical plasma and arguably play a crucial role in understanding the self-regulated feedback mechanisms that are at work in galaxies and galaxy clusters (Zweibel, 2017). They acquire their high energies by diffusive acceleration processes at shocks (Marcowith et al., 2016) driven by supernovae (SNe), or by the relativistic energy feedback from active galactic nuclei (Guo and Oh, 2008; Jacob and Pfrommer, 2017a,b). Concurrently, CRs suffer non-adiabatic cooling due to radiative and Coulomb losses, scattering off of self-excited magnetic fluctuations (Kulsrud and Pearce, 1969; Shalaby et al., 2021), and hadronic collisions. While energetic CR electrons thereby cool rapidly to negligible energies, rendering them dynamically insignificant in astrophysical systems, the momentum-carrying CR protons have much longer cooling times in comparison to their leptonic counterparts or thermal gas. This results in an approximate equipartition of the thermal, magnetic, and CR pressure in the mid-plane of the Milky Way (Boulares and Cox, 1990), thus making CRs a promising agent of galactic feedback processes.

In the past decades, various approaches have been employed to numerically model the impact of CRs in astrophysical simulations. CRs act on a large range of scales, from characteristic plasma scales to galaxies to galaxy clusters. To explore CR dynamics in these macroscopic systems, the only computationally tractable approach is to model CRs collectively as a fluid. Commonly, a one-moment formulation for the CR fluid is applied in hydrodynamic and magneto-hydrodynamic (MHD) simulations (Hanasz and Lesch, 2003; Enßlin et al., 2007; Jubelgas et al., 2008; Booth et al., 2013; Salem and Bryan, 2014; Girichidis et al., 2014; Pakmor et al., 2016a; Pfrommer et al., 2017; Dubois et al., 2019), meaning that only a single scalar quantity (CR energy density or number density) is evolved in time. This setup is well suited for modelling the CR transport mechanisms of advection and diffusion. However, when applying this method to CR streaming, numerical instabilities may occur due to unlimited flux values (Sharma et al., 2009). Hence, further improvements were made by developing a two-moment formulation in which the energy and flux densities of CRs are computed separately (Jiang and Oh, 2018; Thomas and Pfrommer, 2019, 2022; Chan et al., 2019; Thomas et al., 2021). The above algorithms exclusively use a simple 'grey' approach for CR spectra, neglecting the different effects of and on CRs at different energies. To address this shortcoming, some codes were elaborated to handle spectrally resolved simulations, either using additional tracer particles (Vaidya et al., 2018; Winner et al., 2019) or by adding multiple momentum bins per hydro-cell covering a wide range of the CR spectrum (Miniati, 2001; Yang and Ruszkowski, 2017; Girichidis et al., 2020; Ogrodnik et al., 2021; Hopkins et al., 2022).

Each of the previous models uses a two-fluid approximation to describe the thermal gas and CRs individually. Usually, the time evolution of the CR energy density is added as an extra relation to the conventional set of hydrodynamic/MHD equations, which represent conservation laws for mass, momentum, and energy. As a consequence, the CR energy density does not separately follow such a conservation law. Any formulation of the CR energy density equation includes an adiabatic source term (either $P_{\rm cr}\boldsymbol{\nabla}\cdot\boldsymbol{u}$ or $\boldsymbol{u}\cdot\boldsymbol{\nabla}P_{\rm cr}$) that couples the CR pressure $P_{\rm cr}$ to the mean ve-

locity $\boldsymbol{u}$ of thermal gas. This term needs to be calculated in an additional step, thus preventing the CR equation from adopting a conservative form. While this is not a problem for smooth flows, the presence of non-vanishing spatial derivatives could in principle be problematic for shocks because a sudden jump in density/velocity could give rise to a continuous accumulation of numerical errors. This problem of non-uniqueness of the CR energy density is extensively discussed by Gupta et al. (2021).

To overcome this potential numerical flaw, alternative schemes have been developed to integrate CR physics into the simulations, based on ideas by Ryu et al. (1993). Here, rather than CR energy, a modified CR entropy density, $\rho K_{\rm cr} = P_{\rm cr}/\rho^{\gamma_{\rm cr}-1}$ with $\gamma_{\rm cr}$ the adiabatic index of the CRs, is used as the relevant quantity to describe the CR fluid (Kudoh and Hanawa, 2016; Semenov et al., 2021). This approach has the evident benefit that the CR equation is in conservative form, so that Godunov-type solvers can be straightforwardly applied. However, this formulation is only valid in the absence of non-adiabatic changes, where entropy is conserved. This is neither the case for astrophysical shocks in which CRs are accelerated, nor for radiative, hadronic, and Alfvén wave cooling. In such cases, one would have to switch back to the energy description. Furthermore, the unavoidable dependence on mass density can lead to an immediate impact of (numerical) density fluctuations on the entropy variable, particularly in regimes of low resolution, which is the default scenario in large-scale simulations. Moreover, the total energy is not explicitly conserved in such schemes.

In their detailed study, Gupta et al. (2021) state that solving the two-fluid equations across shocks generally yields unique results only when an additional CR subgrid closure is assumed, regardless of the employed numerical method. Without using such an artificial closure, they recommend adopting the energy-based method where the total energy and CR energy are evolved in an unsplit scheme and the source term is added as $P_{\rm cr}\boldsymbol{\nabla}\cdot\boldsymbol{u}$, because this approach proves to be most stable in that case. Further, they argue that the entropy-conserving scheme does not provide satisfactory results in simple stability tests. Additionally, they point out that assuming a constant CR entropy across shocks is not physically justified because CRs are accelerated at shocks. Another study on the differences of the energy-based method and the entropy-conserving scheme is provided by Semenov et al. (2021). According to their results, the use of the energy-based method leads to spurious entropy generation at shocks due to the numerical inaccuracies described earlier. Moreover, they find that this error depends on the shock Mach number and the adiabatic indices of the two fluids, while the entropy-conserving scheme does not suffer from any of these inaccuracies. This led them to conclude that the entropy-conserving scheme is the preferred choice to model CR fluids.

In this work, we investigate the differences of the CR energy and CR entropy formulations for CR transport performing simulations that are carried out with the moving-mesh code Arepo. We use *Heaviside-Lorentz units* throughout this work.

2 Theoretical background

In this section, we present the theoretical background of this work. We justify and derive the equations of ideal MHD in Sec. 2.1, we review the main properties of astrophysical shocks in Sec. 2.2, we introduce the key points of CR physics in Sec. 2.3, and we present the set of CR-MHD equations we use in this work in Sec. 2.4.

2.1 Ideal MHD

2.1.1 Fluid approximation

To derive the equations of ideal MHD, we consider the thermal plasma of astrophysical systems in the so-called fluid approximation, which allows studying multi-particle systems collectively covered by a small set of physical quantities. In the following, we discuss the crucial aspects of this approximation based on Pfrommer (2022a).

We describe the thermal plasma as a perfectly conducting fluid with an equation of state (EOS) $P_{\rm th} = (\gamma_{\rm th} - 1)\varepsilon_{\rm th}$ that links the thermal pressure $P_{\rm th}$ to the thermal energy density $\varepsilon_{\rm th}$ via the adiabatic exponent $\gamma_{\rm th} = 5/3$ of an ideal, non-relativistic gas. This fluid approximation is only valid when the mean free path $\lambda_{\rm mfp}$ of the gas particles is much smaller than the typical size L of the astrophysical system, resulting in frequent binary interactions of the particles and rendering their momentum distribution to approach a smooth Maxwell-Boltzmann distribution. For electrons, which primarily mediate the temperature in the plasma, the classical electron radius $r_{\rm e}$ can be determined to an order of magnitude by equating its thermal energy and electrostatic potential:

$$r_{\rm e} \approx \frac{e^2}{k_{\rm B} T_{\rm e}}, \tag{1}$$

where e is the elementary charge, $T_{\rm e}$ is the electron temperature, and $k_{\rm B}$ denotes Boltzmann's constant. The mean free path of a thermal electron can then be expressed as:

$$\lambda_{\rm mfp} = \frac{1}{n_{\rm e}\,\sigma \ln \Lambda_{\rm C}} = \frac{1}{n_{\rm e} \pi r_{\rm e}^2 \ln \Lambda_{\rm C}}, \tag{2}$$

where $n_{\rm e}$ is the electron number density, and σ is the electron cross-section supplemented by a correction factor $\ln \Lambda_{\rm C}$, the *Coulomb logarithm*, that accounts for distant electrostatic interactions. Translating Eq. (2) to typical astrophysical scales, the collisional electron mean free path reads as:

$$\lambda_{\rm mfp} = 10^{-5}\,{\rm pc} \left(\frac{T_{\rm e}}{10^4\,{\rm K}}\right)^2 \left(\frac{n_{\rm e}}{{\rm cm}^{-3}}\right)^{-1}. \tag{3}$$

Since $L \sim$ kpc for galaxies, we have $\lambda_{\rm mfp} \ll L$ and can thus treat the cold and warm phase of the interstellar medium (ISM) as a fluid. However, the hot, volume-filling phase ($T_{\rm e} \geq 10^6\,{\rm K}, n_{\rm e} \leq 10^{-2}\,{\rm cm}^{-3}$) has $\lambda_{\rm mfp} \geq 10\,{\rm pc}$, so that kinetic plasma effects have to be considered, which may substantially lower the effective mean free path. This is the case, for example, in the outskirts of galaxies or galaxy clusters.

2.1.2 Equations of ideal MHD

We can now derive the equations of ideal MHD, which represent conservation laws for mass, momentum and energy, neglecting viscosity and convective heat flux (Pringle and King, 2007; Raychaudhuri, 2022).

Continuity equation The fluid mass contained in a constant volume V can change in time only if there is a mass flux through the volume surface A:

$$\frac{\partial}{\partial t}\int_V \rho \,\mathrm{d}V = -\int_A \rho \boldsymbol{u}\cdot\boldsymbol{n}\,\mathrm{d}A\,, \tag{4}$$

where ρ is the gas mass density, $\boldsymbol{u}$ is the mean bulk velocity of the gas, and $\boldsymbol{n}$ denotes the normal vector to the volume surface A. Since V is constant, we can take the time derivative on the left-hand side (LHS) into the integral, and we apply Gauss' divergence theorem to the integrand on the right-hand side (RHS):

$$\int_V \left(\frac{\partial \rho}{\partial t} + \boldsymbol{\nabla}\cdot\rho\boldsymbol{u}\right)\mathrm{d}V = 0\,. \tag{5}$$

This must hold for any volume, and thus the integrand itself must vanish:

$$\boxed{\frac{\partial \rho}{\partial t} + \boldsymbol{\nabla}\cdot\rho\boldsymbol{u} = 0}\,. \tag{6}$$

This is the *continuity equation* of ideal MHD. If we perform the integration in Eq. (5) assuming $V \to \infty$ and again apply Gauss' divergence theorem, we find that the total gas mass M is conserved since any flux vanishes at infinity:

$$\int_V \left(\frac{\partial \rho}{\partial t} + \boldsymbol{\nabla}\cdot\rho\boldsymbol{u}\right)\mathrm{d}V = \frac{\partial M}{\partial t} + \lim_{A\to\infty}\int_A \rho\boldsymbol{u}\cdot\boldsymbol{n}\,\mathrm{d}A = \frac{\mathrm{d}M}{\mathrm{d}t} = 0. \tag{7}$$

Momentum conservation We apply the same considerations to the momentum of the gas, taking into account that force densities $\boldsymbol{f}$ cause additional acceleration, and obtain:

$$\frac{\partial(\rho\boldsymbol{u})}{\partial t} + \boldsymbol{\nabla}\cdot\rho\boldsymbol{u}\boldsymbol{u} = \boldsymbol{f}. \tag{8}$$

Regarding a thermal plasma, the relevant force densities are:

$$\boldsymbol{f} = \boldsymbol{f}_\mathrm{P} + \boldsymbol{f}_\mathrm{G} + \boldsymbol{f}_\mathrm{L} = -\boldsymbol{\nabla}P_\mathrm{th} + \rho\boldsymbol{\nabla}\Phi + \frac{\boldsymbol{j}}{c}\times\boldsymbol{B}, \tag{9}$$

where $\boldsymbol{f}_\mathrm{P}$ is the pressure gradient force density, $\boldsymbol{f}_\mathrm{G}$ is the gravitational force density, $\boldsymbol{f}_\mathrm{L}$ is the Lorentz force density, P_th denotes the thermal gas pressure, Φ is the gravitational potential described by Poisson's equation $\boldsymbol{\nabla}^2\Phi = 4\pi G\rho$ with Newton's constant G, $\boldsymbol{j}$ is the current density, $\boldsymbol{B}$ is the mean magnetic field, and c denotes the speed of light. We employ Ampere's law at low frequencies, $\boldsymbol{\nabla}\times\boldsymbol{B} = \boldsymbol{j}/c$, to reformulate the Lorentz force:

$$\boldsymbol{f}_\mathrm{L} = (\boldsymbol{B}\cdot\boldsymbol{\nabla})\boldsymbol{B} - \frac{1}{2}\boldsymbol{\nabla}\boldsymbol{B}^2, \tag{10}$$

where the terms on the RHS denote force densities due to magnetic tension and magnetic pressure, respectively. Substituting into Eq. (8), employing the identity $\boldsymbol{\nabla \cdot BB} = (\boldsymbol{B \cdot \nabla})\boldsymbol{B}$, and rearranging terms, we find:

$$\boxed{\frac{\partial(\rho \boldsymbol{u})}{\partial t} + \boldsymbol{\nabla \cdot}(\rho \boldsymbol{uu} + P\mathbf{1} - \boldsymbol{BB}) = \rho \boldsymbol{\nabla} \Phi}\,, \tag{11}$$

where $P = P_{\mathrm{th}} + \boldsymbol{B}^2/2$ is the total MHD pressure composed of thermal and magnetic pressure. This is the *momentum equation* of ideal MHD, which states momentum conservation in the absence of gravity. Combining Eq. (11) with the identity:

$$\frac{\partial}{\partial t}(\rho \boldsymbol{u}) + \boldsymbol{\nabla \cdot}(\rho \boldsymbol{uu}) = \rho \left[\frac{\partial \boldsymbol{u}}{\partial t} + (\boldsymbol{u \cdot \nabla})\boldsymbol{u}\right], \tag{12}$$

the momentum equation can be expressed in simplified form:

$$\frac{\partial \boldsymbol{u}}{\partial t} + (\boldsymbol{u \cdot \nabla})\boldsymbol{u} = -\frac{\boldsymbol{\nabla} P}{\rho} + \frac{\boldsymbol{\nabla \cdot BB}}{\rho} + \rho \boldsymbol{\nabla} \Phi\,. \tag{13}$$

Energy conservation We describe the energy density $\varepsilon = \varepsilon_{\mathrm{th}} + \frac{1}{2}\rho \boldsymbol{u}^2$ contained in an arbitrary volume as the sum of thermal and kinetic energy densities. This quantity can change either by energy flux through the volume surface, by pressure work done on the surface, or by external gravitational forces $\rho \boldsymbol{\nabla} \Phi$:

$$\frac{\partial}{\partial t}(\varepsilon_{\mathrm{th}} + \frac{1}{2}\rho \boldsymbol{u}^2) + \boldsymbol{\nabla \cdot}(\varepsilon_{\mathrm{th}} + \frac{1}{2}\rho \boldsymbol{u}^2 + P_{\mathrm{th}})\boldsymbol{u} = \rho \boldsymbol{u \cdot \nabla} \Phi\,. \tag{14}$$

This does not yet include the magnetic energy. We combine Faraday's induction equation $\partial \boldsymbol{B}/\partial t = -c\,\boldsymbol{\nabla} \times \boldsymbol{E}$ and the ideal Ohm law $\boldsymbol{E} = -\boldsymbol{u} \times \boldsymbol{B}/c$ in the limit of infinite conductivity, yielding:

$$\boxed{\frac{\partial \boldsymbol{B}}{\partial t} = \boldsymbol{\nabla} \times (\boldsymbol{u} \times \boldsymbol{B}) = -\boldsymbol{\nabla \cdot}(\boldsymbol{Bu} - \boldsymbol{uB})}\,, \tag{15}$$

where we have used the constraint of vanishing divergence of the magnetic field, $\boldsymbol{\nabla \cdot B} = 0$, in the last step. We multiply Eq. (15) by $\boldsymbol{B}$ and find:

$$\frac{\partial}{\partial t}(\frac{1}{2}\boldsymbol{B}^2) + \boldsymbol{\nabla \cdot}\left[\boldsymbol{B}^2 \boldsymbol{u} - \boldsymbol{B}(\boldsymbol{u \cdot B})\right] = 0. \tag{16}$$

Noticing that $\varepsilon_B = \boldsymbol{B}^2/2$, we arrive at

$$\frac{\partial \varepsilon_{\mathrm{B}}}{\partial t} + \boldsymbol{\nabla \cdot}\left[(\varepsilon_{\mathrm{B}} + \frac{1}{2}\boldsymbol{B}^2)\boldsymbol{u} - \boldsymbol{B}(\boldsymbol{u \cdot B})\right] = 0. \tag{17}$$

This is the evolution equation of magnetic energy density of ideal MHD. Adding Eqs. (14) and (17) yields:

$$\boxed{\frac{\partial \varepsilon}{\partial t} + \boldsymbol{\nabla \cdot}\left[(\varepsilon + P)\boldsymbol{u} - \boldsymbol{B}(\boldsymbol{u \cdot B})\right] = -\rho \boldsymbol{u \cdot \nabla} \Phi}\,, \tag{18}$$

where $\varepsilon = \varepsilon_{\mathrm{th}} + \rho \boldsymbol{u}^2/2 + \varepsilon_{\mathrm{B}}$ is the total MHD energy density. This is the *energy conservation equation* of ideal MHD. The kinetic term of the MHD energy density obeys a conservation law that reads as:

$$\frac{\partial}{\partial t}\left(\frac{1}{2}\rho \boldsymbol{u}^2\right) = -\boldsymbol{\nabla}\cdot\left(\frac{1}{2}\rho \boldsymbol{u}^2 \boldsymbol{u}\right) - \boldsymbol{u}\cdot\boldsymbol{\nabla}P - \rho \boldsymbol{u}\cdot\boldsymbol{\nabla}\Phi. \tag{19}$$

Substituting into Eq. (14) and inserting the EOS of the thermal gas gives:

$$\frac{\partial P_{\mathrm{th}}}{\partial t} = -\gamma_{\mathrm{th}} P_{\mathrm{th}} \boldsymbol{\nabla}\cdot\boldsymbol{u} - \boldsymbol{u}\cdot\boldsymbol{\nabla}P_{\mathrm{th}}, \tag{20}$$

which describes the evolution of the internal energy density of the thermal gas.

Entropy conservation Considering the first law of thermodynamics:

$$\frac{\mathrm{d}\varepsilon}{\rho} = \frac{P}{\rho^2}\mathrm{d}\rho + T\mathrm{d}s, \tag{21}$$

where T is the temperature of the system, and s denotes the specific entropy. Combining it with Eqs. (6) and (18) and neglecting magnetic fields, we arrive at:

$$\boxed{\frac{\partial(\rho s)}{\partial t} + \boldsymbol{\nabla}\cdot(\rho s \boldsymbol{u}) = 0}, \tag{22}$$

which states *conservation of entropy density* in the absence of viscosity and heat conduction. The general EOS for an ideal gas reads in its differential form:

$$\frac{\mathrm{d}\varepsilon}{\rho} = \frac{1}{\gamma - 1}\left(\frac{\mathrm{d}P}{\rho} - \frac{P}{\rho^2}\mathrm{d}\rho\right), \tag{23}$$

where γ is the adiabatic index of the gas. Substituting into Eq. (21) and assuming only adiabatic changes ($\mathrm{d}s = 0$), we obtain:

$$P = P_0\left(\frac{\rho}{\rho_0}\right)^{\gamma} \equiv K\rho^{\gamma}. \tag{24}$$

Consequently, for a polytropic gas, K defines a quantity that remains constant under adiabatic changes and is therefore called entropy.

2.1.3 Eigenstructure of ideal MHD

We investigate the *eigenstructure* of ideal MHD and are thus interested in the eigenvalues of the corresponding set of equations. Neglecting gravity ($\boldsymbol{\nabla}\Phi = 0$), the conservation laws for mass, momentum, energy, and magnetic fields of ideal MHD can be expressed in a more compact form:

$$\frac{\partial}{\partial t}\boldsymbol{U} + \boldsymbol{\nabla}\cdot\boldsymbol{F}(\boldsymbol{U}) = \boldsymbol{0}. \tag{25}$$

Here, $\boldsymbol{U}$ contains the conserved quantities and $\boldsymbol{F}$ represents the fluxes of the system:

$$\boldsymbol{U} = \begin{pmatrix} \rho \\ \rho\boldsymbol{u} \\ \varepsilon \\ \boldsymbol{B} \end{pmatrix}, \quad \boldsymbol{F} = \begin{pmatrix} \rho\boldsymbol{u} \\ \rho\boldsymbol{u}\boldsymbol{u} + P\mathbf{1} + \boldsymbol{B}\boldsymbol{B} \\ (\varepsilon + P)\boldsymbol{u} + \boldsymbol{B}(\boldsymbol{u}\cdot\boldsymbol{B}) \\ \boldsymbol{B}\boldsymbol{u} + \boldsymbol{u}\boldsymbol{B} \end{pmatrix}. \tag{26}$$

To reduce the complexity of the following considerations, we focus on a plane-parallel scenario, i.e. $\partial/\partial y = \partial/\partial z = 0, \partial/\partial x = \mathrm{d}/\mathrm{d}x$. We carry out the spatial derivative in Eq. (25) to find its quasi-linear formulation:

$$\frac{\partial}{\partial t}\boldsymbol{U} + \boldsymbol{A}(\boldsymbol{U})\frac{\mathrm{d}\boldsymbol{U}}{\mathrm{d}x} = \mathbf{0}, \tag{27}$$

where $\boldsymbol{A} = \partial\boldsymbol{F}/\partial\boldsymbol{U}$ is the Jacobian of the flux function. It is convenient to transform the system to its primitive variables $\boldsymbol{W} = (\rho, \boldsymbol{u}, P, \boldsymbol{B})$ (Roe and Balsara, 1996):

$$\frac{\partial\boldsymbol{U}}{\partial\boldsymbol{W}}\frac{\partial\boldsymbol{W}}{\partial t} + \boldsymbol{A}\frac{\partial\boldsymbol{U}}{\partial\boldsymbol{W}}\frac{\mathrm{d}\boldsymbol{W}}{\mathrm{d}x} = \mathbf{0}, \tag{28}$$

or equivalently:

$$\frac{\partial\boldsymbol{W}}{\partial t} + \bar{\boldsymbol{A}}\frac{\mathrm{d}\boldsymbol{W}}{\mathrm{d}x} = \mathbf{0}, \tag{29}$$

where

$$\bar{\boldsymbol{A}} = \frac{\partial\boldsymbol{W}}{\partial\boldsymbol{U}}\boldsymbol{A}\frac{\partial\boldsymbol{U}}{\partial\boldsymbol{W}}. \tag{30}$$

The matrix $\bar{\boldsymbol{A}}$ contains all the information concerning the spatial transport of the primitive fluxes. Each eigenvalue provides information about any designated velocity in the transport of the components of $\boldsymbol{W}$. Since the set of MHD equations is hyperbolic, the matrix $\bar{\boldsymbol{A}}$ is diagonalizable and its seven eigenvalues are:

$$\lambda_{1,7} = u \mp c_{\mathrm{fa}}, \tag{31}$$
$$\lambda_{3,5} = u \mp c_{\mathrm{sl}}, \tag{32}$$
$$\lambda_{2,6} = u \mp v_{\mathrm{A}}, \tag{33}$$
$$\lambda_{4} = u. \tag{34}$$

These eigenvalues describe the propagation of plasma waves. λ_4 corresponds to an entropy wave that propagates with the mean gas velocity u. $\lambda_{2,6}$ describe two shear-Alfvén waves that propagate along the magnetic field at the Alfvén velocity $v_{\mathrm{A}} = B/\sqrt{\rho}$, where $B = |\boldsymbol{B}|$. $\lambda_{3,5}$ and $\lambda_{1,7}$ correspond to two slow and two fast magneto-acoustic waves, respectively, and their velocities are given by (Sturrock, 1994):

$$c_{\mathrm{fa,\,sl}} = \left[\frac{\gamma P_{\mathrm{th}} + B^2 \pm \sqrt{\left(\gamma P_{\mathrm{th}} + B^2\right)^2 - 4\gamma_{\mathrm{th}} P_{\mathrm{th}} B_x^2}}{2\rho}\right]^{1/2}. \tag{35}$$

It can be shown that $c_{\mathrm{sl}} \leq v_A \leq c_{\mathrm{fa}}$, explaining the names of the slow and the fast waves. For vanishing magnetic fields, the system reduces to a purely hydrodynamic system. We then have $c_{\mathrm{fa}} = c_{\mathrm{s}}$ and $c_{\mathrm{sl}} = v_{\mathrm{A}} = 0$, implying that the fast magneto-sonic wave degenerates to an ordinary acoustic wave, and Alfvén and slow magneto-sonic waves disappear.

2.2 Shocks

Astrophysical shocks are a principal driver of CR acceleration. In this section, we summarize the most important properties of shocks. Our discussion is based on Pfrommer (2022a).

In general, a shock occurs when a perturbation (e.g. of the pressure) in a medium propagates faster than the local sound speed c_s, which defines the maximum speed for the transport of information in the medium. Consequently, the unperturbed part of the medium does not notice when the shock approaches, which causes a sudden compression and thus a quasi discontinuous transition between the unperturbed and the compressed regions. The width of this transition layer is defined by the mean free path $\lambda_{\rm mfp}$ of the particles involved. In a *collisional* shock, $\lambda_{\rm mfp}$ is determined by the time between binary collisions mediated by Coulomb-interactions. A shock is called *collisionless* when the mean free path is reduced by many orders of magnitude compared to the collisional case, making the transition layer quasi discontinuous. This is when particles are affected by scattering from electromagnetic waves rather than binary collisions because particle-wave interactions are mediated on much shorter timescales.

Rankine-Hugoniot jump conditions The conservation laws derived in Sec. 2.1 are still valid at shocks. However, in the context of shocks, they can be expressed more compactly. We neglect gravity ($\boldsymbol{\nabla}\Phi = 0$ in Eq. (11)), which is plausible because it acts on much longer timescales than the transition times for shocks. We assume steady-state ($\partial/\partial t = 0$) and a plane-parallel geometry. Applying the given assumptions to the conservation laws for mass (Eq. (6)), momentum (Eq. (11)), and energy (Eq. (18)), supplemented by the evolution equation of kinetic energy (Eq. (19)) and assuming the magnetic field $\boldsymbol{B} = (B, 0, 0)$ is oriented parallel to the normal of the infinitesimal thin shock surface, we find (Landau, 1987):

$$\rho_1 u_1 = \rho_2 u_2, \tag{36}$$

$$\rho_1 u_1^2 + P_1 = \rho_2 u_2^2 + P_2, \tag{37}$$

$$\frac{1}{2}u_1^2 + \epsilon_1 + \frac{P_1}{\rho_1} = \frac{1}{2}u_2^2 + \epsilon_2 + \frac{P_2}{\rho_2}, \tag{38}$$

$$B_1 = B_2, \tag{39}$$

where ϵ denotes the specific energy of the gas. These are the *Rankine-Hugoniot jump conditions* that describe the transition between the pre-shock (index 1) and post-shock (index 2) quantities in the shock rest frame.

Contact discontinuity Equation (36) allows for two different types of solutions. The first one is clearly $u_1 = u_2 = 0$ and is called tangential discontinuity. It is characterized by a constant pressure across its interface, which follows from Eq. (37). There is no mass flow through the interface because the normal component of the velocity is constant. If additionally the tangential velocity component is constant, the discontinuity is called *contact discontinuity* (CD). In general, such discontinuities can result in an arbitrary jump in density that must be balanced by the same jump

in temperature in the opposite direction to keep the pressure constant. The second type of solution to Eq. (36) requires $\rho_1 u_1 \neq 0$. Hence, there is mass flow through the interface, and we call this solution a shock.

Shock Mach number An important quantity to characterize a shock is the upstream *shock Mach number*, which is defined by the ratio of shock speed u_1 to upstream (i.e. the pre-shock region, indicated by the index '1') sound speed c_1:

$$\mathcal{M}_1 = \frac{u_1}{c_1} = \sqrt{\frac{m u_1^2}{\gamma k_B T_1}}\,. \tag{40}$$

This definition implies that the shock Mach number can also be interpreted as the ratio of kinetic to thermal energy. The Rankine-Hugoniot jump conditions can be reformulated in terms of $\mathcal{M}_1$ (Landau, 1987):

$$\frac{\rho_2}{\rho_1} = \frac{u_1}{u_2} = \frac{(\gamma+1)\mathcal{M}_1^2}{(\gamma-1)\mathcal{M}_1^2+2} \xrightarrow{\mathcal{M}_1 \gg 1} \frac{\gamma+1}{\gamma-1}, \tag{41}$$

$$\frac{P_2}{P_1} = \frac{2\gamma\mathcal{M}_1^2-(\gamma-1)}{\gamma+1} \xrightarrow{\mathcal{M}_1 \gg 1} \frac{2\gamma\mathcal{M}_1^2}{\gamma+1}, \tag{42}$$

$$\frac{T_2}{T_1} = \left(\frac{c_2}{c_1}\right)^2 = \frac{[(\gamma-1)\mathcal{M}_1^2+2][2\gamma\mathcal{M}_1^2-(\gamma-1)]}{(\gamma+1)^2\mathcal{M}_1^2} \xrightarrow{\mathcal{M}_1 \gg 1} \frac{2\gamma(\gamma-1)\mathcal{M}_1^2}{(\gamma+1)^2}, \tag{43}$$

where γ is the polytropic index of the gas, variables with index '2' denote the post-shock quantities, and the last term in each equation denotes the limit for strong shocks with $\mathcal{M}_1 \gg 1$. We define the downstream (i.e. the post-shock region) Mach number in the same way and substitute the strong shock limit of Eqs. (41) and (43), yielding:

$$\mathcal{M}_2 = \frac{u_2}{c_2} = \frac{u_1}{c_1}\frac{u_2}{u_1}\frac{c_1}{c_2} = \sqrt{\frac{\gamma-1}{2\gamma}}. \tag{44}$$

This shows that, for $\gamma > 1$, a shock transforms a supersonic gas into a denser, slower moving, higher pressure, subsonic gas. The shock converts kinetic energy into thermal and non-thermal energy, the former increasing the entropy of the gas, while the latter can, for example, accelerate CRs.

2.3 Cosmic rays

We use this section to introduce the fundamental aspects of CR physics. To start with, we review some principal characteristics of CRs, drawing on the work of Zweibel (2013, 2017).

CRs represent the high-energy, non-thermal particle population of an astrophysical plasma and are ubiquitous in the Milky Way and presumably in any other galaxy. They amount to only 10^{-9} of the interstellar particles by number, but their total energy density and pressure (see Sec. 2.3.1) is about the same as that of thermal particles. CRs are collisionless and interact with the thermal plasma mostly through particle-wave interactions by scattering off of self-generated magnetic perturbations,

so-called Alfvén waves (see Sec. 2.3.2). They acquire their high energies through several acceleration processes, some of which we will discuss in Sec. 2.3.3.

CR ions (protons and heavier nuclei) account for about 99 per cent of the total CR number N and obey piece-wise power-law distributions $N(E) \propto E^{-\alpha}$ covering many orders of magnitude in flux and energy, from the non-relativistic to the highly relativistic regime. Figure 1 shows a synthesized CR spectrum obtained by many experiments and contains several interesting features. The most prominent one is the turnover at around 10 GeV. These lower-energy CRs are strongly confined to the magnetic field of the solar wind which advects the CRs outwards, rendering their flux highly uncertain. Up to energies of $\approx 3 \times 10^6$ GeV, most CRs are protons with a spectral index of $\alpha = 2.6$. This energy range accounts for the largest fraction of the total CR energy. At $E \approx 3 \times 10^6$ GeV, the spectrum steepens. This feature is called the *knee* and is considered to be the result of a change in the acceleration or confinement processes of CRs. Around 10^9 GeV, the spectrum flattens again, and we call this feature the *ankle*. The gyro radii of these high-energy CRs are larger than the size of the galaxy, making them unbound and thus presumably extra-galactic in origin.

CR electrons are dynamically unimportant in most astrophysical systems because

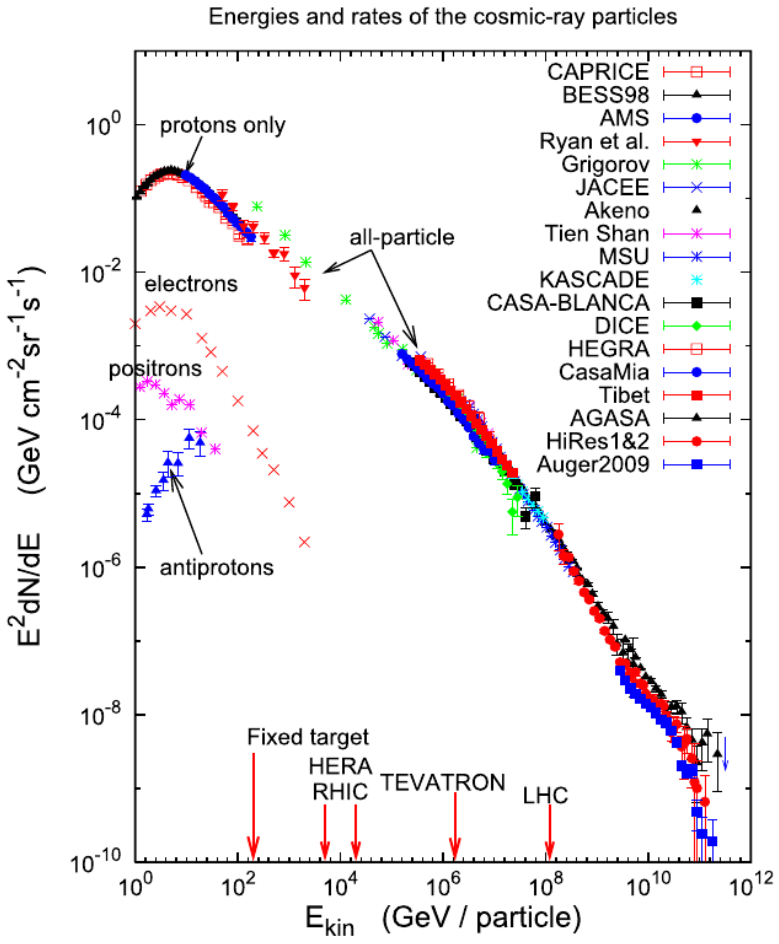

Figure 1: CR energy flux measured in numerous experiments (legend on the RHS), separated into particle species (Zweibel, 2013)

of their negligible number ($\approx$ 1 per cent) and mass compared to their hadronic counterpart. However, because their cooling time ($\sim$ Myr) is significantly shorter than that of the ions ($\sim$ Gyr), CR electrons are crucial for the direct measurement of CRs in galaxies and galaxy clusters (see Sec. 2.3.4). In this work, we focus on the dynamic effects of CRs and thus neglect the minor influence of CR electrons in the following.

Although CRs do not behave like a fluid in the conventional sense, they can still be described as a fluid similar to thermal gas in many situations. We discuss the necessary conditions in Sec. 2.3.5 and conclude by deriving the CR-MHD equations (see Sec. 2.3.6).

2.3.1 Basic CR variables

Here we introduce a selection of important quantities concerning CR physics which we will refer to in the rest of the paper. The following definitions are based on Pfrommer et al. (2006).

We assume that the differential momentum spectrum per volume element of CR protons can be approximated by a single power law in momentum:

$$f(\boldsymbol{r}, \boldsymbol{p}) = \frac{\mathrm{d}^6 N}{\mathrm{d}p^3\, \mathrm{d}r^3} = C p^{-\alpha} \Theta(p - q), \tag{45}$$

where $p = P_\mathrm{p}/m_\mathrm{p}c$ is the dimensionless CR momentum with P_p the proton momentum and m_p the proton rest mass, $C \equiv C(\boldsymbol{r}, t)$ is a space and time dependent normalization, $\Theta(x)$ denotes the Heaviside step function, and $q \equiv q(\boldsymbol{r}, t)$ is the minimum momentum cut-off indicating the non-relativistic limit for $q \to 0$ and the ultra-relativistic limit for $q \to \infty$. We can then define the CR kinetic energy density and pressure, respectively:

$$\varepsilon_\mathrm{cr} = \int_0^\infty \mathrm{d}p\, f(p)\, E_\mathrm{p}(p) = \frac{C\, m_\mathrm{p}\, c^2}{\alpha - 1} \left[\frac{1}{2} \mathcal{B}_x\,(a, b) + q^{\alpha-1} (\sqrt{1 + q^2} - 1) \right], \tag{46}$$

$$P_\mathrm{cr} = \frac{m_\mathrm{p} c^2}{3} \int_0^\infty \mathrm{d}p\, f(p)\, \beta\, p = \frac{C m_\mathrm{p} c^2}{6} \mathcal{B}_x\,(a, b)\,, \tag{47}$$

where $\beta = v/c$ is the dimensionless velocity of the CRs, $\mathcal{B}_x(a, b)$ denotes the incomplete beta function with $x = 1/(1 + q^2)$, $a = (\alpha - 2)/2$, $b = (3 - \alpha)/2$, and $E_\mathrm{p}(p) = (\sqrt{1 + p^2} - 1) m_\mathrm{p} c^2$ is the kinetic energy of a proton.

Liouville's theorem guarantees the constancy of phase-space density for adiabatic compression and expansion. Thus, a change in gas density from ρ_0 to ρ leads to a momentum shift of $p' \to p = p_0 (\rho/\rho_0)^{1/3}$. We can replace the momentum cut-off q and normalization C by adiabatically invariant variables:

$$q(\rho) = q_0 (\rho/\rho_0)^{1/3}, \tag{48}$$

$$C(\rho) = C_0 (\rho/\rho_0)^{(\alpha+2)/3}. \tag{49}$$

The adiabatic index of a CR population is given by:

$$\gamma_\mathrm{cr} = \left. \frac{\mathrm{d} \log P_\mathrm{cr}}{\mathrm{d} \log \rho} \right|_S, \tag{50}$$

where ρ is the density of the ambient medium and the derivative has to be taken at constant entropy S. Substituting Eqs. (47), (48), and (49), the CR adiabatic index can be expressed as:

$$\gamma_{\rm cr} = \frac{\alpha+2}{3} - \frac{2}{3} q^{2-\alpha} \beta \, \mathcal{B}_x \left(a, b\right)^{-1}, \tag{51}$$

and we obtain its non-relativistic and ultra-relativistic limits by:

$$\gamma_{\rm cr} \xrightarrow{q\to 0} \frac{5}{3} \;\; ; \;\; \alpha > 3, \tag{52}$$

$$\gamma_{\rm cr} \xrightarrow{q\to \infty} \frac{4}{3} \;\; ; \;\; \alpha > 2. \tag{53}$$

Since we focus on ultra-relativistic CRs with $v \approx c$ in this work, we will exclusively use $\gamma_{\rm cr} = 4/3$ from now on.

2.3.2 Interaction with the thermal gas

CRs in astrophysical plasma environments are virtually collisionless in the sense that their Coulomb and hadronic interactions with particles of the thermal gas do not significantly affect the dynamics of the system. However, a particle-wave interaction mechanism exists that allows energy transfer from the CRs to the thermal gas. We briefly discuss this mechanism in the following (see e.g. Kulsrud and Pearce, 1969, for further details).

In general, CRs orbit around the unperturbed magnetic field lines in the ISM due to the acceleration caused by the Lorenz force (see Fig. 2, left). Their gyro-radius is given by:

$$r_{\rm g} = \frac{p_\perp c}{ZeB}, \tag{54}$$

where $p_\perp$ denotes the magnitude of the CR momentum perpendicular to the mean magnetic field $\boldsymbol{B}$ with $B = |\boldsymbol{B}|$, Ze is the particle's charge with Z the atomic number, and $r_{\rm g} \sim 1\,\mathrm{AU}$ in galaxies. In this scenario, a charged fluid (i.e. the CRs, as we justify in Sec. 2.3.6) moves relative to a magnetic field, inducing an electric current and thus an electromagnetic force that acts back on the motion of the CRs. The kind of resonant MHD waves generated as a result of this interaction are called *Alfvén waves* (Alfvén, 1942). Alfvén waves propagate along the magnetic field lines with the local Alfvén velocity $\boldsymbol{v}_{\rm A} = \boldsymbol{B}/\sqrt{\rho}$ relative to the thermal gas and oscillate with frequency ω. CRs and Alfvén waves resonate when the Doppler-shifted wave frequency perceived by the CRs is a multiple of the CR gyro-frequency Ω:

$$\omega - k_{||} v_{||} = n\Omega. \tag{55}$$

Here, $k_{||}$ is the wave number of the Alfvén wave parallel to the magnetic field, and $v_{||} = v\mu$ is the parallel velocity component of the CRs with $\mu = \boldsymbol{v}\cdot\boldsymbol{B}/(vB)$ the cosine of the CR pitch angle, i.e. the angle between CR momentum and magnetic field. n is an integer that defines the type of resonant interaction. This is referred to as Landau resonance when $n = 0$, and gyro-resonance in the case of $n \neq 0$.

When a gyro-resonant CR particle propagates with $v_{||} > v_A$, it experiences a decelerating Lorenz force at each instant (cf. Fig. 2, middle). Since Alfvén waves

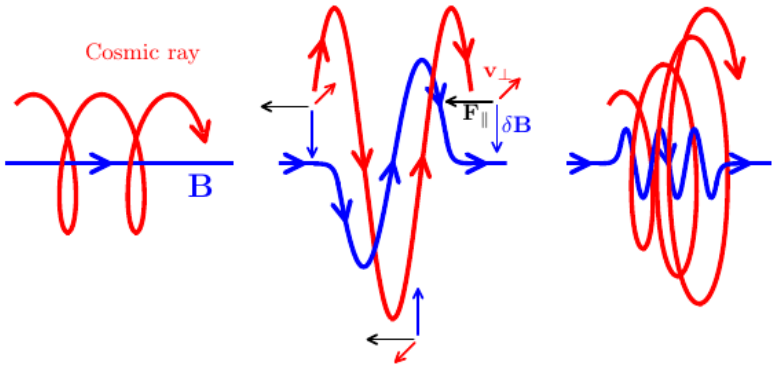

Figure 2: Particle-wave interaction between CRs (red) and Alfvén waves (blue) triggering the gyro-resonant instability (Jacob and Pfrommer, 2017a).

are purely magnetic phenomena, there is no electric field in their own reference frame, and thus the kinetic energy of the CRs is preserved. Hence, only the CR pitch angle is altered (cf. Fig. 2, right), which eventually results in a (partially) isotropic distribution of the CR momentum. In the co-moving reference frame of the CR particle, however, both electric and magnetic fields exist, causing energy transfer from the CR to the self-generated Alfvén wave. This mechanism is called the *gyro-resonant instability* (Kulsrud and Pearce, 1969).

Wave damping processes transfer energy from Alfvén waves to the thermal gas, thus providing an indirect link between CRs and thermal gas. The most important damping processes are ion neutral damping, non-linear Landau damping, turbulent linear Landau damping and turbulent wave damping. For detailed information on the individual processes, we refer the reader to the relevant literature, e.g. Kulsrud and Pearce (1969), Volk and McKenzie (1981), and Farmer and Goldreich (2004). The strength of the wave damping process determines the predominant transport mechanism of CRs. Weak damping of the waves increases the scattering rate of CRs so that they are tightly bound to the Alfvén waves and CR streaming becomes the dominant process. Strong damping, on the other hand, reduces the amplitude of the waves at which CRs can scatter, making the confinement incomplete and causing diffusive motion of the CRs relative to the waves.

2.3.3 CR acceleration

CRs gain their high energy through various astrophysical acceleration processes. In the following, we present the most important mechanisms of CR acceleration.

Adiabatic compression CRs do not move freely through the thermal plasma but are strongly coupled to the magnetic field lines by the Lorenz force and by interactions with Alfvén waves (see Sec. 2.3.2). *Alfvén's theorem* states that, in a fluid that is perfectly conducting, the magnetic field is flux-frozen into the fluid, i.e. it moves along with the thermal gas (Alfvén, 1942). Consequently, CRs are largely tied to the motion of the thermal plasma, leading to an increase in CR pressure and thus CR energy when the plasma is adiabatically compressed.

Fermi-I acceleration This process describes the acceleration of CR particles at collisionless astrophysical shocks induced by SN remnants, active galactic nuclei, galaxy mergers, or inside galaxy clusters (Blandford and Ostriker, 1978). In the following, we discuss the underlying microscopic picture of this acceleration mechanism, exemplified with a plane-parallel shock geometry. We define the reference frame of the shock as the frame in which the shock front is stationary at $x = 0$, and the gas flows parallel to the x-axis with velocity u_1 in the upstream and $u_2 < u_1$ in the downstream. We denote μ the cosine of the CR pitch angle, and $v_{||} = v\mu$ is the parallel component of the CR velocity with $v \approx c$ in the ultra-relativistic limit.

Consider a CR particle that crosses the shock from downstream to upstream. In the rest frame of the upstream gas, the velocity of the shock is greater than the local Alfvén speed (cf. Sec. 2.1.3), and thus the same applies to the velocity of the CR. This causes the excitation of Alfvén waves. Gyro-resonant CRs scatter off of these self-generated waves, which isotropizes the CR momentum distribution and reduces the parallel CR velocity $v_{||}$ to approximately the local Alfvén speed. As a result, the shock will inevitably overtake the CR particle, causing it to cross the shock from upstream back to downstream. Assuming the CR has upstream momentum p in the local fluid frame, its momentum in the reference frame of the shock is given by $p(1 + \mu u_1/c)$. This remains unchanged when traversing the shock because the shock is collisionless. Thus, after passing the shock, the CR momentum relative to the downstream gas is $p(1 + \mu(u_1 - u_2)/c)$ with $\mu > 0$ for a transition from upstream to downstream.

We denote n the downstream number density of CR particles. The flux of CRs escaping the shock downstream is given by $f_{\text{out}} = nu_2$, and the flux entering the downstream region from upstream the shock is calculated as (Drury, 1983):

$$f_{\text{in}} = \int_0^1 \mathrm{d}\mu \, nc\mu/2 = nc/4, \tag{56}$$

where we assumed a constant n, which follows from the diffusion equation, and an isotropic CR distribution behind the shock with half of the CR particles propagating to the left and right, respectively. The probability of never returning to the shock is then given by the ratio of both fluxes:

$$P_{\text{esc}} = f_{\text{out}}/f_{\text{in}} \approx 4u_2/c. \tag{57}$$

For non-relativistic shocks, the probability of CR particles escaping the shock downstream is therefore negligible, so that most CR particles re-cross the shock front from downstream back to upstream. This purely statistical argument can be illustrated by the presence of shock-induced magnetic turbulences ubiquitous in the downstream gas. These turbulences mediate innumerable scatterings by which CRs are reflected back to the upstream region (Bell, 1978). After passing the shock from downstream to upstream, the CR momentum relative to the upstream gas is given by $p(1 + \mu(u_2 - u_1)/c)$ with $\mu < 0$.

Consequently, with each shock crossing, a CR particle perceives an approaching magnetic mirror serving as a scattering agent. This interaction ultimately increases the particle's energy each time it passes through the shock front. Integrating over

μ and neglecting the small change in pitch angle when crossing the shock in either direction, we find for a shock transition from upstream to downstream (Drury, 1983):

$$\frac{\delta E}{E} = \frac{\delta p}{p} = \int_0^1 \mu \frac{u_1 - u_2}{c} 2\mu \, \mathrm{d}\mu = \frac{2}{3} \frac{u_1 - u_2}{c}, \tag{58}$$

where the additional factor of 2μ results from assuming isotropy, and in this case the probability of crossing the shock at a certain angle $+\theta \in [0, \pi/2]$ or $-\theta \in [-\pi/2, 0]$ is proportional to μ, respectively. We obtain an identical result for a shock transition from downstream to upstream by exchanging u_1 and u_2 and reversing the sign of μ.

Because the energy gain in this process is linear in velocity, it is referred to as *first-order* Fermi acceleration.

Fermi-II acceleration This is the process Enrico Fermi originally proposed to explain the generation of CRs (Fermi, 1949). Unlike the Fermi-I process, where CRs always see an approaching magnetic mirror, in this scenario the scattering off of randomly moving turbulent magnetic mirrors drives the acceleration. CRs gain energy if the magnetic mirror is approaching (head-on collisions), and they lose energy when the mirror is receding (head-tail collisions). Fermi argued that head-on collisions are more frequent than head-tail collisions because the relative velocity between CR particles and electromagnetic waves is larger in the former case. These particle-wave interactions can be illustrated as collisions against randomly placed, reflecting obstacles with very large mass, moving in a disordered fashion and at much lower velocities than the CR particles (Fermi, 1949). In this picture, the motion of the CRs can be described statistically by a random walk, resulting in a net energy gain per collision on the order of:

$$\frac{\delta E}{E} \approx \left(\frac{u}{c}\right)^2, \tag{59}$$

where u is the mean velocity of the magnetic mirrors. However, this picture is incomplete since it involves complicated plasma processes that are not well understood. There has not yet been a first-principle theory of second-order Fermi acceleration suggested.

Because the energy gain in this process is quadratic in velocity, it is referred to as *second-order* Fermi acceleration. This acceleration process is slow compared to the Fermi-I mechanism, thus the CR particles need to have a sufficient amount of energy to overcome the cooling losses (cf. Sec. 2.3.4), making the procedure inefficient for heavier nuclei of the CR population.

2.3.4 CR cooling

In this subsection, we recap the major cooling processes of CR ions and electrons and the types of emission spectra emerging from these processes. This extract is based on Pfrommer (2022a).

(a) Hadronic losses

Adiabatic expansion This is the same but opposite effect as described in Sec. 2.3.3. Adiabatic expansion of the thermal gas reduces the CR pressure and thus CR energy.

Coulomb losses CR particles that propagate through the thermal plasma scatter off of thermal electrons and protons, thereby transferring a fraction of their kinetic energy to the plasma. The sum of both effects we refer to as Coulomb losses. The loss rate of this process can be expressed as (Gould, 1972):

$$\left(\frac{\mathrm{d}E_\mathrm{p}(p)}{\mathrm{d}t}\right)_\mathrm{C} = -\frac{4\pi e^4 n_\mathrm{e}}{m_\mathrm{e}\beta c}\left(\frac{2m_\mathrm{e}c^2\beta p}{\hbar\,\omega_{pl}} - \frac{\beta^2}{2}\right), \tag{60}$$

where $\omega_\mathrm{pl} = \sqrt{4\pi e^2 n_\mathrm{e}/m_\mathrm{e}}$ is the plasma frequency, m_e is the electron rest mass, and $\hbar$ denotes Planck's constant. Coulomb losses efficiently remove the low-energy component of a CR population and redistribute it to the thermal plasma.

Catastrophic losses CR nuclei experience inelastic scattering with thermal ions, atoms, and molecules. Provided that the (dimensionless) CR momentum exceeds the required threshold of $p_\mathrm{thr} \approx 0.83$, these interactions mostly result in the production of neutral and charged pions. The neutral pions decay after a short mean lifetime into γ-rays, and the charged pions decay into secondary CR electrons/positrons and neutrinos:

$$\pi^0 \rightarrow 2\gamma,$$
$$\pi^\pm \rightarrow \mu^\pm + \nu_\mu/\bar{\nu}_\mu \rightarrow e^\pm + \nu_e/\bar{\nu}_e + \nu_\mu + \bar{\nu}_\mu.$$

The loss rate of this hadronic process for CR protons is given by (Pfrommer et al., 2017):

$$\left(\frac{\mathrm{d}E_\mathrm{p}(p)}{\mathrm{d}t}\right)_\mathrm{H} = -n_\mathrm{N}\sigma_\mathrm{pp}K_\mathrm{p}m_\mathrm{p}c^3(\gamma-1)(p-p_\mathrm{thr}), \tag{61}$$

where $n_\mathrm{N} = n_\mathrm{e}/(1 - X_\mathrm{He}/2)$ is the target nucleon density in the ISM with a relative primordial helium abundance of $X_\mathrm{He} = 0.24$, σ_pp is the total pion cross-section, γ is the usual Lorenz factor of the CR protons, and $K_\mathrm{p} \approx 0.5$ indicates the inelasticity of the hadronic collisions (Mannheim and Schlickeiser, 1994).

While the γ-ray emission of the π^0-decay is unique and can be used to identify the presence of CRs, this is not the case for the radio-synchrotron emission (see below) of the secondary electrons because their emission spectrum overlaps with that of any other relativistic electron population.

(b) Leptonic losses

CR electrons lose most of their energy by radiation. We briefly discuss the most important processes of radiative cooling only for completeness since we focus on CR ions in this work.

Radio-synchrotron emission Electrons moving in a magnetized plasma gyrate around magnetic field lines, resulting in a permanent loss of energy due to the acceleration caused by the Lorenz force. Depending on the momentum of the CR electrons, this emission process takes place in the radio regime (low-energy relativistic CRs) or in the X-ray regime (high-energy relativistic CRs).

Bremsstrahlung CR electrons moving through the electrostatic potential of a charged nucleus are deflected and thus emit radiation. This loss process is negligible in regions of low number densities $\leq 1\mathrm{cm}^{-3}$ as well as for high-energy CR ions because this effect is diminished by the electron-to-proton mass ratio squared.

Inverse-Compton scattering When low-energy photons, e.g. starlight or photons of the Cosmic Microwave Background, scatter off of high-energy CR electrons, a small fraction of the CR energy is transferred to the photon.

2.3.5 CR transport

Understanding the transport mechanisms of CRs is essential to gain insight into many astrophysical phenomena. Here we discuss the one-moment transport of CRs, which considers only the isotropic part of the CR distribution, and the two-moment transport, where additionally the anisotropic part of the CRs is included.

One-moment CR transport A mathematical determination of the individual CR trajectories is not possible, so we describe the CRs statistically by their collective effects. The evolution of the CR distribution in phase-space is governed by the Vlasov equation:

$$\frac{\partial f}{\partial t} + \boldsymbol{v} \cdot \boldsymbol{\nabla} f + \boldsymbol{F} \cdot \boldsymbol{\nabla}_{\boldsymbol{p}} f = 0, \tag{62}$$

where $f \equiv f(\boldsymbol{x}, \boldsymbol{p}, t)$ is the phase-space distribution function of the CRs. Here, the equation of motion:

$$\boldsymbol{F} = \frac{\mathrm{d}\boldsymbol{p}}{\mathrm{d}t} = Ze\left[(\boldsymbol{E} + \delta\boldsymbol{E}) + \frac{\boldsymbol{v}}{c} \times (\delta\boldsymbol{B} + \boldsymbol{B})\right] \tag{63}$$

denotes the Lorenz force, where Ze is the particle charge, $\boldsymbol{v}$ is the velocity of the CRs, and $\delta\boldsymbol{E} \ll \boldsymbol{E}$ and $\delta\boldsymbol{B} \ll \boldsymbol{B}$ indicate electromagnetic small-scale fluctuations with respect to the large-scale mean magnetic and electric fields $\boldsymbol{B}$ and $\boldsymbol{E}$, respectively. Inserting the equation of motion into the Vlasov equation (62) yields the effective Boltzmann equation:

$$\frac{\partial f}{\partial t} + \boldsymbol{v} \cdot \boldsymbol{\nabla} f + Ze\left(\boldsymbol{E} + \frac{\boldsymbol{v}}{c} \times \boldsymbol{B}\right) \cdot \boldsymbol{\nabla}_{\boldsymbol{p}} f = \left.\frac{\partial f}{\partial \boldsymbol{p}}\right|_C, \tag{64}$$

where $\boldsymbol{p}$ denotes the CR momentum, and we collected the contributions of small-scale fluctuations in the collision term on the RHS:

$$\left.\frac{\partial f}{\partial \boldsymbol{p}}\right|_c = Ze\left(\delta\boldsymbol{E} + \frac{\boldsymbol{v}}{c} \times \delta\boldsymbol{B}\right) \cdot \boldsymbol{\nabla}_{\boldsymbol{p}} f. \tag{65}$$

Solving the full effective Boltzmann equation (64) for general conditions is not possible since the gyro radii of CRs with energies in the GeV range are up to 10 orders of magnitude smaller than the corresponding system size (e.g. a galaxy). Therefore, intractably small time steps would be required to numerically capture the effects of CRs at this scale (Zweibel, 2013). This problem can be largely circumvented if we make some plausible assumptions.

CRs frequently scatter off of self-generated electromagnetic fluctuations, rendering the CR momentum distribution nearly isotropic and transferring energy from the CR particle to the thermal gas. Because these fluctuations and thus the associated energy transfer are small ($\delta\boldsymbol{B} \ll \boldsymbol{B}, \delta\boldsymbol{E} \ll \boldsymbol{E}$), individual CR scattering events do not have a significant effect on the dynamics of the hydrodynamical system. We thus assume that a CR particle propagates many gyro radii before it affects the system. Consequently, the timescale on which the perturbations become important is much larger than the typical gyro timescale of a CR particle. The hydrodynamic timescale, which is the essential scale for describing the system, is even larger in comparison, so we can average effects on timescales well below. Therefore, we average the effective Boltzmann equation over a full CR gyro-orbit. This results in a Fokker-Planck equation for CR transport in the quasi-linear approximation (Skilling, 1975; Schlickeiser, 2002; Pfrommer et al., 2017):

$$\frac{\partial f}{\partial t} + (\boldsymbol{u}+\boldsymbol{v}_{\rm st})\cdot\boldsymbol{\nabla} f = \boldsymbol{\nabla}\cdot[\kappa \boldsymbol{b}\,(\boldsymbol{b}\cdot\boldsymbol{\nabla} f)] + \frac{p}{3}\frac{\partial f}{\partial p}\boldsymbol{\nabla}\cdot(\boldsymbol{u}+\boldsymbol{v}_{\rm st}) + \frac{1}{p^2}\frac{\partial}{\partial p}\left[p^2 K \frac{\partial f}{\partial p}\right] + S, \quad (66)$$

where f denotes the isotropic part of the three-dimensional (3D) CR distribution, $\boldsymbol{b} = \boldsymbol{B}/B$ is the direction of the mean magnetic field, κ is the spatial diffusion coefficient, K is the momentum diffusion rate, and

$$\boldsymbol{v}_{\rm st} = -\boldsymbol{v}_{\rm A}\,\mathrm{sgn}(\boldsymbol{B}\cdot\boldsymbol{\nabla} f) \quad (67)$$

is the CR streaming velocity. Note that two different coordinate system are used in this description: position $\boldsymbol{x}$ and time t are measured in the laboratory (lab) frame, while $\boldsymbol{p}$ is defined in the reference frame of the streaming CRs that propagate with velocity $\boldsymbol{u} + \boldsymbol{v}_{\rm st}$. The second term on the LHS of Eq. (66) describes the advection of the CRs with the Alfvén waves relative to the lab frame. The terms on the RHS account for (from left to right) diffusive transport along the mean magnetic field, Fermi-I acceleration, Fermi-II acceleration, and S represents sources and sinks of CRs.

Two-moment CR transport Sharma et al. (2009) showed that the numerical evolution of the CR distribution subject to the CR streaming effect (Eq. (67)) is plagued by a numerical instability which causes growing numerical errors on the scales of the numerical grid. This is because of the erratic behaviour of the sgn function in Eq. (67) in regions where $\boldsymbol{B}\cdot\boldsymbol{\nabla} f \approx 0$. There, small fluctuations of this quantity cause high-frequency changes in the streaming speed which leads to a fluctuating transport direction of the CRs. Sharma et al. (2009) propose to smooth the transition of the sgn function in Eq. (67) by replacing it with a regularized counterpart such as the tanh function. An alternative and very effective solution to circumvent this limitation is to introduce an additional equation that evolves the CR

momentum density separately (Jiang and Oh, 2018; Thomas and Pfrommer, 2019, 2022; Thomas et al., 2020, 2021). In the following, we discuss the main arguments of this methodology, mostly based on Thomas and Pfrommer (2019).

In contrast to the one-moment method, where only the isotropic part of the CR distribution function is considered (Eq. (66)), here the CR transport equation is decomposed into isotropic and anisotropic components. To proceed, we use the Vlasov equation in the co-moving frame:

$$\frac{\partial f}{\partial t} + (\boldsymbol{u} + \boldsymbol{v}) \cdot \boldsymbol{\nabla} f + \boldsymbol{F} \cdot \boldsymbol{\nabla}_{\boldsymbol{p}} f = 0, \tag{68}$$

where the mean velocity of the thermal gas $\boldsymbol{u}$ and time t are measured in the lab frame, and CR velocity $\boldsymbol{v}$ and momentum $\boldsymbol{p}$ are measured in the co-moving frame. However, switching to the co-moving frame causes pseudo forces and thus a change in the equation of motion:

$$\boldsymbol{F} = -m\frac{\mathrm{d}\boldsymbol{u}}{\mathrm{d}t} - (\boldsymbol{p} \cdot \boldsymbol{\nabla})\boldsymbol{u} + Ze\left[\delta\boldsymbol{E} + \frac{\boldsymbol{v}}{c} \times (\delta\boldsymbol{B} + \boldsymbol{B})\right], \tag{69}$$

where $\mathrm{d}/\mathrm{d}t = \partial/\partial t + \boldsymbol{u} \cdot \boldsymbol{\nabla}$ denotes the Lagrangian time derivative. The first term on the RHS describes an additional pseudo force due to an acceleration of the gas frame because a CR at rest in the lab frame appears accelerated to a co-moving observer. The second term on the RHS arises when spatial inhomogeneities of the reference velocity $\boldsymbol{u}$ are present. Then, a change of a CR particle's position in the lab frame also changes the reference velocity that links the lab and co-moving frames. For relativistic CRs, the former pseudo force is reduced by a factor of order u/c compared to the latter. We thus we neglect its contribution in the following. The gyro-averaged CR transport equation in the reference frame of the gas is then given by (Zank, 2014):

$$\begin{aligned}\frac{\partial f}{\partial t} + (\boldsymbol{u} + \mu v\boldsymbol{b}) \cdot \boldsymbol{\nabla} f + \left[\frac{1-3\mu^2}{2}(\boldsymbol{b} \cdot \boldsymbol{\nabla}\boldsymbol{u} \cdot \boldsymbol{b}) - \frac{1-\mu^2}{2}\boldsymbol{\nabla} \cdot \boldsymbol{u}\right] p\frac{\partial f}{\partial p} \\ + \left[v\boldsymbol{\nabla} \cdot \boldsymbol{b} + \mu\boldsymbol{\nabla} \cdot \boldsymbol{u} - 3\mu(\boldsymbol{b} \cdot \boldsymbol{\nabla}\boldsymbol{u} \cdot \boldsymbol{b})\frac{1-\mu^2}{2}\right]\frac{\partial f}{\partial \mu} = \left.\frac{\partial f}{\partial t}\right|_C,\end{aligned} \tag{70}$$

where μ denotes the cosine of the CR pitch angle. The complexity of this equation can be reduced by borrowing an idea from radiation transport physics. Assuming that the scattering by gyro-resonant Alfvén waves is frequent, the CR distribution f will be nearly isotropic. In a similar case, when the scattering of radiation is frequent, the *Eddington-approximation* can be applied to the radiation field in order to describe its deviations from isotropy. Translating this idea to the CRs, we can expand the CR transport equation in moments of μ, using Legendre polynomials as basis functions (see e.g. Klimas and Sandri, 1971; Zank et al., 2000; Rodrigues et al., 2019). This results in:

$$f = f_0 + 3\mu f_1, \tag{71}$$

where the monopole moment f_0 describes the isotropic part of the CR distribution, the dipole moment f_1 accounts for the anisotropic part, and we assume that any moment higher than the second has no significant contribution. Inserting the

approximation from Eq. (71) into the transport equation (70) and taking the pitch-angle average and the μ-moment gives, respectively (Thomas and Pfrommer, 2019):

$$\frac{\partial f_0}{\partial t} + \boldsymbol{u}\cdot\boldsymbol{\nabla} f_0 + \boldsymbol{\nabla}\cdot(v\boldsymbol{b}f_1) - (\boldsymbol{\nabla}\cdot\boldsymbol{u})\frac{p}{3}\frac{\partial f_0}{\partial p} = \left.\frac{\partial f_0}{\partial t}\right|_C , \tag{72}$$

$$\frac{\partial f_1}{\partial t} + \frac{v}{3}\boldsymbol{b}\cdot\boldsymbol{\nabla} f_0 + \boldsymbol{u}\cdot\boldsymbol{\nabla} f_1 + \left[-\frac{2}{5}(\boldsymbol{b}\cdot\boldsymbol{\nabla}\boldsymbol{u}\cdot\boldsymbol{b}) - \frac{1}{5}\boldsymbol{\nabla}\cdot\boldsymbol{u}\right] p\frac{\partial f_1}{\partial p} + \left[\frac{1}{5}\boldsymbol{\nabla}\cdot\boldsymbol{u} - \frac{3}{5}(\boldsymbol{b}\cdot\boldsymbol{\nabla}\boldsymbol{u}\cdot\boldsymbol{b})\right] f_1 = \left.\frac{\partial f_1}{\partial t}\right|_C . \tag{73}$$

2.3.6 CRs as a fluid

From the respective CR transport equations in Sec. 2.3.5, we are now able to derive fluid equations describing the evolution of the CR quantities defined in Sec. 2.3.1. We present the results for both the one-moment and the two-moment approach (Pfrommer et al., 2017; Thomas and Pfrommer, 2019).

One-moment approach We multiply Eq. (66) by the proton energy $E_\mathrm{p}(p)$ and integrate the resulting equation over the entire momentum space, yielding (Pfrommer et al., 2017):

$$\frac{\partial \varepsilon_\mathrm{cr}}{\partial t} + \boldsymbol{\nabla}\cdot[(\boldsymbol{u}+\boldsymbol{v}_\mathrm{st})(P_\mathrm{cr}+\varepsilon_\mathrm{cr}) - \kappa_\varepsilon \boldsymbol{b}(\boldsymbol{b}\cdot\boldsymbol{\nabla}\varepsilon_\mathrm{cr})] = (\boldsymbol{u}+\boldsymbol{v}_\mathrm{st})\cdot\boldsymbol{\nabla}P_\mathrm{cr} + \Gamma_\mathrm{acc} + \Lambda_\mathrm{cr} + \Gamma_\mathrm{cr}. \tag{74}$$

Here, κ_ε denotes the kinetic-energy-weighted spatial diffusion coefficient, Γ_acc is the net energy-gain rate due to Fermi-II acceleration, and Γ_cr and Λ_cr account for several gain and loss processes of CRs, respectively. The second term on the LHS describes the advective transport of CR pressure and CR energy density with the total velocity $\boldsymbol{u}+\boldsymbol{v}_\mathrm{st}$ as well as the anisotropic diffusion of CR energy density along the mean magnetic field relative to the advection. The remaining term on the RHS accounts for volume work done by the CR pressure on the thermal gas ($\boldsymbol{u}\cdot\boldsymbol{\nabla}P_\mathrm{cr}$) and for the generation of Alfvén waves ($\boldsymbol{v}_\mathrm{st}\cdot\boldsymbol{\nabla}P_\mathrm{cr}$). The latter is always a loss term, which results from the following consideration (Pfrommer et al., 2017):

$$\boldsymbol{v}_\mathrm{st}\cdot\boldsymbol{\nabla}P_\mathrm{cr} = -\frac{\boldsymbol{B}}{\sqrt{\rho}}\frac{\boldsymbol{B}\cdot\boldsymbol{\nabla}P_\mathrm{cr}}{|\boldsymbol{B}\cdot\boldsymbol{\nabla}P_\mathrm{cr}|}\cdot\boldsymbol{\nabla}P_\mathrm{cr} = -\frac{1}{\sqrt{\rho}}\frac{(\boldsymbol{B}\cdot\boldsymbol{\nabla}P_\mathrm{cr})^2}{|\boldsymbol{B}\cdot\boldsymbol{\nabla}P_\mathrm{cr}|} < 0. \tag{75}$$

We can gain further insight into Eq. (74) by substituting the identity:

$$P_\mathrm{cr}\boldsymbol{\nabla}\cdot(\boldsymbol{u}+\boldsymbol{v}_\mathrm{st}) = \boldsymbol{\nabla}\cdot[(\boldsymbol{u}+\boldsymbol{v}_\mathrm{st})P_\mathrm{cr}] - (\boldsymbol{u}+\boldsymbol{v}_\mathrm{st})\cdot\boldsymbol{\nabla}P_\mathrm{cr}, \tag{76}$$

which yields:

$$\frac{\partial \varepsilon_\mathrm{cr}}{\partial t} + \boldsymbol{\nabla}\cdot[\varepsilon_\mathrm{cr}(\boldsymbol{u}+\boldsymbol{v}_\mathrm{st}) - \kappa_\varepsilon\boldsymbol{b}(\boldsymbol{b}\cdot\boldsymbol{\nabla}\varepsilon_\mathrm{cr})] = -P_\mathrm{cr}\boldsymbol{\nabla}\cdot(\boldsymbol{u}+\boldsymbol{v}_\mathrm{st}) + \Gamma_\mathrm{acc} + \Lambda_\mathrm{cr} + \Gamma_\mathrm{cr}. \tag{77}$$

In this representation, we see that the spatial transport of CR energy density is a superposition of advection with the reference frame moving at velocity $\boldsymbol{u} + \boldsymbol{v}_{\mathrm{st}}$ and anisotropic diffusion along the mean magnetic field relative to this reference frame.

The first term on the RHS describes the change of the CR energy density caused by compressive motions in the fluid and by interactions with gyro-resonant Alfvén waves. The signs of $\boldsymbol{\nabla} \cdot \boldsymbol{u}$ and $\boldsymbol{\nabla} \cdot \boldsymbol{v}_{\mathrm{st}}$ control whether the CRs gain or lose energy by these processes. Consequently, Eq. (18) describing the total MHD energy density must be extended to include a coupling term to the CR energy density that accounts for these gain and loss processes, thus ensuring energy conservation (cf. Eq. (89)).

Two-moment approach In addition to the CR quantities defined in Sec. 2.3.1, we introduced the CR energy flux density along the mean magnetic field:

$$f_{\mathrm{cr}} = \boldsymbol{b} \cdot \boldsymbol{f}_{\mathrm{cr}} = \int_0^\infty \mathrm{d}p \, 4\pi p^2 E(p) v f_1(p), \tag{78}$$

and the anisotropic CR pressure flux along the mean magnetic field:

$$K_{\mathrm{cr}} = \boldsymbol{b} \cdot \boldsymbol{K}_{\mathrm{cr}} = \int_0^\infty \mathrm{d}p \, 4\pi \frac{pv}{3} v f_1(p), \tag{79}$$

which are related by an EOS:

$$K_{\mathrm{cr}} = (\gamma - 1) f_{\mathrm{cr}}. \tag{80}$$

To derive the evolution equation for the CR energy density in the two-moment approach, we use the same procedure as we did in the one-momentum approach and multiply Eq. (72) with the proton energy $E_{\mathrm{p}}(p)$ and integrate over momentum space. This results in (Thomas and Pfrommer, 2019):

$$\frac{\partial \varepsilon_{\mathrm{cr}}}{\partial t} + \boldsymbol{\nabla} \cdot [\boldsymbol{u}(\varepsilon_{\mathrm{cr}} + P_{\mathrm{cr}}) + \boldsymbol{b} f_{\mathrm{cr}}] = \boldsymbol{u} \cdot \boldsymbol{\nabla} P_{\mathrm{cr}} + \left. \frac{\partial \varepsilon_{\mathrm{cr}}}{\partial t} \right|_C. \tag{81}$$

The interpretation is analogous to Eq. (74): f_{cr} is the CR energy flux density along the magnetic field, the CR energy density is advected with the thermal gas velocity $\boldsymbol{u}$ and is affected by adiabatic changes (first term on the RHS).

The evolution equation of the CR energy flux can be derived by calculating the $E_{\mathrm{p}}(p)\, v$ moment of Eq. (72), which yields (Thomas and Pfrommer, 2019):

$$\frac{\partial f_{\mathrm{cr}}}{\partial t} + \boldsymbol{\nabla} \cdot (\boldsymbol{u} f_{\mathrm{cr}}) + \frac{c^2}{3} \boldsymbol{b} \cdot \boldsymbol{\nabla} \varepsilon_{\mathrm{cr}} = -(\boldsymbol{b} \cdot \boldsymbol{\nabla} \boldsymbol{u}) \cdot (\boldsymbol{b} f_{\mathrm{cr}}) + \left. \frac{\partial f_{\mathrm{cr}}}{\partial t} \right|_C. \tag{82}$$

The third term on the LHS is a source term of CR energy density flux because the presence of an energy density gradient results in additional flux. The first term on the RHS represents a pseudo force.

For a detailed determination and interpretation of the various collision terms appearing in the two-momentum derivations, we refer the reader to Thomas and Pfrommer (2019), as this is beyond the scope of this work. Here, we only focus on the effects of implementing CR energy or entropy density as the evolving quantity, neglecting CR transport mechanisms like diffusion and streaming. Therefore, applying the two-moment method, which is much more computationally expensive, is not beneficial and may unnecessarily complicate our discussions.

2.4 One-moment CR-MHD

Here we introduce the full set of one-moment CR-MHD equations we employ in this work, and we specify associated thermal and non-thermal source terms. Further, we discuss the competing energy and entropy formulations for CR transport and how they are coupled to the MHD equations. Additionally, we present the extension of the existing energy-conserving numerical scheme to the entropy-conserving formulation of the CR transport equations.

In general, various CR transport phenomena influence how CRs are distributed in space once they leave their sources. This includes (but is not limited to) CR streaming or diffusion along magnetic field lines (Skilling, 1971; Zweibel, 2013), transport induced by magnetic field line wandering (Jokipii, 1966; Shalchi and Kourakis, 2007), CR interactions with turbulence (Shalchi, 2009; Yan and Lazarian, 2011), and guiding centre drifts (Gombosi, 2004; Schlickeiser and Jenko, 2010). In one of the common approximations, CRs are assumed to be co-moving with the bulk flow of the thermal particles and all additional transport process along or across the magnetic field are neglected, i.e. $\boldsymbol{v}_{\mathrm{st}} = 0$, $\kappa_{\varepsilon} = 0$ and $\Gamma_{\mathrm{acc}} = 0$ in Eq. (77). In this case, the evolution equation for the CR energy density reads as:

$$\frac{\partial \varepsilon_{\mathrm{cr}}}{\partial t} + \boldsymbol{\nabla} \cdot (\varepsilon_{\mathrm{cr}} \boldsymbol{u}) = -P_{\mathrm{cr}} \boldsymbol{\nabla} \cdot \boldsymbol{u} + \Gamma_{\mathrm{cr}} + \Lambda_{\mathrm{cr}}, \tag{83}$$

where $\boldsymbol{u}$ is the mean velocity of the thermal gas, P_{cr} is the CR pressure linked to the CR energy density $\varepsilon_{\mathrm{cr}}$ by an EOS:

$$P_{\mathrm{cr}} = (\gamma_{\mathrm{cr}} - 1)\varepsilon_{\mathrm{cr}}, \tag{84}$$

$\gamma_{\mathrm{cr}} = 4/3$ is the adiabatic index of the CRs, and non-adiabatic gain and loss processes of CR energy are represented by Γ_{cr} and Λ_{cr}, respectively. The term $\boldsymbol{\nabla} \cdot (\varepsilon_{\mathrm{cr}} \boldsymbol{u})$ describes the advection of CR energy with the gas flow, while the term $P_{\mathrm{cr}} \boldsymbol{\nabla} \cdot \boldsymbol{u}$ on the RHS of Eq. (83) states that CR energy density is subject to adiabatic changes. This adiabaticity of the CRs suggests the definition of a proxy for the CR entropy given by (cf. Eq. (24))

$$K_{\mathrm{cr}} = P_{\mathrm{cr}} / \rho^{\gamma_{\mathrm{cr}}}, \tag{85}$$

where ρ is the gas mass density. We call K_{cr} the *specific CR entropy*, or *CR entropy* for short. The evolution equation for K_{cr} is:

$$\frac{\partial (\rho K_{\mathrm{cr}})}{\partial t} + \boldsymbol{\nabla} \cdot (\rho K_{\mathrm{cr}} \boldsymbol{u}) = \frac{\gamma_{\mathrm{cr}} - 1}{\rho^{\gamma_{\mathrm{cr}} - 1}} (\Gamma_{\mathrm{cr}} + \Lambda_{\mathrm{cr}}), \tag{86}$$

and it states that CR entropy is solely advected with the gas-flow and is a conserved quantity in the absence of any explicit gains or losses of CR energy. The CR energy density does not have this favourable property and is a non-conserved quantity because of the adiabatic term which cannot be cast into a total-flux divergence form. This difference between the energy and entropy formulations for CR transport also influences the design of numerical schemes that implement these equations. While standard finite-volume schemes can be readily applied to the entropy equation (86), these schemes cannot be directly applied to the adiabatic term of the CR energy

equation (83) and other discretizations need to be made (Kudoh and Hanawa, 2016; Gupta et al., 2021).

CR exert forces on the thermal particles and are thus represented through their pressure in the momentum and energy equations in the MHD system of equations (see Sec. 2.1) that neglect gravity:

$$\frac{\partial \rho}{\partial t} + \boldsymbol{\nabla} \cdot (\rho \boldsymbol{u}) = 0, \tag{87}$$

$$\frac{\partial (\rho \boldsymbol{u})}{\partial t} + \boldsymbol{\nabla} \cdot (\rho \boldsymbol{u}\boldsymbol{u} + P_{\rm tot}\mathbf{1} + \boldsymbol{B}\boldsymbol{B}) = \mathbf{0}, \tag{88}$$

$$\frac{\partial \varepsilon}{\partial t} + \boldsymbol{\nabla} \cdot [(\varepsilon + P_{\rm tot})\boldsymbol{u} + \boldsymbol{B}(\boldsymbol{u} \cdot \boldsymbol{B})] = P_{\rm cr} \boldsymbol{\nabla} \cdot \boldsymbol{u} + \Gamma_{\rm th} + \Lambda_{\rm th}, \tag{89}$$

$$\frac{\partial \boldsymbol{B}}{\partial t} + \boldsymbol{\nabla} \cdot (\boldsymbol{B}\boldsymbol{u} + \boldsymbol{u}\boldsymbol{B}) = 0, \tag{90}$$

where $\boldsymbol{B}$ is the magnetic field, $\Gamma_{\rm th}$ and $\Lambda_{\rm th}$ are heating and cooling terms affecting the thermal energy density $\varepsilon_{\rm th}$, ε is the total MHD energy density given by :

$$\varepsilon = \frac{\rho}{2}\boldsymbol{u}^2 + \varepsilon_{\rm th} + \frac{\boldsymbol{B}^2}{2}, \tag{91}$$

and $P_{\rm tot}$ is the total pressure of the composite fluid of CRs, thermal gas, and magnetic field and is given by:

$$P_{\rm tot} = P_{\rm th} + P_{\rm cr} + \frac{\boldsymbol{B}^2}{2}. \tag{92}$$

Similar to the CRs, thermal energy density and thermal pressure are linked by an EOS:

$$P_{\rm th} = (\gamma_{\rm th} - 1)\varepsilon_{\rm th}, \quad \text{where} \quad \gamma_{\rm th} = 5/3. \tag{93}$$

In this work, we explicitly determine the CR loss term $\Lambda_{\rm cr}$ composed of Coulomb and hadronic losses from Eqs. (60) and (61) assuming equilibrium between injected and cooled CR energy. This results in (see Enßlin et al., 2007; Pfrommer et al., 2017, for a detailed derivation):

$$\Lambda_{\rm cr} = \Lambda_{\rm cr,\,C} + \Lambda_{\rm cr,\,H} = -\lambda_{\rm cr} n_{\rm e} \varepsilon_{\rm cr}, \tag{94}$$

where $\lambda_{\rm cr} = 1.022 \times 10^{-15}\,{\rm cm^3\,s^{-1}}$ is the rate coefficient for collisional CR energy loss. We approximate the rate of CR energy gain $\Gamma_{\rm cr}$ through acceleration in core-collapse SNe by:

$$\Gamma_{\rm cr} = \zeta_{\rm SN}\, \epsilon_{\rm SN}\, \dot{m}_*, \tag{95}$$

where $\zeta_{\rm SN}$ is the fraction of SN energy that gets converted to CR energy, $\dot{m}_*$ is the star-formation rate (SFR), and $\epsilon_{\rm SN} = 10^{49}\,{\rm erg\,M_\odot}^{-1}$ denotes the SN energy per solar mass. To determine the latter, we assume a Kroupa (Kroupa, 2001) initial mass function and that stars above $8\,{\rm M_\odot}$ explode as SNe, injecting an energy of 10^{51} erg.

Provided that $\Lambda_{\rm cr,\,C}$ is fully thermalized and approximately 1/6 of the hadronic collisions of CR ions result in secondary electrons, a large fraction of which in turn cool completely by Coulomb losses that again heat the surrounding plasma, the heating rate of the thermal gas is:

$$\Gamma_{\rm th} = -\Lambda_{\rm cr,\,C} - \Lambda_{\rm cr,\,H}/6 = \lambda_{\rm th} n_{\rm e} \varepsilon_{\rm cr}, \tag{96}$$

where $\lambda_{\mathrm{th}} = 4.02 \times 10^{-16}\,\mathrm{cm^3\,s^{-1}}$ is the rate coefficient for collisional heating of the thermal gas by CRs. Finally, the radiative-cooling term Λ_{th} is modelled following the approach of Springel and Hernquist (2003).

Note that the total energy is conserved in the combined set of MHD equations together with the CR energy equation (83) in the absence of explicit sources or sinks of CR or thermal energy. This cannot be guaranteed if the CR entropy equation (86) is used, and thus energy errors will inevitably build up in simulations that employ this formulation for CR transport. Hence, the decision between the CR energy and entropy formulations is also a decision which conservation property is regarded to be more valuable. A priori, neither of them is more favourable.

3 Numerics of CR-MHD

The numerical treatment of CR-MHD requires the numerical solution of the associated system of coupled hyperbolic partial differential equations (PDEs). In Sec. 3.1, we first consider the so-called finite-volume method (FVM), which is particularly useful to solve hyperbolic PDEs. Riemann solvers form an intrinsic component of this solution procedure, and we introduce their basic structure in Sec. 3.2. In Sec. 3.3, we describe some key points of the Arepo code providing the numerical framework we employ and extend in this work to perform our simulations. Finally, we brief our implementation of CR physics into the existing MHD framework of Arepo in Sec. 3.4.

3.1 Finite-Volume Method

To solve the set of ideal MHD equations, we employ a FVM as part of the Arepo code. Here, the computational domain is divided into a finite number of disjoint numerical cells and the physical quantities associated with a given numerical cell are modified by fluxes into and out of this cell. For now, we consider only the equations of ideal MHD, and in Sec. 3.4.1 we extend the methods described here to include CR physics. Neglecting gravity, we can re-write the set of ideal MHD equations in the more compact form:

$$\frac{\partial}{\partial t}\boldsymbol{U} + \boldsymbol{\nabla}\cdot\boldsymbol{F} = \boldsymbol{0}, \tag{97}$$

where $\boldsymbol{U} \equiv \boldsymbol{U}(\boldsymbol{r}, t)$ is the state vector of the fluid's conserved quantities, $\boldsymbol{F}(\boldsymbol{U}) \equiv \boldsymbol{F}(\boldsymbol{U}(\boldsymbol{r}, t))$ is a function describing the spatial flux:

$$\boldsymbol{U} = \begin{pmatrix} \rho \\ \rho\boldsymbol{u} \\ \varepsilon \\ \boldsymbol{B} \end{pmatrix}, \quad \boldsymbol{F} = \begin{pmatrix} \rho\boldsymbol{u} \\ \rho\boldsymbol{u}\boldsymbol{u} + P\boldsymbol{1} + \boldsymbol{B}\boldsymbol{B} \\ (\varepsilon + P)\boldsymbol{u} + \boldsymbol{B}(\boldsymbol{u}\cdot\boldsymbol{B}) \\ \boldsymbol{B}\boldsymbol{u} + \boldsymbol{u}\boldsymbol{B} \end{pmatrix}, \tag{98}$$

and all symbols retain their meaning from the definitions in Sec. 2.1.2. The basic idea of the FVM is then to describe the state vector $\boldsymbol{U}$ as a finite set of cell-averaged quantities at discrete time steps rather than using continuous functions. For the sake of clarity, we focus on the 1D case in the following.

We define a (numerical) cell i as the interval $[x_{i-1/2}, x_{i+1/2}]$ with centre x_i and extent $\Delta x_i = x_{i+1/2} - x_{i-1/2}$. Moreover, we define a time step as $\Delta t = t^{n+1} - t^n$ where n denotes a discrete instant in time. The cell average of the state vector $\boldsymbol{U}$ at time t^n is defined as:

$$\boldsymbol{U}_i^n = \frac{1}{\Delta x_i}\int_{x_{i-1/2}}^{x_{i+1/2}} \boldsymbol{U}\,\mathrm{d}x. \tag{99}$$

We integrate Eq. (97) over the extent of cell i and for a single time step and insert Eq. (99), yielding an explicit update scheme for the state vector (Toro, 2009):

$$\boldsymbol{U}_i^{n+1} = \boldsymbol{U}_i^n - \frac{\Delta t}{\Delta x}\left(\boldsymbol{F}_{i+1/2} - \boldsymbol{F}_{i-1/2}\right), \tag{100}$$

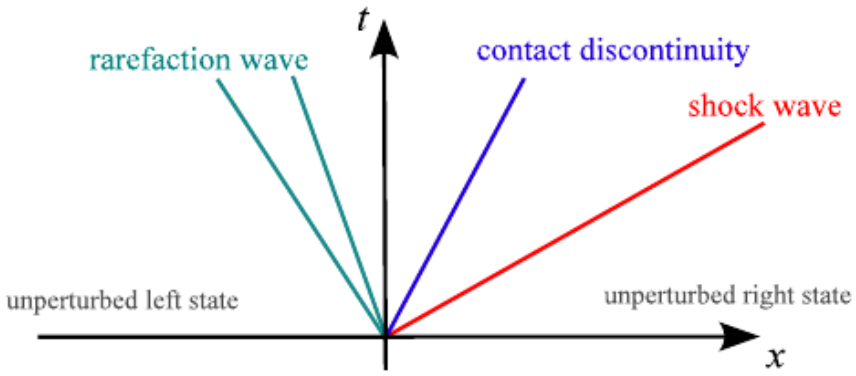

Figure 3: Wave fan of the solution to the Riemann problem. The central contact wave separates the original fluid phases. On the left and the right, there is either a shock or a rarefaction wave (Pfrommer, 2022b).

where we have defined the temporal integral average of the fluxes (Toro, 2009):

$$\boldsymbol{F}_{i+1/2} = \frac{1}{\Delta t} \int_{t^n}^{t^{n+1}} \mathrm{d}t \, \boldsymbol{F}(\boldsymbol{U}(x_{i+1/2}, t)). \tag{101}$$

$\boldsymbol{F}_{i-1/2}$ describes the flux that enters cell i at the left interface, and $\boldsymbol{F}_{i+1/2}$ is the flux leaving the cell to the right.

We cannot calculate the averaged state vector $\boldsymbol{U}_i^{n+1}$ for the next time step since we do not know the exact value of $\boldsymbol{U}(x_{i+1/2}, t)$ and therefore cannot calculate the occurring averages. However, an approximate solution to Eq. (101) can be obtained by so-called Riemann solvers, which we discuss next. The idea of using the solution of the Riemann problem at this point dates back to Godunov and Bohachevsky (1959), which is why this method is also referred to as *Godunov's method*.

3.2 Riemann solvers

In general, a Riemann solver is a numerical method for solving the Riemann problem, which is an initial value problem for a set of conservation laws such as the (homogeneous) equations of MHD:

$$\frac{\partial}{\partial t}\boldsymbol{U} + \frac{\partial}{\partial x}\boldsymbol{F} = \boldsymbol{0}, \tag{102}$$

subject to the discontinuous initial conditions:

$$\boldsymbol{U}(x, 0) = \boldsymbol{U}^0(x) = \begin{cases} \boldsymbol{U}_\mathrm{L}, & x < 0 \\ \boldsymbol{U}_\mathrm{R}, & x > 0\,. \end{cases} \tag{103}$$

Here, the indices L and R indicate the left and right sides of the discontinuity, respectively, which are assumed to be infinite half-spaces in which the respective constant initial conditions hold everywhere. This setup is a slight generalization of the shock-tube problem we describe and extensively simulate in Sec. 4.2.

Riemann solvers calculate or approximate the fluxes across this discontinuity. The resulting fluxes are then used in Eq. (100) to advance the state vector in time.

These fluxes are calculated at every cell interface in the computational domain by invoking the Riemann solver at each individual cell interface with different values for $\boldsymbol{U}_\mathrm{L}$ and $\boldsymbol{U}_\mathrm{R}$. To reduce the complexity of our discussion, we focus in the following on a single Riemann problem for the application of the Riemann solver on a single cell interface.

The solution of the Riemann problem is composed of multiple (shock) waves which form a wave pattern whose complexity depends on the underlying physics. Figure 3 outlines the solution to an idealized and purely hydrodynamic Riemann problem which, in this particular case, consists of three separated waves, the so-called Riemann fan: a shock that propagates to the right, a rarefaction wave propagating to the left, and a CD (see Sec. 2.2) that separates the original fluid phases.

While no analytical but iteratively exact solutions exist for the idealized hydrodynamic Riemann problem (see e.g. Godunov et al., 1976; Chorin, 1976; van Leer, 1979), the situation is even more complex for problems arising in the realm of MHD. There, finding exact or iterative solutions to the Riemann problem is computationally expensive because of the significantly higher number of coupled PDEs. Riemann solvers based on this idea are rarely used in practice, although they are described in the literature (see e.g. Torrilhon et al., 2002; Takahashi et al., 2014). Instead, non-iterative approximate Riemann solvers were developed.

Essentially, there are two ways to gain approximate solutions to the Riemann problem: to approximate the states and the corresponding fluxes in the wave pattern or to approximate the numerical flux directly (Toro, 2009). Pioneering work has been done in this context by Harten, Lax and van Leer (Harten et al., 1983) who developed the HLL Riemann solver named after them. They assumed a two-wave configuration that separates three constant regions in the computational domain, and the entire Riemann fan is represented by a single averaged state. Their approach yields an approximate, but closed-form solution to the Riemann problem. This assumption only accounts for two waves in the wave pattern and is, consequently, only a correct representation of the solution to the Riemann problem for hyperbolic systems consisting of two evolution equations. For hyperbolic systems with more than two waves in the wave pattern (cf. Sec. 2.1.3), some waves are unaccounted for, which ultimately results in an increased numerical diffusivity (Toro, 2009).

Based on the HLL concept, further numerical methods were developed which improved the accuracy and robustness of the approximation, e.g. the HLLE and HLLEM schemes (Einfeldt, 1988; Einfeldt et al., 1991), which additionally estimate the speed of the different waves. Toro et al. (1994) introduced the HLLC Riemann solver which assumes a Riemann fan consisting of two intermediate states emerging from a three-wave model (see Fig. 4, left). The additional wave is a contact wave, indicated by the C in HLLC. For purely hydrodynamic systems covered by three equations (like the Euler equations), this solver is a complete Riemann solver because the wave pattern of the Riemann fan contains all characteristics of the exact Riemann problem. For systems with more than three distinct characteristics (like the ideal MHD equations), however, the solver becomes incomplete, resulting in weak resolution of the intermediate wave and thus worse approximations (Toro, 2009).

Miyoshi and Kusano (2005) further enhanced the HLL concept and developed

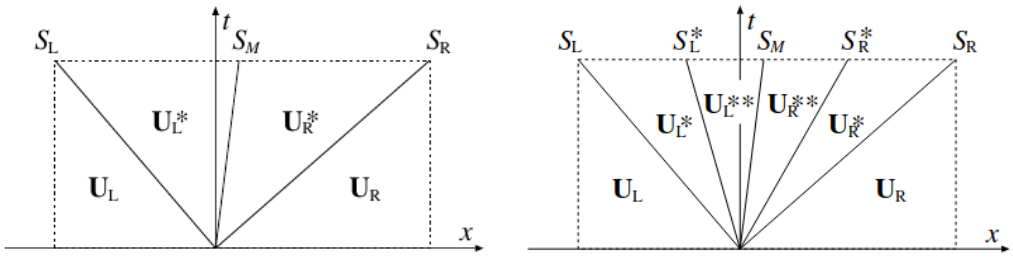

Figure 4: Riemann-fan structure of the HLLC Riemann solver (left) and the HLLD Riemann solver (right) (Miyoshi and Kusano, 2005).

a method that provides excellent results especially in the context of MHD. Since their solver exactly resolves isolated discontinuities in MHD systems, it was named HLLD Riemann solver, and we use this approach as part of the Arepo code in this work. It extends the HLLC Riemann solver by accounting for two additional states in the wave pattern. These states and the corresponding waves in the wave pattern represent Alfvén waves (while the slow magneto-sonic waves remain unconsidered, cf. Sec. 2.1.3). Thus, the HLLD approach considers a division of the Riemann fan into four intermediate states which are separated by three waves represented by their respective speed S in Fig. 4: two Alfvén waves propagating to the left (S_L^*) and to the right (S_R^*), respectively, and a contact wave S_M. The outermost waves S_L and S_R, which represent a shock and/or a rarefaction wave, remain their meaning. From the given initial conditions $\boldsymbol{U}_\mathrm{L}$ and $\boldsymbol{U}_\mathrm{R}$, the algorithm first calculates the state vectors of the intermediate states $\boldsymbol{U}_\mathrm{L}^*$, $\boldsymbol{U}_\mathrm{L}^{**}$, $\boldsymbol{U}_\mathrm{R}^*$, and $\boldsymbol{U}_\mathrm{R}^{**}$ (see Miyoshi and Kusano, 2005, for all details of the algorithm). The fluxes through the respective interfaces can then be calculated explicitly for $k \in \{\mathrm{L}, \mathrm{R}\}$ by:

$$\boldsymbol{F}_k^* = \boldsymbol{F}_k + S_k(\boldsymbol{U}_k^* - \boldsymbol{U}_k), \tag{104}$$

$$\boldsymbol{F}_k^{**} = \boldsymbol{F}_k^* + S_k^*(\boldsymbol{U}_k^{**} - \boldsymbol{U}_k^*). \tag{105}$$

Drawing on the results in Sec. (2.1.3), we find the respective speeds of the Alfvén modes for $k \in \{\mathrm{L}, \mathrm{R}\}$:

$$S_k^* = S_\mathrm{M} \mp \frac{B_x}{\sqrt{\rho_k^*}}, \tag{106}$$

and the average normal velocity across the Riemann fan is given by (Miyoshi and Kusano, 2005):

$$S_\mathrm{M} = \frac{(S_\mathrm{R} - u_\mathrm{R})\rho_\mathrm{R} u_\mathrm{R} - (S_\mathrm{L} - u_\mathrm{L})\rho_\mathrm{L} u_\mathrm{L} - P_\mathrm{R} + P_\mathrm{L}}{(S_\mathrm{R} - u_\mathrm{R})\rho_\mathrm{R} - (S_\mathrm{L} - u_\mathrm{L})\rho_\mathrm{L}}. \tag{107}$$

We estimate the velocities of the enclosing waves by:

$$S_\mathrm{L} = \min\left[u_\mathrm{L} - c_{\mathrm{f,L}},\, u_\mathrm{R} - c_{\mathrm{f,R}}\right], \tag{108}$$

$$S_\mathrm{R} = \max\left[u_\mathrm{L} + c_{\mathrm{f,L}},\, u_\mathrm{R} + c_{\mathrm{f,R}}\right], \tag{109}$$

and we have thus found an approximate solution for the fluxes in Eq. (100), which

can be expressed as:

$$\boldsymbol{F}^{\mathrm{HLLD}}(\boldsymbol{U}_{\mathrm{L}}, \boldsymbol{U}_{\mathrm{R}}) = \begin{cases} \boldsymbol{F}_{\mathrm{L}}, & S_{\mathrm{L}} > 0 \\ \boldsymbol{F}^{*}_{\mathrm{L}}, & S_{\mathrm{L}} \leq 0 \leq S^{*}_{\mathrm{L}} \\ \boldsymbol{F}^{**}_{\mathrm{L}}, & S^{*}_{\mathrm{L}} \leq 0 \leq S_{\mathrm{M}} \\ \boldsymbol{F}^{**}_{\mathrm{R}}, & S_{\mathrm{M}} \leq 0 \leq S^{*}_{\mathrm{R}} \\ \boldsymbol{F}^{*}_{\mathrm{R}}, & S^{*}_{\mathrm{R}} \leq 0 \leq S_{\mathrm{R}} \\ \boldsymbol{F}_{\mathrm{R}}, & S_{\mathrm{R}} < 0\,. \end{cases} \tag{110}$$

3.3 Numerical framework: Arepo

We employ the massively parallel adaptive moving-mesh code Arepo to perform the various simulations in this work. We use this section to summarize some relevant algorithms and key feature of this code. Our discussion is based on Springel (2010), Pakmor and Springel (2013), and Weinberger et al. (2020).

3.3.1 Code features

Spatial discretization Arepo is a mesh code that discretizes the computational domain using a so-called Voronoi tessellation, which consists of distinct Voronoi cells (VCs). A VC is constructed around a mesh-generating point (MGP) and contains those spatial points that are closer to a given MGP than to any other MGP. Consequently, any connecting line between the MGPs of adjacent VCs is normal to the interface of the corresponding VCs. This property simplifies the exchange of fluxes between neighbouring cells because only its normal component has to be considered.

The set of exactly these connecting lines forms a so-called Delaunay triangulation. Mathematically, such a triangulation is defined by the fact that the circumcircles (or circumspheres in 3D) of these triangles (or tetrahedra in 3D) do not contain any other MGP except those by which they are defined. This property uniquely determines the triangulation of the computational domain, irrespective of the order the MGPs are evaluated for mesh generation.

Figure 5 shows an example of a 2D Voronoi tessellation and corresponding Delaunay triangulation. Clearly, the number of MGPs determines the resolution of a simulation.

Moving mesh A special feature of Arepo is the employment of the moving-mesh approach. Here, the MGPs are advected with the bulk velocity $\boldsymbol{u}$ of the hydrodynamical flow inside the associated computational cell, which leads to an approximate equal-mass discretization of the system. This method is implemented in Arepo using a semi-Lagrangian approach because exchange of mass between computational cells is still possible while the mesh is moving with the flow. This is in contrast to Eulerian codes where the computational grid is fixed. In comparison to fully-Lagrangian flows, slight deviations of the velocity of the MGPs from the bulk velocity $\boldsymbol{u}$ are allowed. This property is used in Arepo to steer the motion of the VCs such that the VCs attain certain desired properties. For example, Springel (2010) presents an algorithm to adjust the mesh motion in order to form rounder

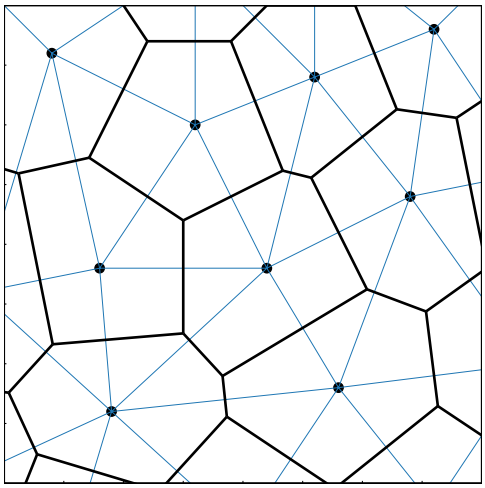

Figure 5: Exemplary 2D Voronoi tessellation (black lines) and corresponding Delaunay triangulation (blue lines) of the computational domain. Mesh-generating points are shown as black dots.

VCs and to reduce the probability of ill-formed or numerically precarious VCs in the simulation. Lagrangian codes provide the tremendous advantage of being Galilean invariant, which is especially important for simulations of astrophysical flows where supersonic velocities are frequently encountered.

The finite-volume algorithm needs to be adapted to account for the moving mesh. *Reynolds transport theorem* states that we need to account for an additional geometrical flux in the finite-volume algorithm which originates from the mesh motion itself: consider a standing fluid parcel which is discretized by a moving mesh. In this situation, physical quantities are still exchanged over mesh interfaces solely due to the mesh motion. The resulting total flux is a superposition of the physical flux from Eq. (98) and the geometrical flux from Reynolds transport theorem:

$$\boldsymbol{F}_{\mathrm{m}} = \boldsymbol{F}_{\mathrm{s}} - \boldsymbol{U}\boldsymbol{w}. \tag{111}$$

The most straightforward approach to solve the Riemann problem in the frame of the static mesh and subsequently advect the solution with the moving mesh proves to be problematic for the HLLD Riemann solver. The MGPs of the cells are advected with the gas flow inside a cell, and thus the relative velocity of flux and interface is $\boldsymbol{w}-\boldsymbol{u} \approx \boldsymbol{0}$, resulting in very little flux across the interface. The HLLD solver provides only an approximation of the flux, and its output is subject to additional numerical diffusivity when calculating the flux in the static reference frame. Consequently, the error of the flux approximation can be larger than the actual flux, which in turn can lead to an unphysical inversion of the flux at the interface and destroy the upwind property of the algorithm (Pakmor et al., 2011). We can avoid this issue considering the flux across an interface in the reference frame of the mesh, thus reducing numerical diffusivity. Therefore, we first transform the system into the mesh frame:

$$\boldsymbol{U}' = \begin{pmatrix} \rho \\ \rho(\boldsymbol{u}-\boldsymbol{w}) \\ \varepsilon' \\ \boldsymbol{B} \end{pmatrix}, \quad \boldsymbol{F}'(\boldsymbol{U}') = \begin{pmatrix} \rho(\boldsymbol{u}-\boldsymbol{w}) \\ \rho(\boldsymbol{u}-\boldsymbol{w})(\boldsymbol{u}-\boldsymbol{w}) + P\boldsymbol{1} + \boldsymbol{B}\boldsymbol{B} \\ (\varepsilon' + P)\boldsymbol{u} + \boldsymbol{B}\left[(\boldsymbol{u}-\boldsymbol{w})\cdot\boldsymbol{B}\right] \\ \boldsymbol{B}(\boldsymbol{u}-\boldsymbol{w}) + (\boldsymbol{u}-\boldsymbol{w})\boldsymbol{B} \end{pmatrix}, \tag{112}$$

where $\varepsilon' = \varepsilon - \rho\boldsymbol{u}^2/2 + \rho(\boldsymbol{u}-\boldsymbol{w})^2/2$. We apply the HLLD Riemann solver in this moving frame and transform the obtained fluxes back to the reference frame of the mesh:

$$\boldsymbol{F}_{\mathrm{m}}(\boldsymbol{U}_{\mathrm{m}}) = \boldsymbol{F}'(\boldsymbol{U}') + \begin{pmatrix} 0 \\ \rho\boldsymbol{w}(\boldsymbol{u}-\boldsymbol{w}) \\ \rho\boldsymbol{u}\boldsymbol{w}(\boldsymbol{u}-\boldsymbol{w}) - \frac{1}{2}\rho\boldsymbol{w}^2(\boldsymbol{u}-\boldsymbol{w}) + P\boldsymbol{w} - \boldsymbol{B}(\boldsymbol{w}\cdot\boldsymbol{B}) \\ -\boldsymbol{w}\boldsymbol{B} \end{pmatrix}. \quad (113)$$

This procedure always maintains the upwind property of the algorithm and improves its general stability and accuracy (Pakmor et al., 2011).

Mesh refinement The mesh deforms steadily and adapts its topology as a consequence of the moving MGPs without causing undesirable effects such as mesh tangling due to the mathematical properties of the Voronoi tessellation described previously (Springel, 2010). However, over many simulation time steps, the cells may deviate from their intended mass content or size. To address this, Arepo provides the mechanism of *local* mesh refinement and de-refinement without triggering any global adaptions of the mesh. If this option is enabled, Arepo checks various refinement criteria for each active cell in the simulation. One important criteria checks whether the volume of neighbouring cells differs by more than a user-defined factor. If this is the case, the affected cells are split into a pair of nearly identical cells, adding a mesh generating point without influencing the geometry of other adjacent cells. This method can be used to increase the resolution of the mesh around regions of interest, such as shocks. Because this refinement increases the numerical resolution only locally, the overall increase in computation cost of the simulation is reduced in comparison to a global refinement of all computational cells. We make use of this refinement feature in Sec. 4.4.2.

Magnetic-divergence cleaning While the analytic MHD equations automatically obey the divergence constraint for the magnetic field, $\boldsymbol{\nabla}\cdot\boldsymbol{B} = 0$, numerical errors originating from the discretization of the MHD equation can introduce local violations of this condition in a simulation. In order to prevent a catastrophic build-up of these errors, Arepo uses the divergence-cleaning method introduced by Powell et al. (1999) and implemented by Pakmor and Springel (2013). The basic idea of this method is to drop the constraint of vanishing divergence of the magnetic field in the derivation of the ideal MHD equations and collect the terms containing $\boldsymbol{\nabla}\cdot\boldsymbol{B}$ in additional source terms in the momentum, energy, and induction equations:

$$\frac{\partial(\rho\boldsymbol{u})}{\partial t} + \boldsymbol{\nabla}\cdot(\rho\boldsymbol{u}\boldsymbol{u} + P_{\mathrm{tot}}\mathbf{1} - \boldsymbol{B}\boldsymbol{B}) = -(\boldsymbol{\nabla}\cdot\boldsymbol{B})\,\boldsymbol{B}, \quad (114)$$

$$\frac{\partial\varepsilon}{\partial t} + \boldsymbol{\nabla}\cdot[(\varepsilon+P)\boldsymbol{u} - \boldsymbol{B}(\boldsymbol{u}\cdot\boldsymbol{B})] = -(\boldsymbol{\nabla}\cdot\boldsymbol{B})\,(\boldsymbol{u}\cdot\boldsymbol{B}), \quad (115)$$

$$\frac{\partial\boldsymbol{B}}{\partial t} + \boldsymbol{\nabla}\cdot(\boldsymbol{B}\boldsymbol{u} - \boldsymbol{u}\boldsymbol{B}) = -(\boldsymbol{\nabla}\cdot\boldsymbol{B})\,\boldsymbol{u}. \quad (116)$$

These equations in combination with the continuity equation (6) yield an evolution equation for the divergence of the magnetic field (Powell et al., 1999):

$$\frac{\mathrm{d}}{\mathrm{d}t}(\boldsymbol{\nabla}\cdot\boldsymbol{B}) = -(\boldsymbol{\nabla}\cdot\boldsymbol{B})(\boldsymbol{\nabla}\cdot\boldsymbol{u}), \quad (117)$$

which is identical with the statement that $\boldsymbol{\nabla} \cdot \boldsymbol{B}/\rho$ is a passively advected scalar and thus stays constant along particle trajectories. If one can ensure in the initial conditions $\boldsymbol{\nabla} \cdot \boldsymbol{B} = 0$, this remains true for any other time. In practice, numerical inaccuracies prevent these initial conditions from being met exactly. For smooth flows where $\boldsymbol{\nabla} \cdot \boldsymbol{u} \approx 0$, the magnetic divergence stays roughly constant in time, and the advective nature of Eq. (117) prevents local magnetic divergence from further growing. In regions where $\boldsymbol{\nabla} \cdot \boldsymbol{u} \approx \text{const.} \neq 0$, we find using the method of lines:

$$\boldsymbol{\nabla} \cdot \boldsymbol{B} = (\boldsymbol{\nabla} \cdot \boldsymbol{B}_0) \exp\left[-(\boldsymbol{\nabla} \cdot \boldsymbol{u})t\right]. \tag{118}$$

Hence, diverging flows exponentially suppress the growth of magnetic divergence, while in converging flows, e.g. in shocks, $\boldsymbol{\nabla} \cdot \boldsymbol{B}$ increases exponentially.

The magnetic divergence in the additional source terms is then calculated for each cell i by:

$$\boldsymbol{\nabla} \cdot \boldsymbol{B}_i = \frac{1}{V_i} \sum_j \boldsymbol{B} \cdot \boldsymbol{n}\, A_{ij}\,, \tag{119}$$

where the sum extends over all adjacent cells j, V_i is the volume of cell i, A_{ij} is the area of the interface of cells i and j, $\boldsymbol{n}$ is the normal vector to this interface, and $\boldsymbol{B} \cdot \boldsymbol{n} = (B_{n,\mathrm{L}} + B_{n,\mathrm{R}})/2$ is the average of the normal magnetic-field components left and right of the interface to cell j.

3.3.2 Treatment of source terms

Gravity sources So far, we did not specify how to treat the gravity source terms in the momentum equation (8) and the energy equation (18). The HLLD Riemann solver only gives a solution to the homogeneous set of MHD equations. Hence, we add these sources separately following the so-called *operator-split* method. We first apply the sources for half a time step at the beginning of the step. Subsequently, we solve the ideal MHD equations in its homogeneous form and advance the system in time for a full step. Finally, the gravity terms are applied for another one-half time step. This procedure represents a second-order accurate *leap-frog scheme* (see e.g. Pfrommer, 2022b, for details).

Determining the gravitational potential Φ by direct summation, where each particle in the simulation directly contributes to the gravitational potential of every other particle, is computationally intractable for high-resolution simulations. The computational cost for this summation technique scales as N^2 where N is the number of particles in the simulation. While direct summation results in highly accurate values for the potential, the costs become unbearable once $N > 10^6$ because of this scaling. To circumvent this limitation, Arepo employs the so-called tree-particle-mesh approach, a dual method composed of a tree algorithm and a particle-mesh algorithm.

In general, tree algorithms group distant particles into nodes and calculate their contribution to the gravitational force as the collective effect of their centre of mass. Consequently, tree algorithms can cover a wide dynamicalrange, but are comparatively slow due to the fact that they consider every particle in the simulation and that the tree must be re-generated at each time step.

Particle-mesh algorithms transform the Poisson equation into Fourier space:

$$-k^2\Phi = 4\pi G\rho, \tag{120}$$

solve the algebraic equation for the gravitational potential, and use an inverse Fourier transform to obtain the potential field. This method is simple and very fast, but restricted to a uniform Cartesian mesh, limiting its dynamic range dramatically.

Arepo combines the advantages of both methods to overcome the shortcomings of the other. Gravitational forces are split into long-range and short-range contributions computed with the particle-mesh and the tree approach, respectively. The tree algorithm simply ignores contributions of nodes or particles that are far away, which speeds up the procedure significantly. The neglected force contribution is then provided by a particle-mesh algorithm.

Radiative cooling The explicit cooling $\Lambda_{\rm th}$ in Eq. (89) describes radiative cooling of the thermal gas and is determined by an iterative root-finding algorithm applied to the implicit equation (Weinberger et al., 2020):

$$u' - u^n - \Delta t\,\frac{\Lambda(u')}{\rho} = 0, \tag{121}$$

where Λ is the cooling function introduced by Springel and Hernquist (2003), and u^n and u' denote the specific internal energy of the thermal gas at the beginning and the end of the step, respectively.

3.3.3 Gradient estimation

Each cell in the computational domain is characterized by the primitive variables $\boldsymbol{W} = (\rho, \boldsymbol{u}, P_{\rm th}, \boldsymbol{B})^{\rm T}$, which can be considered as volume-averaged values or (in a seconder-order accurate scheme) the values of the underlying fields as evaluated at the cell's centre of mass (COM). The conserved variables $\boldsymbol{U}$ are calculated straightforwardly from the primitive variables:

$$\boldsymbol{U} = \begin{pmatrix} W_1 \\ W_1 W_2 \\ W_1 W_2^2/2 + W_3/(\gamma_{\rm th}-1) + W_4^2/2 \\ W_4 \end{pmatrix}. \tag{122}$$

Consequently, it suffices to specify $\boldsymbol{W}$ in the initial conditions of a simulation, and Arepo computes the conserved quantities after the initial mesh generation when the cell volumes are known.

We use the primitive variables as inputs to the HLLD Riemann solver to obtain approximate solutions to the local Riemann problems at each interface of a cell. Therefore, we need a suitable extrapolation of the primitives from the centre of cell i to the geometric centre $\boldsymbol{f}_{ij}$ of the interface of cell i and j. We denote the vector containing these extrapolated values as $\boldsymbol{W}_{ij}$. In the following, we present the method for gradient estimation developed and implemented in Arepo by Pakmor et al. (2016b).

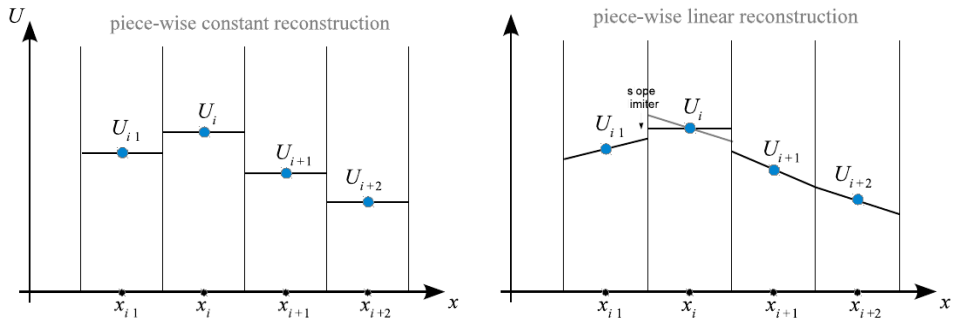

Figure 6: Examples of fluid-state reconstructions inside a numerical cell. The left plot shows a piece-wise constant reconstruction, the right plot a piece-wise linear reconstruction (Pfrommer, 2022b).

Unlike the original approach by Godunov, we use a piece-wise linear reconstruction of the quantities inside a cell (see Fig. 6, right). We approximate the quantity $q(\boldsymbol{r})$ for an arbitrary point $\boldsymbol{r}$ within the cell by:

$$q(\boldsymbol{r}) = q(\boldsymbol{s}_i) + (\boldsymbol{r} - \boldsymbol{s}_i)\,(\boldsymbol{\nabla} q)_i \;, \tag{123}$$

where $\boldsymbol{s}_i$ is the COM of cell i. To estimate the occurring gradient, we require that the linear extrapolation of the respective quantity in cell i to the COM of cell j agrees with the actual value found at $q(\boldsymbol{s}_j)$:

$$q(\boldsymbol{s}_j) = q(\boldsymbol{s}_i) + (\boldsymbol{s}_j - \boldsymbol{s}_i)\,(\boldsymbol{\nabla} q)_i \;. \tag{124}$$

This is an over-determined problem if the number of neighbouring cells exceeds three, which is the case for most mesh configurations (even in the 2D scenario, cf. Fig. 5). To determine a unique solution, we employ the least squares approach that minimizes the accumulated deviations S_{tot} of the final gradient to all adjacent cells j:

$$S_{\mathrm{tot}} = \sum_j g_j \left((q_j - q_i) - (\boldsymbol{\nabla} q)_i\,(\boldsymbol{s}_j - \boldsymbol{s}_i)\right)^2 . \tag{125}$$

Here, $g_j = A_{ij}/(\boldsymbol{s}_j - \boldsymbol{s}_i)^2$ denotes a relative weight for cell j which emphasizes neighbouring cells that share a large common interface or whose COMs have a small distances between them. We use the resulting gradient $(\boldsymbol{\nabla} q)_i$ to perform the spatial extrapolation of q from the cell's COM $\boldsymbol{s}_i$ to the geometric centre $\boldsymbol{f}_{ij}$ of the respective interface:

$$(q)_{\boldsymbol{f}} = q + (\boldsymbol{f}_{ij} - \boldsymbol{s}_i)\,(\boldsymbol{\nabla} q)_i \,. \tag{126}$$

3.3.4 Time integration

Arepo employs a second-order accurate scheme to update the physical values inside a cell at each time step. This method relies on a procedure similar to Heun's method and was introduced by Pakmor et al. (2016b). We explain the individual steps of this numerical procedure below.

First, we calculate the primitive variables from the conserved variables at the beginning of the current time step to obtain $\boldsymbol{W}_i^n$ at the centre of cell i. We then

reconstruct the gradient of each quantity $q \in \boldsymbol{W}_i^n$ and extrapolate the central value to the interface of cells i and j (I_{ij} in the following) as described in Sec. 3.3.3:

$$\boldsymbol{W}_{ij}^n = \boldsymbol{W}_i^n + (\boldsymbol{f}_{ij} - \boldsymbol{s}_i)(\boldsymbol{\nabla W})_i \,. \tag{127}$$

We pass the resulting values of $\boldsymbol{W}_{ij}^n$ to the HLLD Riemann solver, obtain the fluxes $\hat{\boldsymbol{F}}_{ij}^n$ through I_{ij} at the current time step, and apply these fluxes for half a time step to cell i. To simplify numerical calculations, the volume-integrated quantities are used instead of the volume-averaged quantities and Gauss's divergence theorem is applied to the flux-divergence term:

$$\frac{\partial}{\partial t}\int_V \boldsymbol{U}\,\mathrm{d}V + \int_V \boldsymbol{\nabla}\cdot\boldsymbol{F}\,\mathrm{d}V = \boldsymbol{0} \quad\Longleftrightarrow\quad \frac{\partial}{\partial t}\boldsymbol{Q} + \int_A \boldsymbol{F}\cdot\boldsymbol{n}\,\mathrm{d}A = \boldsymbol{0}, \tag{128}$$

or as explicit update scheme:

$$\boldsymbol{Q}_i' = \boldsymbol{Q}_i^n - \frac{\Delta t}{2}\sum_j A_{ij}\hat{\boldsymbol{F}}_{ij}^n\left(\boldsymbol{W}_{ij}^n, \boldsymbol{W}_{ji}^n\right) \,. \tag{129}$$

The sum extends over all adjacent cells j, and A_{ij} denotes the oriented area of I_{ij}. Next, Arepo determines the vertex velocities $\boldsymbol{w}$ of the MGPs, moves the MGPs to their new positions according to:

$$\boldsymbol{r}' = \boldsymbol{r}^n + \Delta t\,\boldsymbol{w}^n \,, \tag{130}$$

and constructs the new mesh based on the updated positions $\boldsymbol{r}'$ of the MGPs. The resulting mesh represents the updated spatial discretization of the system at time t^{n+1}. We therefore need to repeat the spatial extrapolation of the primitive variables, complemented by advancing $\boldsymbol{W}$ by a full time step:

$$\boldsymbol{W}_{ij}' = \boldsymbol{W}_i^n + (\boldsymbol{f}_{ij}' - \boldsymbol{s}_i')(\boldsymbol{\nabla W})_i + \Delta t\,\frac{\partial \boldsymbol{W}}{\partial t}, \tag{131}$$

where primed variables are time-extrapolated quantities calculated based on the new mesh at the end of a time step. Instead of determining the time derivative of the primitive variables directly, we use the ideal MHD equations to express the temporal in terms of spatial derivatives. Neglecting source terms, we find (cf. Eqs. (6), (13), (20), and (15)):

$$\frac{\partial \rho}{\partial t} = -\rho\boldsymbol{\nabla}\cdot\boldsymbol{u} - \boldsymbol{u}\cdot\boldsymbol{\nabla}\rho, \tag{132}$$

$$\frac{\partial \boldsymbol{u}}{\partial t} = -\frac{\boldsymbol{\nabla}P}{\rho} - (\boldsymbol{u}\cdot\boldsymbol{\nabla})\boldsymbol{u} + \frac{\boldsymbol{\nabla}\cdot\boldsymbol{B}\boldsymbol{B}}{\rho}, \tag{133}$$

$$\frac{\partial P_{\mathrm{th}}}{\partial t} = -\gamma_{\mathrm{th}}P_{\mathrm{th}}\boldsymbol{\nabla}\cdot\boldsymbol{u} - \boldsymbol{u}\cdot\boldsymbol{\nabla}P_{\mathrm{th}}, \tag{134}$$

$$\frac{\partial \boldsymbol{B}}{\partial t} = -\boldsymbol{\nabla}\cdot(\boldsymbol{B}\boldsymbol{u} + \boldsymbol{u}\boldsymbol{B})\,, \tag{135}$$

where $P = P_{\mathrm{th}} + \boldsymbol{B}^2/2$ is the total MHD pressure. We pass the primitive values of $\boldsymbol{W}_{ij}'$ to the HLLD Riemann solver and obtain the current fluxes $\boldsymbol{F}_{ij}'$ associated with

the new mesh at t^{n+1}. Finally, we apply these fluxes for another one-half time step:

$$\boldsymbol{Q}_i^{n+1} = \boldsymbol{Q}'_i - \frac{\Delta t}{2} \sum_j A_{ij}^{n+1} \hat{\boldsymbol{F}}'_{ij} \left(\boldsymbol{W}'_{ij}, \boldsymbol{W}'_{ji} \right) . \tag{136}$$

Note that the calculation of the intermediate state in Eq. (131) requires the calculation of the fluxes twice and therefore also the solution of the Riemann problem twice. Although this is an undesirable computational overhead, the additional expense is not significant compared to generating the moving mesh in Arepo (Pakmor et al., 2016b), and the benefit of second-order accuracy outweighs this issue.

3.3.5 Evolution of conserved scalar quantities

Arepo provides particular routines for the integration and evolution of conserved scalar quantities s that are passively advected with the mass flow. The evolution equation of such quantities reads as:

$$\frac{\partial}{\partial t} \left(\rho \frac{s}{\rho} \right) + \boldsymbol{\nabla} \cdot \left[\left(\rho \frac{s}{\rho} \right) \boldsymbol{u} \right] = 0. \tag{137}$$

Combining this equation with the continuity equation (6) provides a universal relation between the temporal and spatial derivatives of s:

$$\frac{\partial}{\partial t} \left(\frac{s}{\rho} \right) = -\boldsymbol{u} \cdot \boldsymbol{\nabla} \left(\frac{s}{\rho} \right) , \tag{138}$$

representing the primitive formulation of Eq. (137). We employ Eq. (138) during the temporal extrapolation step described in Sec. 3.3.4.

Passive scalars are integrated using the same finite-volume algorithm as the MHD equations. To calculate the fluxes at cell interfaces, the approximate solution to the Riemann problem provided by the HLLD Riemann solver is extended to incorporate these passive scalars. Because passive scalars are advected with the mass flow, the flux of the passive scalar is calculated by upwinding this quantity at the cell interface using:

$$F_q = F_{\rho,\mathrm{HLLD}} \times \begin{cases} s_\mathrm{L}/\rho_\mathrm{L}, & S_\mathrm{M} > 0 \\ s_\mathrm{R}/\rho_\mathrm{R}, & S_\mathrm{M} < 0 \, , \end{cases} \tag{139}$$

where $F_{\rho,\mathrm{HLLD}}$ is the result of the mass flux $\rho\boldsymbol{u}$ from the HLLD Riemann solver at the same interface. No additional changes to the Riemann solver are needed because passive scalars are assumed to be truly passive and not to influence the dynamics of the MHD fluid. Although this property does not hold for the CRs energy and entropy, experience and the presented numerical test show that this algorithm can be applied to these quantities as well.

3.4 Implementation of CR physics

In this section, we present our implementation of CR physics into the existing MHD framework of Arepo. We first describe the required modifications to the MHD module and how we solve the additional equation for CR energy and entropy, respectively. Subsequently, we explain the algorithm for shock detection and how the CR acceleration process at shocks is realized numerically.

3.4.1 Customizations of the MHD module

The full set of CR-MHD equations can be written in compact form as:

$$\frac{\partial}{\partial t}\boldsymbol{U} + \boldsymbol{\nabla}\cdot\boldsymbol{F} = \boldsymbol{S}. \tag{140}$$

Here, applying the energy-based method, the state vector $\boldsymbol{U}$ contains an additional value describing CR energy density $\varepsilon_{\mathrm{cr}}$, $\boldsymbol{F}$ accounts for the additional flux $\varepsilon_{\mathrm{cr}}\boldsymbol{u}$, and the vector $\boldsymbol{S}$ contains source terms describing explicit gains and losses of CRs $(\Gamma_{\mathrm{cr}}, \Lambda_{\mathrm{cr}})$ and thermal gas $(\Gamma_{\mathrm{th}}, \Lambda_{\mathrm{th}})$ as well as terms accounting for the adiabatic changes of the CR fluid $(P_{\mathrm{cr}}\boldsymbol{\nabla}\cdot\boldsymbol{u})$:

$$\boldsymbol{U} = \begin{pmatrix} \rho \\ \rho\boldsymbol{u} \\ \varepsilon \\ \varepsilon_{\mathrm{cr}} \\ \boldsymbol{B} \end{pmatrix}, \boldsymbol{F} = \begin{pmatrix} \rho\boldsymbol{u} \\ \rho\boldsymbol{u}\boldsymbol{u} + P_{\mathrm{tot}}\mathbf{1} + \boldsymbol{B}\boldsymbol{B} \\ (\varepsilon + P_{\mathrm{tot}})\boldsymbol{u} + \boldsymbol{B}(\boldsymbol{u}\cdot\boldsymbol{B}) \\ \varepsilon_{\mathrm{cr}}\boldsymbol{u} \\ \boldsymbol{B}\boldsymbol{u} + \boldsymbol{u}\boldsymbol{B} \end{pmatrix}, \boldsymbol{S} = \begin{pmatrix} 0 \\ \mathbf{0} \\ P_{\mathrm{cr}}\boldsymbol{\nabla}\cdot\boldsymbol{u} + \Gamma_{\mathrm{th}} + \Lambda_{\mathrm{th}} \\ -P_{\mathrm{cr}}\boldsymbol{\nabla}\cdot\boldsymbol{u} + \Gamma_{\mathrm{cr}} + \Lambda_{\mathrm{cr}} \\ \mathbf{0} \end{pmatrix}. \tag{141}$$

Using the entropy-conserving scheme, the CR energy density equation is replaced by the CR entropy density equation, and explicit CR energy gains and losses are converted to explicit CR entropy gains and losses:

$$\boldsymbol{U} = \begin{pmatrix} \rho \\ \rho\boldsymbol{u} \\ \varepsilon \\ \rho K_{\mathrm{cr}} \\ \boldsymbol{B} \end{pmatrix}, \boldsymbol{F} = \begin{pmatrix} \rho\boldsymbol{u} \\ \rho\boldsymbol{u}\boldsymbol{u} + P_{\mathrm{tot}}\mathbf{1} + \boldsymbol{B}\boldsymbol{B} \\ (\varepsilon + P_{\mathrm{tot}})\boldsymbol{u} + \boldsymbol{B}(\boldsymbol{u}\cdot\boldsymbol{B}) \\ \rho K_{\mathrm{cr}}\boldsymbol{u} \\ \boldsymbol{B}\boldsymbol{u} + \boldsymbol{u}\boldsymbol{B} \end{pmatrix}, \boldsymbol{S} = \begin{pmatrix} 0 \\ \mathbf{0} \\ P_{\mathrm{cr}}\boldsymbol{\nabla}\cdot\boldsymbol{u} + \Gamma_{\mathrm{th}} + \Lambda_{\mathrm{th}} \\ \frac{\gamma_{\mathrm{cr}}-1}{\rho^{\gamma_{\mathrm{cr}}-1}}(\Gamma_{\mathrm{cr}} + \Lambda_{\mathrm{cr}}) \\ \mathbf{0} \end{pmatrix}. \tag{142}$$

In the following, we explain how these additional CR quantities are incorporated into the previously described algorithms.

Evolution of CR energy/entropy Because the evolution equation for CR entropy in Eq. (142) resembles the evolution equation of a scalar quantity when neglecting explicit gains and losses, we use the routines explained in Sec. 3.3.5 to implement the evolution equation of CR entropy. CR energy, however, is not conserved due to the adiabatic compression or expansion of the thermal gas to which the CRs are coupled (Eq. (141)). The corresponding adiabatic source terms extend the otherwise homogeneous CR energy equation. These terms are implemented using the method presented by Pfrommer et al. (2017). Here, they used Gauss' divergence theorem to calculate the change of CR energy due to these sources:

$$\left.\frac{\partial E_{\mathrm{cr}}}{\partial t}\right|_{\mathrm{adiab}} = \int_V P_{\mathrm{cr}}\boldsymbol{\nabla}\cdot\boldsymbol{u}\,\mathrm{d}V \approx \int_V \boldsymbol{\nabla}\cdot(P_{\mathrm{cr}}\boldsymbol{u})\,\mathrm{d}V = \int_A P_{\mathrm{cr}}\boldsymbol{u}\cdot\boldsymbol{n}\,\mathrm{d}A, \tag{143}$$

where $E_{\mathrm{cr}} = \int_V \varepsilon_{\mathrm{cr}}\mathrm{d}V$ and the approximation in the second step assumes a constant CR pressure ($\boldsymbol{\nabla}P_{\mathrm{cr}} = \mathbf{0}$) across the cell. The occurring surface integral can be converted into a discrete sum over all cell interfaces of a given VC. The pressure and the normal velocity in the surface integral need to be evaluated in order to calculate the integral. To this end, we use the normal velocity as calculated by

the HLLD Riemann solver and choose the cell-centred value of $P_{\rm cr}$. Although this choice may appear arbitrary, this results in a stable integration scheme, which we will demonstrate using our test problems. The adiabatic source term appears in the energy equation with the opposite sign, which states that adiabatic processes conserve the total energy in the system. To account for this on a numerical level, the same amount of energy calculated by the surface integral is added to the thermal energy of a cell, but with the opposite sign.

We account for non-adiabatic source terms of CR energy in an operator-split fashion after evolving the implicit CR-MHD system by a full time step. In the process, we first apply gains of CR energy due to CR injection in SNe remnants ($\Gamma_{\rm cr}$, cf. Eq. (95)) and CR acceleration at resolved shocks (see Sec. 3.4.2), followed by CR cooling due to Coulomb and hadronic interactions ($\Lambda_{\rm cr}$, cf. Eq. (94)). This general procedure is used for the energy-based and entropy-conserving schemes. While the default implementation of these source terms in Arepo is based on the energy formulation, all occurring numerical terms in the code are translated to use the CR entropy as the defining CR quantity once the code is set up for simulation with the entropy-conserving scheme.

CR pressure We account for the additional pressure exerted by the CRs adding this pressure onto the thermal pressure during the time extrapolation step of the MHD equations in each cell. Furthermore, the CR pressure is an additional primitive variable inside the hyperbolic equation system. We calculate its value from CR energy density ($P_{\rm cr} = (\gamma_{\rm cr} - 1)\varepsilon_{\rm cr}$) or CR entropy density ($P_{\rm cr} = \rho K_{\rm cr}\, \rho^{\gamma_{\rm cr}-1}$), depending on the scheme in use. The CR pressure, as a primitive variable, is used by the Riemann solver to calculate fluxes. As other MHD quantities sharing the same property, this quantity is extrapolated in space and time during the finite volume step of Arepo. We extrapolate the CR pressure from the COM $\boldsymbol{s}_i$ of cell i to the geometric centre $\boldsymbol{f}_{ij}$ of an interface according to Eqs. (127) and (131), replacing the time derivative of the CR pressure using:

$$\frac{\partial P_{\rm cr}}{\partial t} = -P_{\rm cr}(\boldsymbol{\nabla}\cdot\boldsymbol{u})_i - \boldsymbol{u}\cdot(\boldsymbol{\nabla}P_{\rm cr})_i\,. \tag{144}$$

We obtain this relation combining the CR energy equation (83) with the EOS (84) of CRs and neglecting source terms. In Sec. 3.3.3, we describe how we estimate the velocity divergence, and we employ the same method to find a suitable estimate for the CR pressure gradient.

Modifications to the HLLD solver The HLLD Riemann solver is designed to solve the ideal MHD equations and is not intended to consider an additional CR fluid. In order not to change its original scope, we account separately for the evolution of the CR variables and the source terms that arise in the process. However, CRs affect the total pressure of the system, and the effective adiabatic index of a two-component fluid differs from that of an ideal thermal gas:

$$\gamma_{\rm eff} = \left(\gamma_{\rm th}P_{\rm th} + \gamma_{\rm cr}P_{\rm cr}\right)/(P_{\rm th} + P_{\rm cr}). \tag{145}$$

Consequently, we modify the speed of the slow and fast magneto-acoustic waves as follows (Pfrommer et al., 2017):

$$c_{\,\mathrm{fa,sl}} = \left[\frac{\gamma_{\mathrm{eff}} P_{\mathrm{t}} + B^2 \pm \sqrt{\left(\gamma_{\mathrm{eff}} P_{\mathrm{t}} + B^2\right)^2 - 4\gamma_{\mathrm{eff}} P_{\mathrm{t}} B_x^2}}{2\rho}\right]^{1/2}, \tag{146}$$

where $P_{\mathrm{t}} = P_{\mathrm{th}} + P_{\mathrm{cr}}$ is the total pressure of the CRs and the thermal fluid. This total pressure is also used as a replacement for the thermal pressure whenever its quantity is used inside the Riemann solver when the origin of the corresponding terms is the pressure term of the momentum equation. These modifications are independent of whether we use the CR energy or entropy scheme. Note that the Alfvén waves generally remain unaffected by the additional CR pressure.

3.4.2 CR acceleration at resolved shocks

Shock detection To model the injection of freshly accelerated CRs at shock fronts, we employ the shock finding method developed by Schaal and Springel (2015) and extended by Pfrommer et al. (2017). We summarize the main points of this algorithm for completeness here. The shock finding algorithm identifies a shock zone by applying the following local cell-based criteria:

(i) $\nabla \cdot \boldsymbol{u} < 0$,

(ii) $\nabla \tilde{T} \cdot \nabla \rho > 0$,

(iii) $\tilde{\mathcal{M}} > \tilde{\mathcal{M}}_{\mathrm{min}}$,

where $\tilde{\mathcal{M}}$ is the (numerically stabilized) shock Mach number, and $\tilde{T}$ is the pseudo temperature of the composite gas, defined via:

$$k_{\mathrm{B}} \tilde{T} = \frac{P}{n} = \frac{\mu m_{\mathrm{p}} (P_{\mathrm{th}} + P_{\mathrm{cr}})}{\rho}, \tag{147}$$

where n is the gas number density, m_{p} is the proton rest mass, and μ denotes the mean molecular weight. Criterion (i) identifies converging flows, which is the essential condition for the presence of a shock. To filter spurious shocks such as tangential or contact discontinuities, criterion (ii) is applied. These discontinuities are characterized by having a constant pressure across their surfaces, implying that the temperature and density change in opposite directions and therefore the corresponding gradients have opposite signs. Criterion (iii) gives a minimum threshold for the Mach number to distinguish numerical noise from physical shocks, which we choose to be $\tilde{\mathcal{M}}_{\mathrm{min}} = 1.3$ in this work (Pfrommer et al., 2017).

Modelling CR acceleration Kinetic gas energy is dissipated into thermal and non-thermal energy at a shock. For a composite fluid of thermal gas and CRs, the dissipated energy at the shock is given by the difference between the total post-shock energy (index '2') and the adiabatically compressed pre-shock energy (index '1') (Pfrommer et al., 2017):

$$\varepsilon_{\mathrm{diss}} = \varepsilon_{\mathrm{th},2} + \varepsilon_{\mathrm{cr},2} - \left(\varepsilon_{\mathrm{th},1}\, x_{\mathrm{s}}^{\gamma_{\mathrm{th}}} + \varepsilon_{\mathrm{cr},1}\, x_{\mathrm{s}}^{\gamma_{\mathrm{cr}}}\right), \tag{148}$$

where $x_\mathrm{s} = \rho_2/\rho_1$ is the shock compression ratio. The dissipated energy is advected with the post-shock velocity u_2, resulting in a flux:

$$f_\mathrm{diss} = \varepsilon_\mathrm{diss} u_2 = \varepsilon_\mathrm{diss} \frac{\mathcal{M}_1 c_1}{x_\mathrm{s}}, \tag{149}$$

with $\mathcal{M}_1$ the pre-shock Mach number and c_1 the pre-shock sound speed. We thus obtain the rate of energy dissipation at a shock with surface A_s by:

$$\frac{\mathrm{d}E_\mathrm{diss}}{\mathrm{d}t} = f_\mathrm{diss} A_\mathrm{s}. \tag{150}$$

Diffusive shock acceleration and other plasma-physical processes can convert a fraction of the dissipated energy into energy contained in CRs, which we model by the factor ζ_cr:

$$\Delta E_\mathrm{cr} = \zeta_\mathrm{cr} \frac{\mathrm{d}E_\mathrm{diss}}{\mathrm{d}t} \Delta t = \zeta_\mathrm{cr} E_\mathrm{diss}\,. \tag{151}$$

Generally, ζ_cr may depend on Mach number $\mathcal{M}_1$, magnetic obliquity θ, i.e. the angle between shock normal and the magnetic field, and the plasma beta parameter $\beta = P_\mathrm{th}/P_\mathrm{mag}$ (Pfrommer et al., 2017). In this work, however, we follow the results reported by Caprioli and Spitkovsky (2014) for quasi-parallel shocks ($\theta \lesssim 45°$) with $\mathcal{M}_1 > 3$ and choose $\zeta_\mathrm{cr} = 0.1$.

We model the conversion of dissipated energy to CR energy for each cell that is part of the shock with the following procedure. First, we compute the total dissipated energy as the energy difference between shocked and pre-shock region:

$$\Delta E_\mathrm{tot} = \sum_j \left[(E_\mathrm{tot})_j - E_\mathrm{tot,1}\right], \tag{152}$$

where the sum extends over all cells j the shock finder recognizes as involved in the shock, i.e. the shock surface and the post-shock zone. We then distribute the total dissipated energy among the detected cells according to their relative contribution to that energy:

$$(\Delta E_\mathrm{cr})_i = \zeta_\mathrm{cr} E_\mathrm{diss} \frac{(E_\mathrm{tot})_i - E_\mathrm{tot,1}}{E_\mathrm{tot}}\,. \tag{153}$$

This existing injection algorithm is extended to be applicable with the CR entropy formalism. We first calculate the pre-existing CR energy from the current value of the CR entropy, add the injected CR energy, and then recalculate the CR entropy from the updated value of the CR energy. This ensures energy conservation of dissipated energy during the injection procedure.

We execute the shock finder at the end of each hydro-step and apply the resulting source term of CR energy or entropy for a full time step. It should be noted that we neglect the effect of adiabatic compression of the thermal gas and CRs when calculating the total dissipated energy in Eq. (152). Pfrommer et al. (2017) argue that this contribution is negligible for strong shocks and the presented algorithm proves to be stable in many applications.

4 Numerical tests

In this section, we perform a suite of test problems to compare the performance of the energy-based and entropy-conserving methods described in Sec. 2.4. By default, all simulations in this section are performed with the moving-mesh setup of Arepo using standard parameters for mesh regularization (Vogelsberger et al., 2012; Pakmor et al., 2016b; Weinberger et al., 2020) and a grid that is initially equally spaced.

4.1 Pressure balance

In this first test, we set up a contact discontinuity characterized by a uniform density, a uniform total pressure but jumping CR and thermal pressures over the discontinuity. The gas is initially moving with a constant velocity inside a periodic simulation domain. Because the total pressure is constant, these initial conditions are dynamically stable in the sense that the CR and thermal pressure jumps at the contact discontinuity should not introduce any additional motions. The resulting profiles for the gas density, velocity, thermal, and CR pressure should coincide with their respective initial values after each periodic crossing of the contact discontinuity through the simulation domain. This pressure balance test offers a simple way to test the basic stability of a numerical method in hydrodynamics. If a method fails this test, it is likely to fail even in more complex simulations. We use the same setup of Gupta et al. (2021). The contact discontinuity is set up at $x = 0.5$ inside a periodic simulation domain of length $L = 1$. The initial conditions for the left and the right state are defined as $\{\rho, u, P_{\rm th}, P_{\rm cr}\}_L = \{1, 1, 0.1, 0.9\}$ and $\{\rho, u, P_{\rm th}, P_{\rm cr}\}_R = \{1, 1, 0.9, 0.1\}$. We use a resolution of $N = 1000$ mesh cells and the moving-mesh setup of Arepo.

Figure 7 shows the simulation results of the pressure balance test at $t = 1$, i.e. after one box-crossing time. Note that the limits of the respective y-axis in the top row are set to $\Delta y \lesssim 5 \times 10^{-12}$. Minor blips form in the density, velocity, and pressure profiles using either CR formulation. Because the blips have a low amplitude, they do not influence the overall dynamics. Gupta et al. (2021) performed the same test, employing both the energy and entropy formalism for CR transport in the PLUTO code. They found that their numerical scheme produces deviations in the percentage regime for the simulation with the entropy formalism, and that truncation errors in simulations with the energy formalism depended on details of the numerical algorithm they chose.

4.2 1D shock tubes

For our next test, we perform a sequence of one-dimensional (1D) shock-tube simulations with various Mach numbers $\mathcal{M} = u_{\rm sh}/c_{\rm s,\,pre}$, where $u_{\rm sh}$ is the shock velocity in the lab frame and $c_{\rm s,\,pre}$ is the pre-shock sound speed. We vary $\mathcal{M}$ from 1.5 to 100 and use several resolutions ranging from $N = 30$ to 10^4 mesh cells. The general setup to this problem is identical to the one presented by Pfrommer et al. (2017). We set up a box of length $L = 10$ containing a discontinuity at $x = 5$. Gas in the left half-space ($x < 5$) has a density of $\rho = 1$ and a relative CR pressure of $X_{\rm cr} = P_{\rm cr}/P_{\rm th} = 2$. We vary the thermal pressure and the CR pressure between dif-

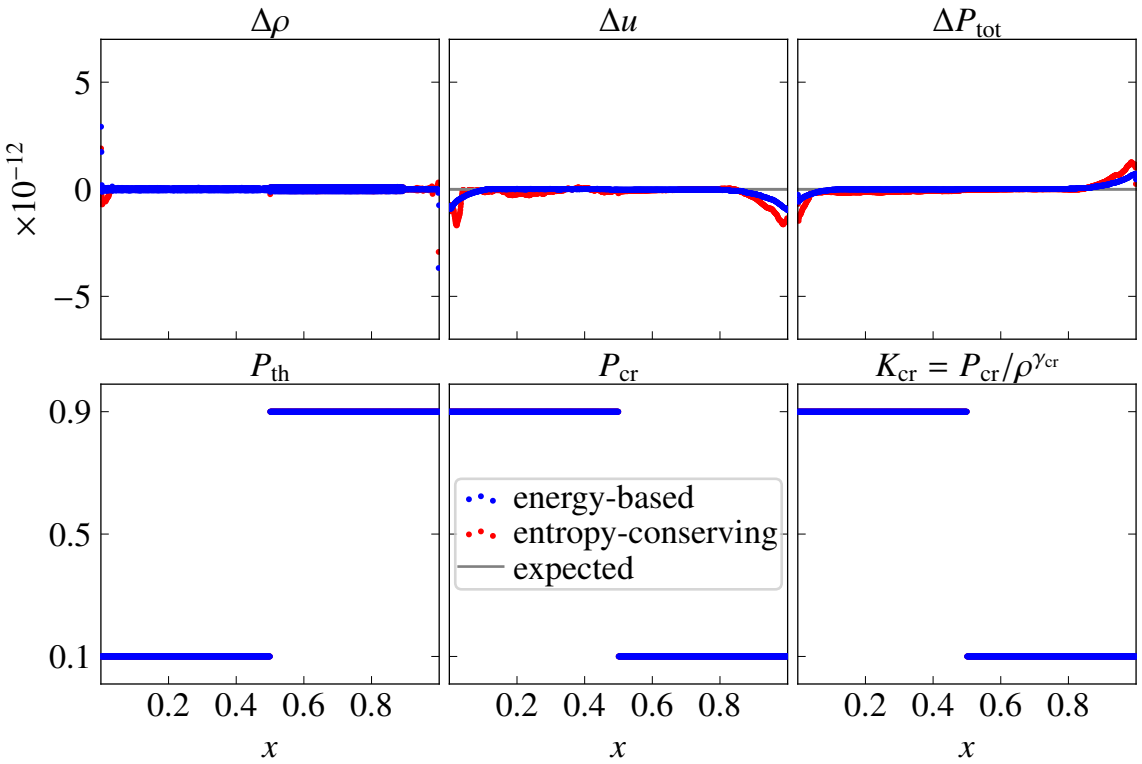

Figure 7: Results of the pressure balance test with periodic boundary conditions at $t = 1.0$, i.e. after one box crossing time. In the top row, we plot the deviations of the simulation results from the expected values, i.e. $\Delta\rho$, Δu_x and $\Delta P_{\rm tot}$. Note that the limits of the respective y-axis are set to $\Delta y \lesssim 5 \times 10^{-12}$ (where $y \in \{\rho, u, P_{\rm tot}\}$). The bottom row shows quantities that are initially discontinuous across $x = 0.5$, i.e. $P_{\rm th}$, $P_{\rm cr}$, and $K_{\rm cr}$.

ferent simulations in this region to achieve the desired Mach numbers of the shock while keeping the pressure ratio $X_{\rm cr}$ constant. A shock tube forms because this half-space is initially over-pressurised with respect to the right half-space ($x > 5$) that contains gas at a low density of $\rho = 0.125$. The thermal and CR pressures in this region are the same for all simulations and are set to $P_{\rm th} = P_{\rm cr} = 0.05$. The fluid is initially at rest, $u_x = 0$, and we use reflective boundary conditions. We refer to Table 1 for the exact initial values. We perform two sets of simulations: one that only considers adiabatic changes of CRs (discussed in Sec. 4.2.1) and one that additionally accounts for non-adiabatic changes in the form of CR acceleration at the shock (discussed in Sec. 4.2.2).

4.2.1 Adiabatic CRs

Figure 8 shows the results of the 1D shock-tube test with $\mathcal{M} = 10$ and only accounting for adiabatic changes of the CRs. The left-hand panel shows the results using the energy-based method, the right-hand panel shows the outcome using the entropy-conserving scheme. We perform both runs with identical initial conditions (see Table 1) and a spatial resolution of $N = 100$ mesh cells. The simulation results resemble the well-known Sod-shock tube: a rarefaction develops to the left, while a contact discontinuity and a shock form to the right of the initial discontinuity. Because the CRs evolve only adiabatically, the CR entropy is expected to be almost

Table 1: Initial conditions for the shock-tube tests with various Mach numbers $\mathcal{M}$. The indices L and R denote values of the left and right half-space, respectively.

$\mathcal{M}$	u_x	ρ_L	$P_\mathrm{th,\,L}$	$X_\mathrm{cr,\,L}$	ρ_R	$P_\mathrm{th,\,R}$	$X_\mathrm{cr,\,R}$
Without CR shock acceleration:							
1.5	0	1	0.24263	2	0.125	0.05	1
2	0	1	0.54795	2	0.125	0.05	1
3	0	1	1.4182	2	0.125	0.05	1
5	0	1	4.1911	2	0.125	0.05	1
10	0	1	17.172	2	0.125	0.05	1
15	0	1	38.804	2	0.125	0.05	1
30	0	1	155.61	2	0.125	0.05	1
60	0	1	622.84	2	0.125	0.05	1
100	0	1	1730.4	2	0.125	0.05	1
With CR shock acceleration:							
9.56	0	1	17.172	2	0.125	0.05	1

featureless. The only discontinuity in this profile should coincide with the contact discontinuity and separate the high CR-entropy gas from the low CR-entropy gas.

As shown in Fig. 8, both methods yield nearly identical results and are in very good agreement with the analytic solutions (solid lines in semi-transparent colour; values adopted from Pfrommer et al. 2006) for density ρ, thermal pressure P_th, CR pressure P_cr, velocity u_x, and CR and thermal entropy, K_cr and $K_\mathrm{th} = P_\mathrm{th}/\rho^{\gamma_\mathrm{th}}$, where $\gamma_\mathrm{th} = 5/3$. To give a more detailed view, we zoom into the post-shock regime of the pressure and entropy plots, as indicated by the inset panels in the second and bottom row. The magnified boxes show the post-shock region around at the analytical solution. We note that even at this magnification P_th and P_cr are still in good agreement with the analytical solution and deviate only about 1 per cent for both numerical schemes. A similar result is obtained for entropy K. The entropy-conserving scheme does an excellent job of adiabatically compressing the CRs at the shock while keeping the CR entropy density constant across the shock. The energy-based method generates an artificial amount of CR entropy at the shock with a deviation from the analytic solution in the 2 per cent regime using our moving-mesh setup.

We analyse how this spurious entropy generation at the shock depends on the mesh resolution. To this end, we perform a sequence of test runs varying the number of mesh cells in the range of $N = 30$ to 10^4 while keeping the Mach number constant at $\mathcal{M} = 10$. We run each simulation with both a moving mesh and a fixed mesh to compare the two approaches. In order to quantify the deviation from the analytic solution, we evaluate the post-shock regime and determine the median of the absolute difference between the numerical and analytic solution within that region. We choose to calculate the median difference because the large entropy jump between the contact discontinuity and post-shock region would lead to misleading results when calculating the *mean* deviation in low-resolution simulations.

In Fig. 9, we show the median differences of the thermal and CR pressures and entropy densities for varying resolutions from $N = 30$ to 10^4 on the LHS and display

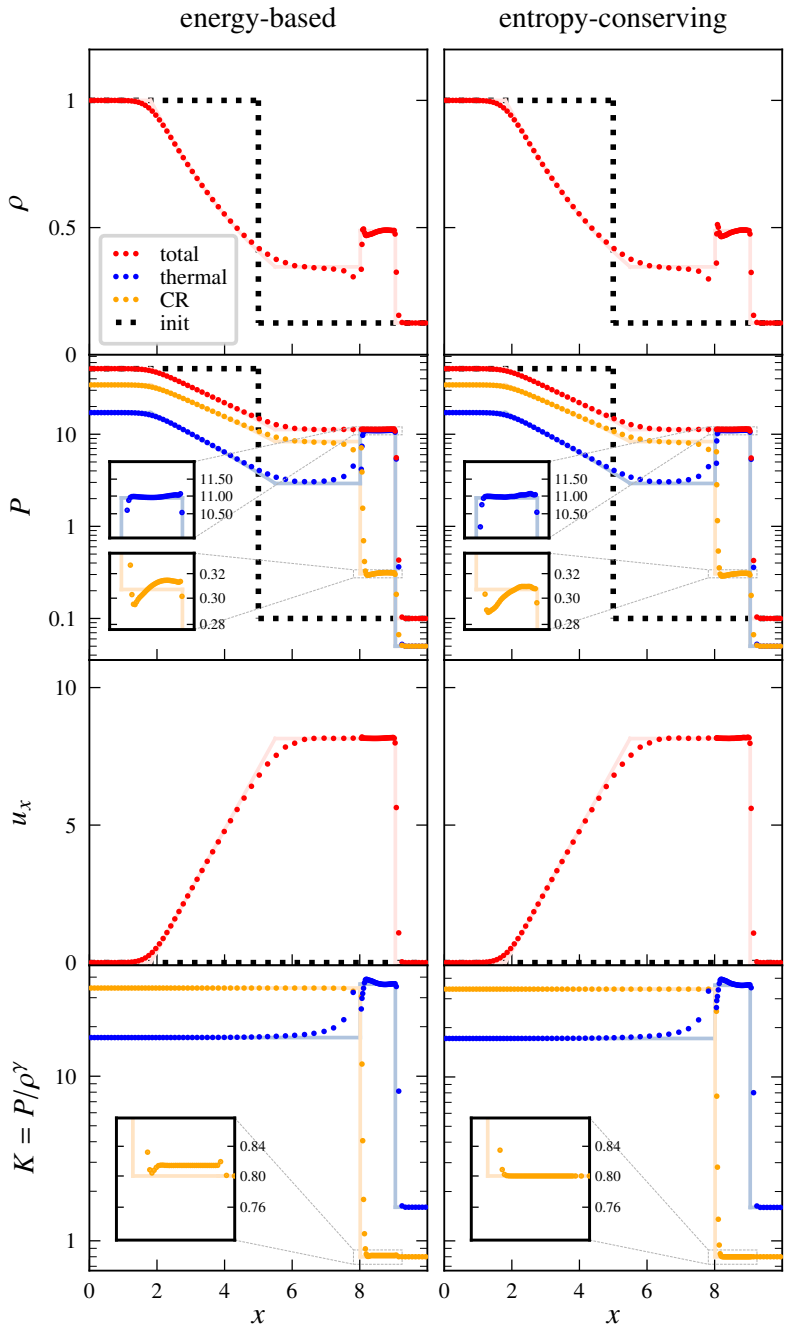

Figure 8: Shock-tube test for a composite of CRs and thermal gas while omitting CR acceleration at the shock. The left column displays the results using the energy-based method and the right column those of the entropy-conserving scheme. Shown are 1D simulations with a resolution of $N = 100$ mesh cells and $\mathcal{M} = 10$ at $t = 0.37$. We plot from top to bottom: mass density ρ, pressure P, velocity u_x and entropy P_i/ρ^{γ_i}, where $i \in \{\mathrm{cr}, \mathrm{th}\}$. Analytic solutions are shown as solid lines in semi-transparent colours and simulation results as dots. The inset panels in the second and bottom row show magnifications of the corresponding post-shock regime, indicated by the dashed rectangles.

the pressure and entropy density profiles near the shock for $N = 100$ on the RHS. Results obtained with the moving-mesh method are grouped together in the top row, while the result obtained with the static-mesh method can be found in the bottom row.

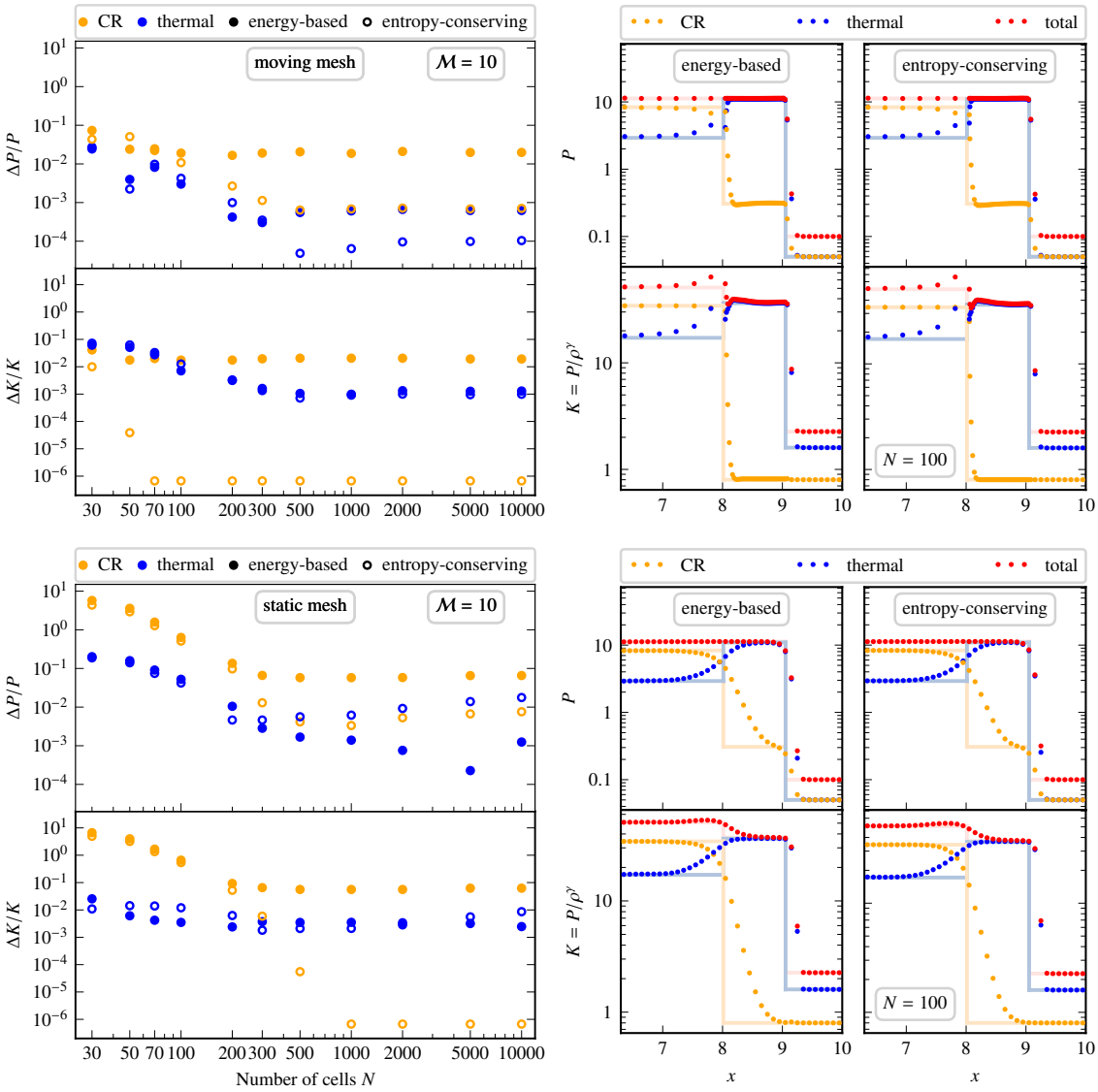

Figure 9: Shock-tube test with $\mathcal{M} = 10$ and various resolutions ranging from $N = 30$ to 10^4 mesh cells *without* accounting for CR acceleration at the shock. The top row displays the results of the moving-mesh approach, the bottom row shows the results using a static-mesh setup. In the left-hand panels, we plot the median of the absolute deviations in the post-shock region from the analytic solution of $P_{\rm th}$, $P_{\rm cr}$, $K_{\rm th}$, and $K_{\rm cr}$ at $t = 0.37$. Filled circles indicate the results using the energy-based method, open circles indicate results of the entropy-conserving scheme. In each panel, we plot the relative error of P in the top row, the relative error of K in the bottom row. For a resolution of $N = 100$ mesh cells, the corresponding post-shock region is depicted in the panels on the RHS, wherein the left column shows the results for the energy-based method and the right column for the entropy-conserving scheme. The static-mesh method yields significantly worse results due to its inherently higher numerical diffusivity.

In the static-mesh setup, the error in $K_{\rm cr}$ diverges towards lower mesh resolutions for both the entropy- and energy-conserving numerical schemes, which can be attributed to the higher numerical diffusivity of this approach. Only for a resolution of $N = 200$ cells, the deviations start to fall below 10 per cent and stabilizes towards higher resolutions or nearly vanishes for the entropy-conserving scheme. The behaviour of $P_{\rm cr}$ is similar: while the error diverges in the poorly resolved runs for both methods, it stabilizes at around 7 per cent for the energy-based method and in

the 1 per cent regime for the entropy-conserving scheme. The deviation of the thermal pressure $P_{\rm th}$ is moderate for low resolutions and converges for higher resolutions to around 2 per cent for the entropy-conserving scheme and to negligible values for the energy-based method.

The moving-mesh approach consistently gives significantly better results. Even for very low resolutions, the deviation of $K_{\rm cr}$ and $P_{\rm cr}$ is clearly below 10 per cent for both energy- and entropy-conserving methods. In the high-resolution runs, these errors converge to around 2 per cent using the energy-based method and nearly vanish when we apply the entropy-conserving scheme. The error in $K_{\rm th}$ behaves nearly identical for both numerical schemes, with values around 8 per cent for very low resolutions and negligible deviations for the high resolution runs. We find similar trends for $P_{\rm th}$ but notice deviations in the 2 per cent regime for the lowest resolutions and negligible errors for an increasing number of mesh cells.

We continue by investigating the dependency of spurious entropy generation at shocks on the Mach number $\mathcal{M}$. Again, we perform a suite of shock-tube simulations but fix the resolution at $N = 100$ mesh cells and vary the Mach number in the range of $\mathcal{M} = 1.5$ to 100 this time. Shocks with lower Mach numbers require more time to fully develop. Hence, in each simulation, we evaluate the post-shock region once the shock has crossed $x = 9$, which corresponds to the theoretical shock position at $t = 0.37$ for $\mathcal{M} = 10$ employed in the previous setup. Since we have already demonstrated that the moving-mesh setup gives much better results, we stick to this approach in the following.

Figure 10 shows the results of the different runs. Again, the entropy-conserving scheme performs very good in adiabatically compressing the CRs at the shock with almost vanishing deviation in $K_{\rm cr}$, independent of Mach number. The relative errors in $P_{\rm th}$ and $P_{\rm cr}$ slightly vary in the regime of 1 per cent and remain small for higher Mach numbers. The energy-based method shows very similar results, except for the deviation of $K_{\rm cr}$, which slightly increases up to a Mach number of 10 and stabilizes at very small values of about 2 per cent for larger $\mathcal{M}$. Overall, both methods give very good results and do not show a severe dependence on Mach number. Semenov et al. (2021) also performed the same test employing both the energy and entropy formalism for CR transport with the ART code. Using their implementation for the energy-based formulation of CR transport, they find a strong dependence of the CR entropy error on the Mach number, with errors reaching $\lesssim 20$ per cent for $\mathcal{M} \geq 9$.

4.2.2 CR acceleration at the shock

Figure 11 shows the results of the 1D shock-tube test with $\mathcal{M} = 9.56$ including CR acceleration at the shock. The left-hand panel displays the results that we obtained with the energy-based method, and the right-hand panel shows the results using the entropy-conserving scheme. Again, we perform each run with identical initial conditions (cf. Table 1) and a spatial resolution of $N = 100$ mesh cells.

The results obtained with energy-based method agree with the exact solution up to minor deviations. The most pronounced differences are the relatively high blips in density, pressure, and entropy in the first two cells past the contact discontinuity. This comes about because in the first few time steps after the start of the simulation, when the shock has not yet fully developed and the post-shock regime is about to

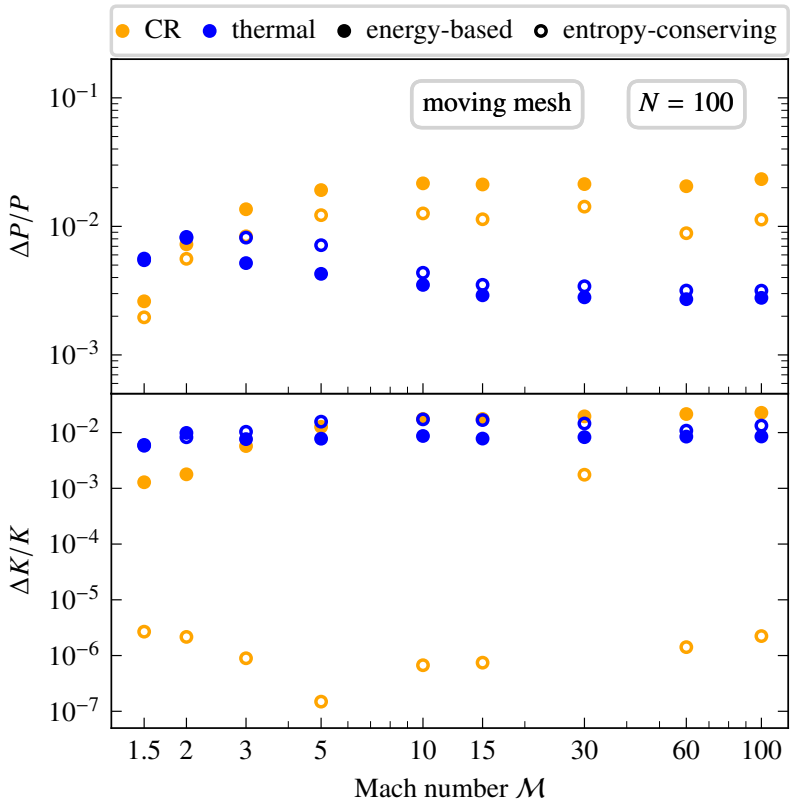

Figure 10: Shock-tube test with $N = 100$ mesh cells and various Mach numbers ranging from $\mathcal{M} = 1.5$ to 100. We use our moving-mesh setup *without* accounting for CR acceleration. We plot the median of the absolute deviations of $P_{\rm th}$, $K_{\rm th}$, and $K_{\rm cr}$ from the analytic solution in the post-shock regime. In each case, we evaluate the post-shock region once the shock has (theoretically) crossed $x = 9$. Filled circles indicate the results of the energy-based method, open circles those of the entropy-conserving scheme. Shown are the relative error in P in the top row and the relative error in K in the bottom row.

form, our algorithm injects too much CR energy because the estimated pressure jump is initially too large. While this causes an increased compressibility in comparison to the exact solution, the algorithm recovers as soon as the shock and post-shock regime have formed and then performs correctly. This behaviour was already mentioned by Pfrommer et al. (2017). Zooming into the post-shock regime, we find that $K_{\rm cr}$ and $P_{\rm cr}$ are subject to a ~ 6 per cent error, while $P_{\rm th}$ deviates by 3 per cent.

The entropy scheme, however, performs worse in this setup. Again, we notice the blips in density and entropy, but in the opposite direction. Unlike the energy-based method, these blips do not settle down when the post-shock zone has developed, but form oscillations with fairly large amplitudes that pervade half of the post-shock region. This is because CR entropy is injected at the shock and therefore CRs are not adiabatically compressed, making entropy conservation no longer valid and the algorithm has problems to adjust to the sudden change of the initially conserved quantity. Most importantly, the shock propagates too fast in comparison to the analytical solution in the entropy-based scheme. This is a consequence of mass conservation: because the density is too low in the left-hand part of the post-shock zone, the total post-shock zone needs to be broader and the shock advances faster.

To quantify this behaviour, we evaluate the ratio of the simulated-to-theoretical

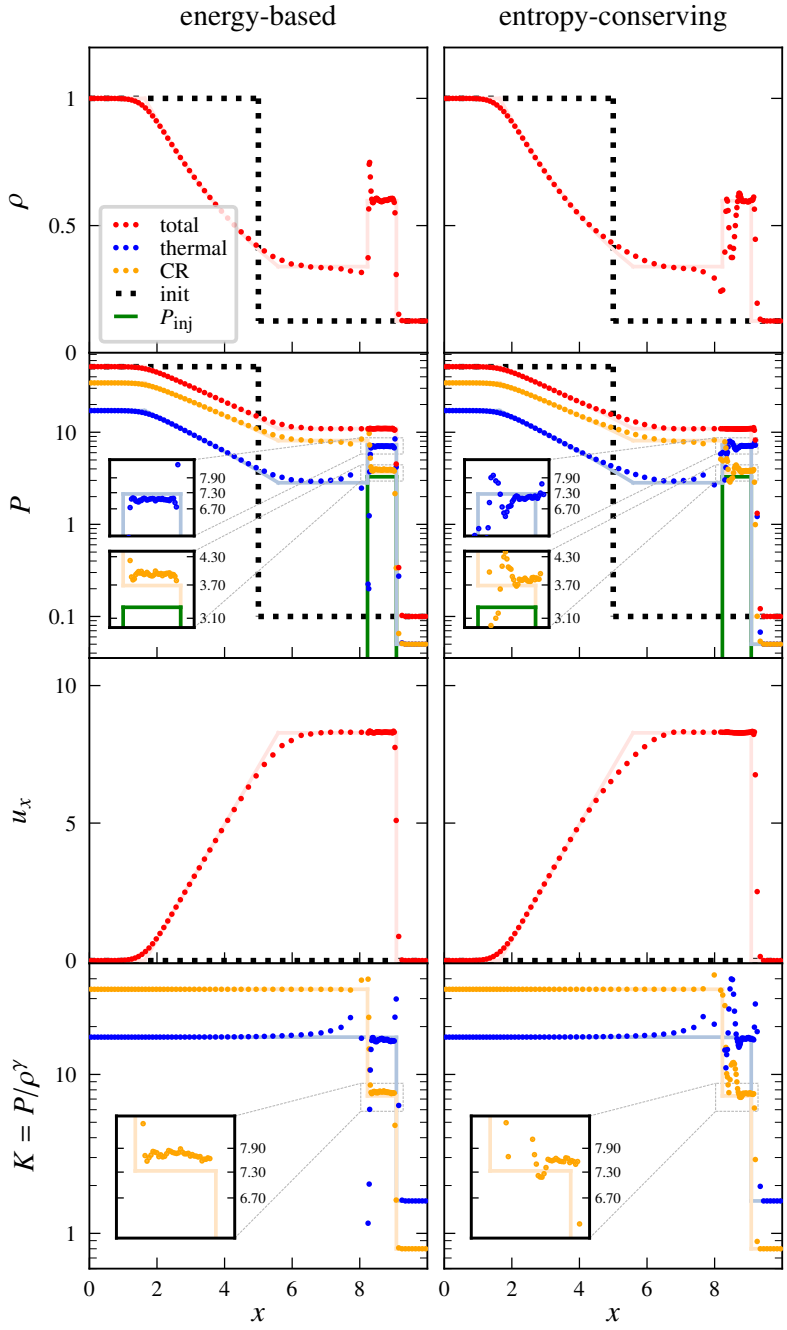

Figure 11: Same setup as in Fig. 8, but now taking into account CR acceleration at the shock with $N = 100$, $\mathcal{M} = 9.56$ and the snapshot taken at $t = 0.39$.

shock velocity $\chi = u_{\rm sh,\,sim}/u_{\rm sh,\,theo}$ by averaging 10 snapshots in the period from $t = 0.31$ to $t = 0.4$. In Fig. 12, we plot the result as a function of resolution. Here, we use the moving-mesh setup, a fixed Mach number of $\mathcal{M} = 9.56$, and we vary the resolution in the range of $N = 30$ to 10^4. The energy-based method simulates the shock position very accurately even for the lowest-resolution run, amounting to a deviation from the theoretical value of $\lesssim 3$ per cent. The error quickly reaches negligible values for higher resolutions. Using the entropy-conserving scheme, the simulated shock position is significantly less accurate in comparison to the energy method, particularly for low resolutions, where the deviation is $\gtrsim 10$ per cent, more

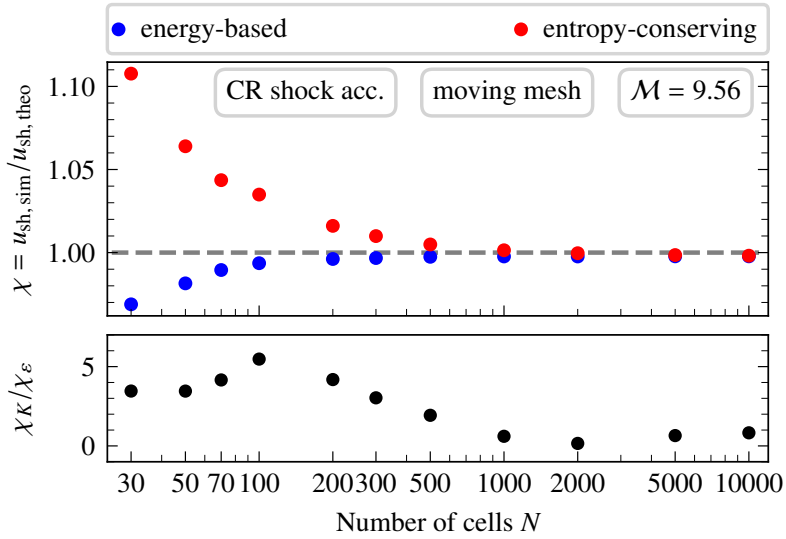

Figure 12: Ratio of simulated-to-theoretical shock velocity $\chi = u_{\rm sh,\,sim}/u_{\rm sh,\,theo}$ (top panel) and the χ-ratio of both numerical schemes (bottom panel) as a function of resolution N, respectively. We use the moving-mesh setup of Arepo with a fixed Mach number of $\mathcal{M} = 9.56$ and account for CR acceleration at the shock. Results obtained with the energy-based method (index ε) are coloured blue, those obtained with the entropy-conserving scheme (index K) red.

than four times worse in comparison to the energy-based method. Only for a resolution of $N \gtrsim 500$, the entropy scheme approaches the accuracy of the energy-based method and the oscillations described earlier also vanish.

We investigate the dependence of the error on the number of mesh cells N for our current setup that includes CR acceleration. Therefore, we fix the Mach number at $\mathcal{M} = 9.56$ and vary the resolution in the range of $N = 30$ to 10^4. Figure 13 shows the results of our test runs. As expected, the inclusion of CR acceleration worsens the numerical solution so that truncation errors at high resolution amount to about 6 per cent for $P_{\rm cr}$ and 4 per cent for $K_{\rm cr}$ (energy-based method) and approximately half of that for the entropy-conserving scheme. At low resolution, the errors increase to values exceeding 10 per cent, with the errors in the entropy-conserving scheme to rise above those in the energy-based method. Note that we identify the error with the median of the absolute deviation between simulation and theory so that the error is not sensitive to (even significant) post-shock oscillations as long as they do not accumulate to more than half of the mesh cells within the post-shock region. Because the oscillations are confined to only a few cells, the median error is hence only slightly affected by this feature, while we identified it to have a significant impact on the shock propagation at resolutions $N \lesssim 500$ (see Fig. 12).

4.3 3D shock tubes

The 1D shock-tube test, described in Sec. 4.2, is a useful tool for evaluating the general performance of a numerical method in an idealized environment. Here, we analyse the differences of the energy-based method and the entropy-conserving scheme in the more challenging 3D shock-tube setup. To address this, we set up a box of size $(L_x, L_y, L_z) = (10, 1, 1)$ and use an irregular glass-like distribution of the particles as initial conditions (see Schaal and Springel, 2015, for details). Like in the

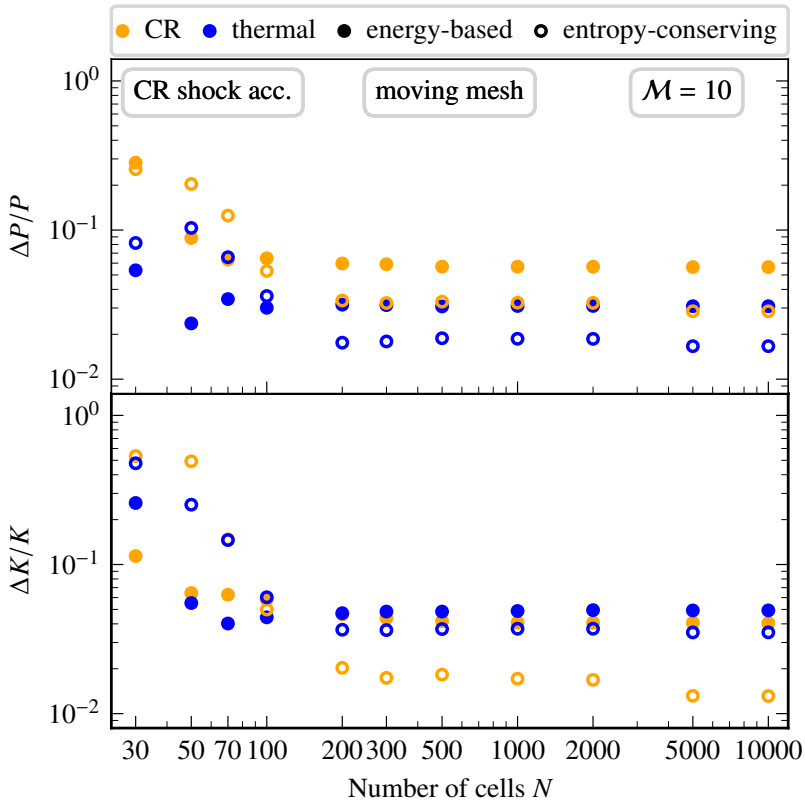

Figure 13: Shock-tube test with Mach number $\mathcal{M} = 9.56$ and various resolutions ranging from $N = 30$ to 10^4. We use our moving-mesh setup and account for CR acceleration at shocks. We plot the median of the absolute deviations of $P_{\rm th}$, $P_{\rm cr}$, $K_{\rm th}$ and $K_{\rm cr}$ from the analytic solution in the post-shock regime at $t = 0.39$. Filled circles indicate the results of the energy-based method, open circles those of the entropy-conserving scheme. We show the relative error of P in the top row and the relative error of K in the bottom row.

1D case, we fix the Mach number at $\mathcal{M} = 10$ and omit CR acceleration at the shock. We vary the number of mesh cells along the x axis in $N_x = \{30, 50, 70, 100, 200\}$ and choose the number of mesh-generating points in the y and z direction to be $N_y = N_z = N_x/10$.

In Fig. 14, we plot the median absolute deviation of the simulation result from the analytic solution. The trend of these errors is similar to the one obtained in 1D and shows that deviations get smaller for increased resolutions until they saturate at the 3-percent level. Interestingly, the pressure deviations do not differ significantly between the simulations employing the energy- or entropy-conserving scheme. However, the errors calculated for the 3D simulations are larger if we directly compare them to those obtained from the corresponding 1D shock tube at the same resolution.

4.4 Simulations of isolated galaxy formation

In this section, we continue our comparison of the energy-based method and the entropy-conserving scheme in a more realistic astrophysical application. We simulate the formation of three different isolated galaxies inside halo masses of 10^{10}, 10^{11} and $10^{12}\,{\rm M}_\odot$.

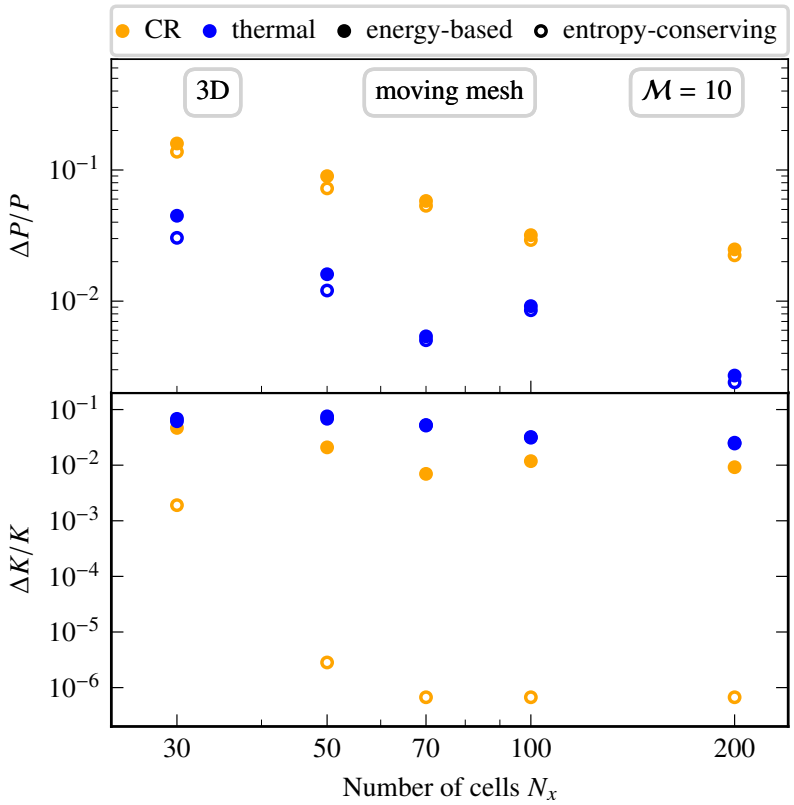

Figure 14: Same representation as in the upper left panel in Fig. 9, but with a 3D setup. N_x denotes the number of mesh cells along the x-axis, and the y and z resolutions are chosen to be $N_y = N_z = N_x/10$, respectively.

4.4.1 Simulation setup

We model the ISM by an effective pressurized EOS and follow radiative cooling and star formation using the approach by Springel and Hernquist (2003). In addition to the composite thermal and CR fluid, we evolve the magnetic field using the Powell et al. (1999) scheme for divergence control as implemented in Arepo (Pakmor and Springel, 2013). The magnetic field is initialized with a low-amplitude uniform seed magnetic field with a strength of $B = 10^{-10}\,\mathrm{G}$. The general setup is identical to the one employed by Pfrommer et al. (2017). We adopt Navarro-Frenk-White (NFW) profiles for the dark matter component (Navarro et al., 1997), which are characterized by the concentration parameter $c_{200} = r_{200}/r_\mathrm{s}$, where r_{200} denotes the radius that encloses 200 times the critical density of the universe and r_s is the characteristic radius of the NFW profile. We choose the values for c_{200} following the results presented by Macciò et al. (2008). We adopt a hydrostatic gas distribution that is initially in equilibrium within the halo. We assume that the halo carries a small amount of angular momentum, parametrized by a spin parameter $\lambda = J|E|^{1/2}\mathrm{G}^{-1}M_{200}^{-5/2}$, where J is the angular momentum, $|E|$ is the total halo energy, G is the gravitational constant and M_{200} denotes the mass within r_{200}. For each run we choose $\lambda = 0.3$ and a baryon mass fraction of $\Omega_\mathrm{b}/\Omega_\mathrm{m} = 0.155$.

In the initial conditions of our high-resolution simulations, we have $N = 10^7$ gas cells inside the virial radius. Each gas cell has a mass of $155\mathrm{M}_\odot \times M_{200}/(10^{10}\mathrm{M}_\odot)$, which also corresponds to the target mass of the cells throughout the simulation. We

Table 2: Parameters of the isolated galaxy simulations. Columns from left to right label (1) virial mass M_{200}, (2) concentration parameter of the NFW profile, (3) initial gas fraction, (4) dimensionless spin parameter, (5) CR acceleration efficiency at SNe, (6) initial number of resolution elements N within the virial radius, and (7) MVD of adjacent VCs.

M_{200}	c_{200}	$\Omega_\mathrm{b}/\Omega_\mathrm{m}$	λ	ζ_SN	N	MVD
$10^{10}\,\mathrm{M}_\odot$	11	0.155	0.3	0.1	10^7	5, 10
$10^{11}\,\mathrm{M}_\odot$	8.5	0.155	0.3	0.1	10^7	10
$10^{12}\,\mathrm{M}_\odot$	7	0.155	0.3	0.1	10^7	5, 10
$10^{12}\,\mathrm{M}_\odot$	7	0.155	0.3	0.1	10^6	10
$10^{12}\,\mathrm{M}_\odot$	7	0.155	0.3	0.1	10^5	10

enforce that the mass of all cells is within a factor of 2 of the target mass by explicitly refining and de-refining the mesh cells that violate these criteria. We additionally require that adjacent cells adhere a maximum volume difference (MVD) of 10 and refine the larger cell if this condition is violated. Furthermore, we adopt a threshold for the star-forming density of $\rho_\mathrm{sf} = 5.98 \times 10^{-3}\,\mathrm{M}_\odot\,\mathrm{pc}^{-3}$. We account for CR injection at SNe with a CR energy injection efficiency of $\zeta_\mathrm{SN} = 0.1$, indicating the fraction of SN energy that is converted into CRs. The CR injection at SNe is performed with a sub-resolution model and not with our explicit shock finding method and associated CR acceleration. For a detailed description of the sub-resolution model, we refer to Sec. 3.2 of Pfrommer et al. (2017). We assume advective CR transport and account for adiabatic changes of the CR energy as well as Coulomb and hadronic CR cooling, while neglecting active CR transport in the form of anisotropic diffusion and streaming. A summary of the simulation parameters is listed in Table 2.

4.4.2 Results

In Fig. 15, we plot the SFR (left-hand panel) and the instantaneous CR energy (right-hand panel) as a function of time for our three different haloes (shown with different line styles). Results using the energy-based method are coloured blue, those of the entropy-conserving scheme are shown with red. The $10^{10}\,\mathrm{M}_\odot$ halo shows a slightly but systematically lower SFR using the entropy-conserving scheme, which can be explained by the minor increase in the corresponding CR energy. In comparison to the energy-based method, the higher pressure induced by CRs causes the thermal gas to cool more slowly, which in turn leads to a decrease in the SFR. This effect declines with increasing halo mass, as already reported by Pfrommer et al. (2017). Hence, the same but opposite behaviour can be analogously explained for our $10^{12}\,\mathrm{M}_\odot$ halo, where the total CR energy is reduced by about 30 per cent using the entropy-conserving scheme. This leads to a small increase in SFR in the period between 0.5 and 1.2 Gyr. The halo with $10^{11}\,\mathrm{M}_\odot$ shows no differences at all, neither in SFR nor in CR energy.

We explain the behaviour for the various haloes as follows. Because the entropy-conserving scheme does not explicitly conserve CR *energy*, this scheme introduces intrinsic differences in the CR energy when we compare it to the energy-based method. Thus, the temporal evolution of the CR energy for both schemes inevitable deviates. This leads to discrepancies in the SFR, which in turn change the amount of CRs injected. Thus, a cycle of altered CR energy is created in which the injection and

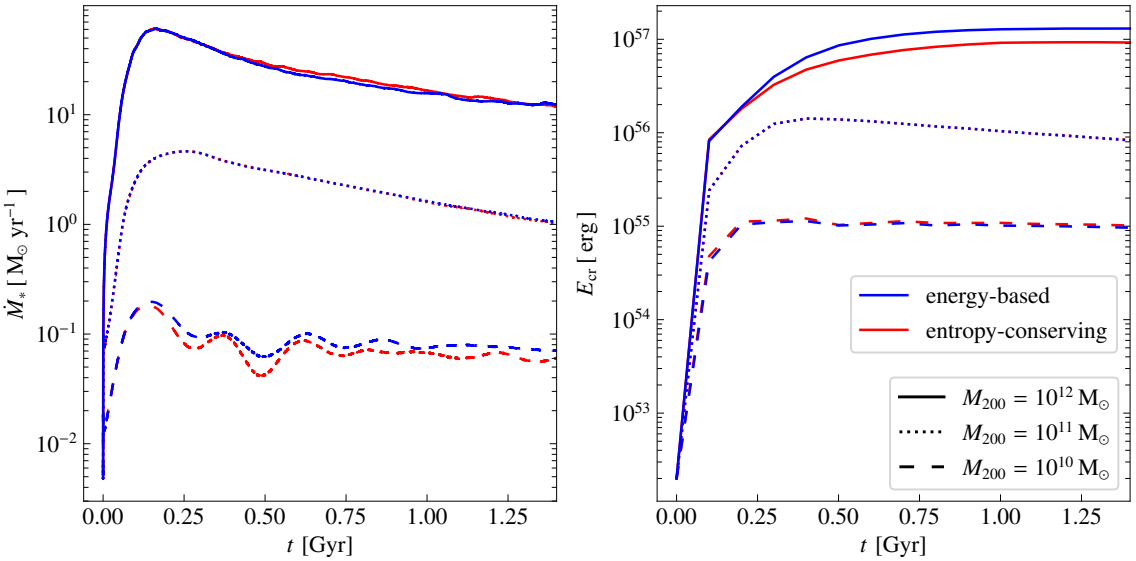

Figure 15: SFR (left-hand panel) and instantaneous CR energy (right-hand panel) as a function of time for our various haloes. Profiles for these quantities are depicted using dotted, dashed and solid lines for the haloes of mass 10^{10}, 10^{11} and $10^{12}\,\mathrm{M}_\odot$, respectively. Results using the energy-based method are coloured blue, those of the entropy-conserving scheme red.

non-conservation of CR energy influence each other through their effects on the SFR. Another point that should not be ignored is the fact that the gain and loss terms in Eqs. (83) and (86) describe variations in energy, not entropy. While the algebraic conversion of this is straightforward, the underlying physics may not be so easily transferable and should therefore be used with caution.

In Fig. 16, we show a gallery of slices that display the gas density ρ, CR energy density $\varepsilon_{\mathrm{cr}}$, and SFR for the $10^{12}\,\mathrm{M}_\odot$ halo after 1 Gyr of evolution. The top six panels depict the results using the energy-based method, the bottom six panels the results from the entropy-conserving scheme. Both numerical methods produce very similar results. At this stage of evolution, gas has rapidly accumulated in the centre of the galaxy, which leads to an increased gas density and SFR there. Most CRs are injected in this area, as confirmed by the centrally enhanced CR energy density (panels in the middle row). While the distribution of the gas density in both haloes looks almost identical, the edge-on views of $\varepsilon_{\mathrm{cr}}$ (bottom panels in the middle row) show a slightly more extended distribution of CR energy when the energy-based method is used. This is due to the increased CR pressure (or CR energy, cf. right panel in Fig. 15) providing additional pressure support. Furthermore, we notice a minor increase in SFR within a ring at about 14 to 16 kpc from the centre when using the entropy-conserving scheme. This is in agreement with a moderately reduced $\varepsilon_{\mathrm{cr}}$ in this region in comparison to the energy-based method, as discussed in the previous paragraph. However, we note that the differences are minuscule and that the overall morphological appearances of both galaxies are nearly identical, especially considering the larger astrophysical uncertainties of the adopted model parameters.

Note that recent galaxy simulations by Semenov et al. (2021) find larger differences between the entropy-conserving and energy-based methods. The main differences in comparison to our approach is their employed hydrodynamical method (a

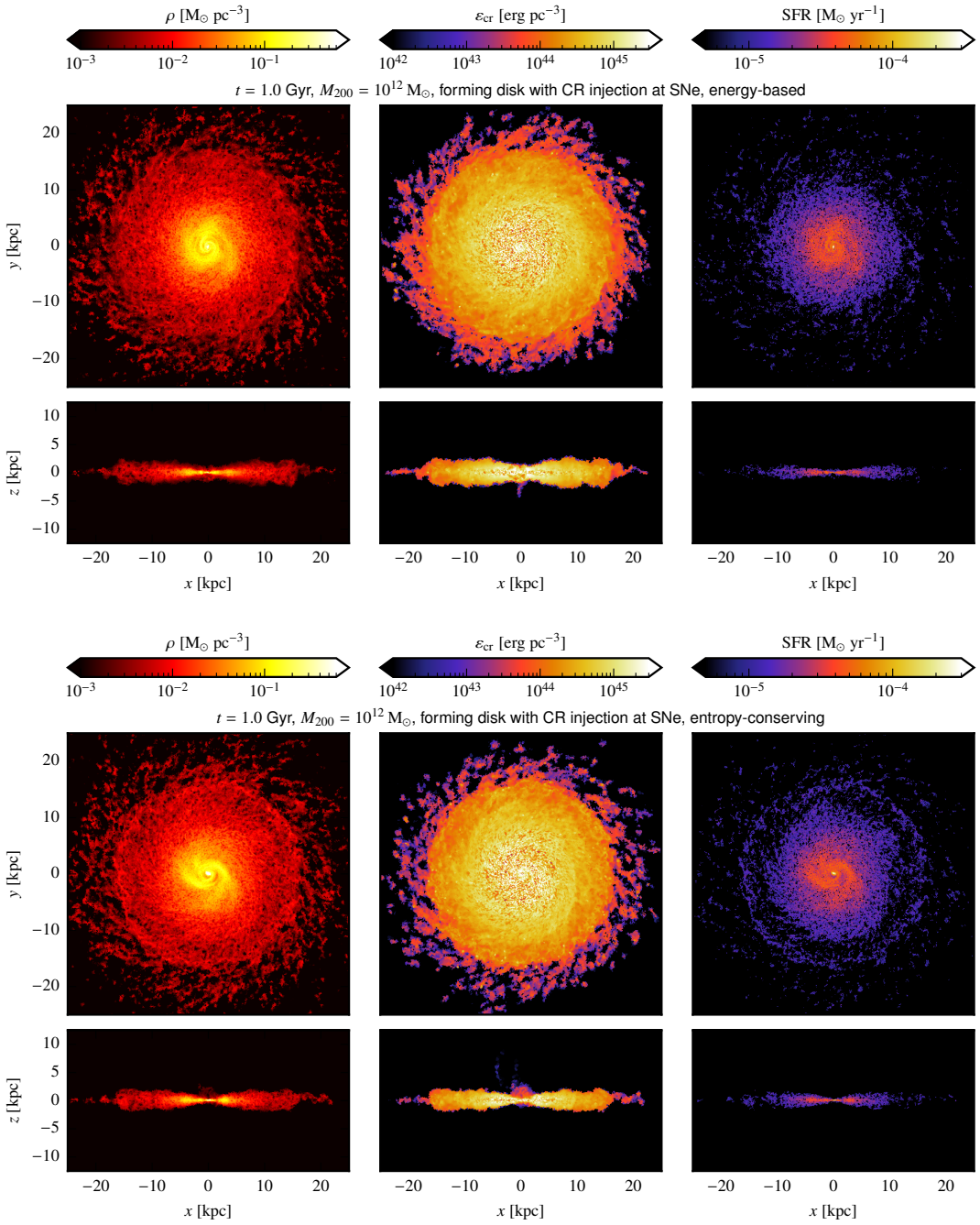

Figure 16: Slices showing the gas density ρ, CR energy density $\varepsilon_{\rm cr}$ and SFR (from left to right) for the galaxy situated in the $10^{12}\,{\rm M}_\odot$ halo after 1 Gyr of evolution. The top six panels show results obtained with the energy-based method, and the bottom six panels show the results of the simulation that employs the entropy-conserving scheme. For each quantity, we show slices through the mid-plane of the disc (face-on views) and vertical slices through the centre (edge-on views).

spatially fixed, adaptively refined mesh) and their explicitly modelled multiphase ISM, while we adopt an effective EOS that results in a smoother ISM. Semenov et al. (2021) follow the radiative cooling down to temperatures of 40 K so that energy deposition into the cooling phase by SNe result in more compressible, radiative shocks. Studying CR acceleration at radiative shocks is beyond the scope of this

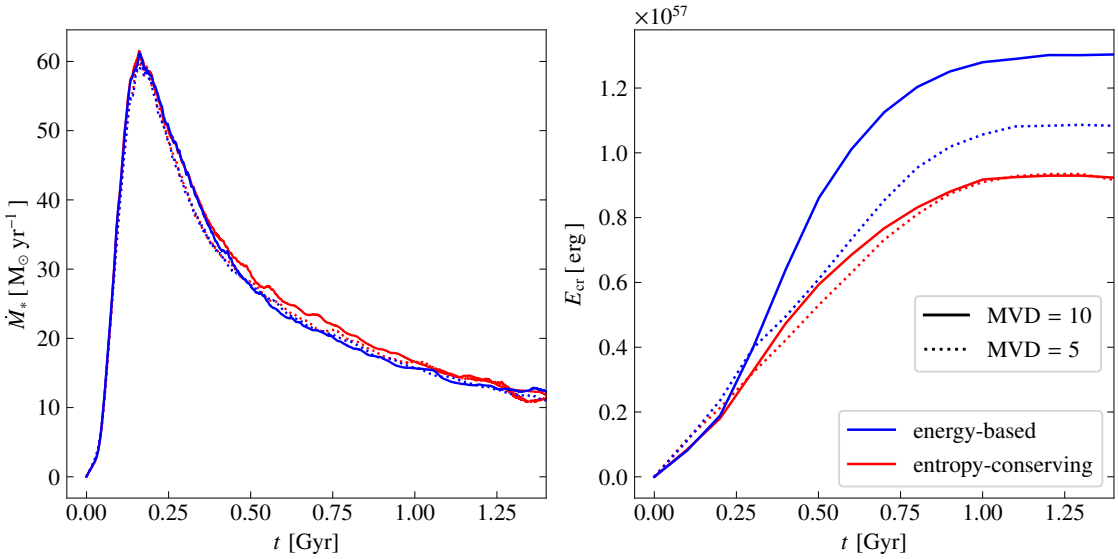

Figure 17: SFR (left panel) and instantaneous CR energy within the simulation (right panel) as a function of time for our halo with $10^{12}\,\mathrm{M}_\odot$, plotted with a linear scaling. Results using the energy-based method are coloured blue, those of the entropy-conserving scheme are shown in red. The solid lines show the results when neighbouring cells differ in volume by a maximum factor of 10, and the dotted lines show the results for an MVD of 5.

work and will be postponed to future work.

Adapting the refinement criterion As stated in Sec. 4.4.1, we limit adjacent cells to differ in volume at most by a factor of 10 in our simulations of isolated galaxies. Here, we analyse a setup where this MVD is restricted to a factor of 5, which has the effect of resolving regions of high density even more accurately. This is of particular interest in terms of star formation and CR injection.

In Fig. 17, we plot the SFR (left-hand panel) and instantaneous CR energy (right-hand panel) of the $10^{12}\,\mathrm{M}_\odot$ halo and compare simulations with the fiducial and the more restrictive value for the MVD. Results using the energy-based method are coloured blue, those of the entropy-conserving scheme are shown in red. Solid (dotted) lines indicate the previous results using an MVD of 10 (5). Both methods yield a very similar SFR. The instantaneous CR energy echoes this finding, with the more restrictive MVD simulations to differ at most by less than 20 percent. Analogously, we adapt the refinement criterion for the $10^{10}\,\mathrm{M}_\odot$ halo, but notice no change from our fiducial case with an MVD of 10.

Convergence behaviour of numerical schemes Here we analyse the convergence behaviour of the energy-based and entropy-conserving methods as a function of resolution. To this end, we show the total CR energy of our $10^{12}\,\mathrm{M}_\odot$ halo in Fig. 18 and plot the results for initial resolutions of 10^5, 10^6, and 10^7 grid cells as dotted, dashed, and solid lines, respectively. Results using the energy-based method are coloured blue, results of the entropy-conserving scheme with red. We use an MVD of 10 in each case. Either method converges with an increasing number of mesh cells, albeit to different values, with the discrepancy between the two schemes decreasing with increasing resolution.

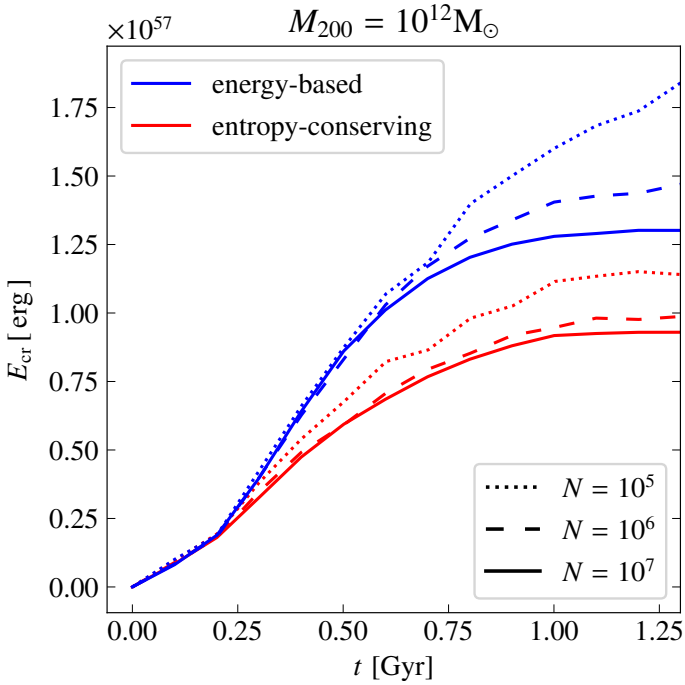

Figure 18: Total instantaneous CR energy as a function of time for different resolutions of the isolated galaxy simulations. Results using the energy-based method are coloured blue, outcomes of the entropy-conserving scheme red. Results of the runs with a resolution of 10^5, 10^6 and 10^7 mesh cells are shown as dotted, dashed and solid lines, respectively.

5 Conclusions

Here, we study various approaches to integrate CRs into MHD simulations, namely the energy-based method and the entropy-conserving scheme, in the context of the moving-mesh code Arepo. To this end, we perform a sequence of 1D shock-tube tests, with and without accounting for CR acceleration at shocks, as well as using a static-mesh and a moving-mesh setup. This allows us to analyse the idealized behaviour of CRs under the influence of adiabatic and non-adiabatic changes using different numerical schemes, in addition to comparing the performance of the two mesh approaches. Moreover, we use both numerical methods to simulate the influence of CRs on the formation of several isolated galaxies in haloes of mass 10^{10}, 10^{11} and $10^{12}\,\mathrm{M}_\odot$ including advective CR transport and feedback in terms of CR injection by SNe. We find that:

- The moving-mesh approach performs significantly better than the static-mesh setup, which is due to the comparably high numerical diffusivity of the latter. This is true regardless of the method used to integrate the CRs (see Fig. 9).
- At *very high resolution*, the entropy-conserving scheme has a lower error in CR energy by a factor of 10 when omitting CR acceleration (cf. top row in Fig. 9) and by a factor of 2 when accounting for CR acceleration at shocks (see Fig. 13). However, the overall error remains small (less than 2 per cent and 6 per cent, respectively) for the energy-based method and hence far below astrophysical uncertainties.
- At *low resolution*, which is more typical for astrophysical large-scale simulations, both numerical schemes perform almost identical in terms of CR and thermal energy in a setup without CR acceleration (see Fig. 9). When considering CR acceleration at the shock, the energy-based method proves to be numerically much more stable (see Fig. 11) and thus shows significantly lower deviations from the analytic solutions, particularly in CR entropy (see Fig. 13).
- The shock velocity is determined significantly more accurately using the energy-based method when CR acceleration at the shock is considered, particularly at low and intermediate resolutions where deviations are reduced by a factor of 5 to 6 in comparison to the entropy-conserving scheme (see Fig. 12).
- The simulations of isolated galaxies yield almost identical results using either numerical method (see Fig. 16). The small variations in SFR and instantaneous CR energy (see Fig. 15) can be explained by the intrinsic behaviour of the entropy-conserving scheme, where energy is not explicitly conserved.

In this work, we have demonstrated that the integration of CRs into MHD simulations using a moving-mesh approach can be properly achieved with either the energy-based method or the entropy-conserving scheme, as long as active CR acceleration at shocks is omitted. When the latter is considered, the energy-based method is the preferred choice, in particular for poorly resolved simulations.

References

H. Alfvén. Existence of Electromagnetic-Hydrodynamic Waves. *Nature*, 150(3805): 405–406, Oct. 1942. doi: 10.1038/150405d0. URL https://ui.adsabs.harvard.edu/abs/1942Natur.150..405A.

A. R. Bell. The acceleration of cosmic rays in shock fronts - I. *MNRAS*, 182:147–156, Jan. 1978. doi: 10.1093/mnras/182.2.147. URL https://ui.adsabs.harvard.edu/abs/1978MNRAS.182..147B.

R. D. Blandford and J. P. Ostriker. Particle acceleration by astrophysical shocks. *ApJL*, 221:L29–L32, Apr. 1978. doi: 10.1086/182658. URL https://ui.adsabs.harvard.edu/abs/1978ApJ...221L..29B.

C. M. Booth, O. Agertz, A. V. Kravtsov, and N. Y. Gnedin. SIMULATIONS OF DISK GALAXIES WITH COSMIC RAY DRIVEN GALACTIC WINDS. *ApJ*, 777(1):L16, oct 2013. doi: 10.1088/2041-8205/777/1/l16. URL https://doi.org/10.1088/2041-8205/777/1/l16.

A. Boulares and D. P. Cox. Galactic Hydrostatic Equilibrium with Magnetic Tension and Cosmic-Ray Diffusion. *ApJ*, 365:544, Dec. 1990. doi: 10.1086/169509. URL https://ui.adsabs.harvard.edu/abs/1990ApJ...365..544B.

D. Caprioli and A. Spitkovsky. Simulations of Ion Acceleration at Non-relativistic Shocks. I. Acceleration Efficiency. *Astrophysical Journal*, 783(2):91, Mar. 2014. doi: 10.1088/0004-637X/783/2/91.

T. K. Chan, D. Kereš, P. F. Hopkins, E. Quataert, K.-Y. Su, C. C. Hayward, and C.-A. Faucher-Giguère. Cosmic ray feedback in the FIRE simulations: constraining cosmic ray propagation with GeV γ-ray emission. *MNRAS*, 488(3):3716–3744, 07 2019. ISSN 0035-8711. doi: 10.1093/mnras/stz1895. URL https://doi.org/10.1093/mnras/stz1895.

A. J. Chorin. Random Choice Solution of Hyperbolic Systems. *Journal of Computational Physics*, 22(4):517–533, Dec. 1976. doi: 10.1016/0021-9991(76)90047-4.

L. O. Drury. REVIEW ARTICLE: An introduction to the theory of diffusive shock acceleration of energetic particles in tenuous plasmas. *Reports on Progress in Physics*, 46(8):973–1027, Aug. 1983. doi: 10.1088/0034-4885/46/8/002.

Y. Dubois, B. Commerçon, A. Marcowith, and L. Brahimi. Shock-accelerated cosmic rays and streaming instability in the adaptive mesh refinement code Ramses. *A&A*, 631:A121, Nov. 2019. doi: 10.1051/0004-6361/201936275. URL https://ui.adsabs.harvard.edu/abs/2019A&A...631A.121D.

B. Einfeldt. On godunov-type methods for gas dynamics. *SIAM Journal on Numerical Analysis*, 25(2):294–318, 1988. doi: 10.1137/0725021. URL https://doi.org/10.1137/0725021.

B. Einfeldt, P. L. Roe, C. D. Munz, and B. Sjogreen. On Godunov-Type Methods near Low Densities. *Journal of Computational Physics*, 92(2):273–295, Feb. 1991. doi: 10.1016/0021-9991(91)90211-3.

T. A. Enßlin, C. Pfrommer, V. Springel, and M. Jubelgas. Cosmic ray physics in calculations of cosmological structure formation. *A&A*, 473(1):41–57, Oct. 2007. doi: 10.1051/0004-6361:20065294. URL https://ui.adsabs.harvard.edu/abs/2007A&A...473...41E.

A. J. Farmer and P. Goldreich. Wave Damping by Magnetohydrodynamic Turbulence and Its Effect on Cosmic-Ray Propagation in the Interstellar Medium. *ApJ*, 604(2):671–674, Apr. 2004. doi: 10.1086/382040. URL https://ui.adsabs.harvard.edu/abs/2004ApJ...604..671F.

E. Fermi. On the Origin of the Cosmic Radiation. *Physical Review*, 75(8):1169–1174, Apr. 1949. doi: 10.1103/PhysRev.75.1169. URL https://ui.adsabs.harvard.edu/abs/1949PhRv...75.1169F.

P. Girichidis, T. Naab, S. Walch, and M. Hanasz. Anisotropic transport and early dynamical impact of Cosmic Rays around Supernova remnants. *arXiv e-prints*, art. arXiv:1406.4861, June 2014. URL https://ui.adsabs.harvard.edu/abs/2014arXiv1406.4861G.

P. Girichidis, C. Pfrommer, M. Hanasz, and T. Naab. Spectrally resolved cosmic ray hydrodynamics - I. Spectral scheme. *MNRAS*, 491(1):993–1007, Jan. 2020. doi: 10.1093/mnras/stz2961. URL https://ui.adsabs.harvard.edu/abs/2020MNRAS.491..993G.

S. K. Godunov and I. Bohachevsky. Finite difference method for numerical computation of discontinuous solutions of the equations of fluid dynamics. *Matematičeskij sbornik*, 47(89)(3):271–306, 1959. URL https://hal.archives-ouvertes.fr/hal-01620642.

S. K. Godunov, A. V. Zabrodin, M. I. Ivanov, A. N. Kraiko, and G. P. Prokopov. Numerical solution of multidimensional problems of gas dynamics. *Moscow Izdatel Nauka*, Jan. 1976.

T. I. Gombosi. *Physics of the Space Environment*. Cambridge Atmospheric and Space Science Series, 2004. ISBN 9780521607681. URL https://ui.adsabs.harvard.edu/abs/2004pse..book.....G.

R. J. Gould. Energy loss of a relativistic ion in a plasma. *Physica*, 58(3):379–383, Apr. 1972. doi: 10.1016/0031-8914(72)90159-0. URL https://ui.adsabs.harvard.edu/abs/1972Phy....58..379G.

F. Guo and S. P. Oh. Feedback heating by cosmic rays in clusters of galaxies. *MNRAS*, 384(1):251–266, Feb. 2008. doi: 10.1111/j.1365-2966.2007.12692.x. URL https://ui.adsabs.harvard.edu/abs/2008MNRAS.384..251G.

S. Gupta, P. Sharma, and A. Mignone. A numerical approach to the non-uniqueness problem of cosmic ray two-fluid equations at shocks. *MNRAS*, 502(2):2733–2749, 01 2021. ISSN 0035-8711. doi: 10.1093/mnras/stab142. URL https://doi.org/10.1093/mnras/stab142.

M. Hanasz and H. Lesch. Incorporation of cosmic ray transport into the ZEUS MHD code. Application for studies of Parker instability in the ISM. *A&A*, 412:331–339, Dec. 2003. doi: 10.1051/0004-6361:20031433. URL https://ui.adsabs.harvard.edu/abs/2003A&A...412..331H.

A. Harten, P. D. Lax, and B. v. Leer. On upstream differencing and godunov-type schemes for hyperbolic conservation laws. *SIAM Review*, 25(1):35–61, 1983. doi: 10.1137/1025002. URL https://doi.org/10.1137/1025002.

P. F. Hopkins, J. Squire, and I. S. Butsky. A consistent reduced-speed-of-light formulation of cosmic ray transport valid in weak- and strong-scattering regimes. *MNRAS*, 509(3):3779–3797, Jan. 2022. doi: 10.1093/mnras/stab2635. URL https://ui.adsabs.harvard.edu/abs/2022MNRAS.509.3779H.

S. Jacob and C. Pfrommer. Cosmic ray heating in cool core clusters - I. Diversity of steady state solutions. *MNRAS*, 467(2):1449–1477, May 2017a. doi: 10.1093/mnras/stx131. URL https://ui.adsabs.harvard.edu/abs/2017MNRAS.467.1449J.

S. Jacob and C. Pfrommer. Cosmic ray heating in cool core clusters - II. Self-regulation cycle and non-thermal emission. *MNRAS*, 467(2):1478–1495, May 2017b. doi: 10.1093/mnras/stx132. URL https://ui.adsabs.harvard.edu/abs/2017MNRAS.467.1478J.

Y.-F. Jiang and S. P. Oh. A New Numerical Scheme for Cosmic-Ray Transport. *ApJ*, 854(1):5, Feb. 2018. doi: 10.3847/1538-4357/aaa6ce. URL https://ui.adsabs.harvard.edu/abs/2018ApJ...854....5J.

J. R. Jokipii. Cosmic-Ray Propagation. I. Charged Particles in a Random Magnetic Field. *ApJ*, 146:480, Nov. 1966. doi: 10.1086/148912. URL https://ui.adsabs.harvard.edu/abs/1966ApJ...146..480J.

M. Jubelgas, V. Springel, T. Enßlin, and C. Pfrommer. Cosmic ray feedback in hydrodynamical simulations of galaxy formation. *A&A*, 481(1):33–63, Apr. 2008. doi: 10.1051/0004-6361:20065295. URL https://ui.adsabs.harvard.edu/abs/2008A&A...481...33J.

A. J. Klimas and G. Sandri. Foundation of the Theory of Cosmic-Ray Transport in Random Magnetic Fields. *ApJL*, 169:41, Oct. 1971. doi: 10.1086/151116. URL https://ui.adsabs.harvard.edu/abs/1971ApJ...169...41K.

P. Kroupa. On the variation of the initial mass function. *MNRAS*, 322(2):231–246, Apr. 2001. doi: 10.1046/j.1365-8711.2001.04022.x. URL https://ui.adsabs.harvard.edu/abs/2001MNRAS.322..231K.

Y. Kudoh and T. Hanawa. Approximate Riemann solvers for the cosmic ray magnetohydrodynamical equations. *MNRAS*, 462(4):4517–4531, Nov. 2016. doi: 10.1093/mnras/stw1937. URL https://ui.adsabs.harvard.edu/abs/2016MNRAS.462.4517K.

R. Kulsrud and W. P. Pearce. The Effect of Wave-Particle Interactions on the Propagation of Cosmic Rays. *ApJ*, 156:445, May 1969. doi: 10.1086/149981. URL https://ui.adsabs.harvard.edu/abs/1969ApJ...156..445K.

E. Landau, L.D.; Lifschitz. *Fluid Mechanics : Volume 6*. Elsevier Science & Technology, 1987. ISBN 9780080570730. URL http://ebookcentral.proquest.com/lib/potsdamuni/detail.action?docID=4088285.

A. V. Macciò, A. A. Dutton, and F. C. Van Den Bosch. Concentration, spin and shape of dark matter haloes as a function of the cosmological model: WMAP1, WMAP3 and WMAP5 results. *MNRAS*, 391(4):1940–1954, 12 2008. ISSN 0035-8711. doi: 10.1111/j.1365-2966.2008.14029.x. URL https://doi.org/10.1111/j.1365-2966.2008.14029.x.

K. Mannheim and R. Schlickeiser. Interactions of cosmic ray nuclei. *A&A*, 286:983–996, June 1994. URL https://ui.adsabs.harvard.edu/abs/1994A&A...286..983M.

A. Marcowith, A. Bret, A. Bykov, M. E. Dieckman, L. O'C Drury, B. Lembège, M. Lemoine, G. Morlino, G. Murphy, G. Pelletier, I. Plotnikov, B. Reville, M. Riquelme, L. Sironi, and A. Stockem Novo. The microphysics of collisionless shock waves. *Reports on Progress in Physics*, 79(4):046901, Apr. 2016. doi: 10.1088/0034-4885/79/4/046901. URL https://ui.adsabs.harvard.edu/abs/2016RPPh...79d6901M.

F. Miniati. Cosmocr: A numerical code for cosmic ray studies in computational cosmology. *Computer Physics Communications*, 141(1):17–38, 2001. ISSN 0010-4655. doi: https://doi.org/10.1016/S0010-4655(01)00293-4. URL https://www.sciencedirect.com/science/article/pii/S0010465501002934.

T. Miyoshi and K. Kusano. A multi-state HLL approximate Riemann solver for ideal magnetohydrodynamics. *Journal of Computational Physics*, 208(1):315–344, Sept. 2005. doi: 10.1016/j.jcp.2005.02.017.

J. F. Navarro, C. S. Frenk, and S. D. M. White. A Universal Density Profile from Hierarchical Clustering. *ApJ*, 490(2):493–508, Dec. 1997. doi: 10.1086/304888. URL https://ui.adsabs.harvard.edu/abs/1997ApJ...490..493N.

M. A. Ogrodnik, M. Hanasz, and D. Wóltański. Implementation of Cosmic Ray Energy Spectrum (CRESP) Algorithm in PIERNIK MHD Code. I. Spectrally Resolved Propagation of Cosmic Ray Electrons on Eulerian Grids. *ApJS*, 253(1):18, Mar. 2021. doi: 10.3847/1538-4365/abd16f. URL https://ui.adsabs.harvard.edu/abs/2021ApJS..253...18O.

R. Pakmor and V. Springel. Simulations of magnetic fields in isolated disc galaxies. *MNRAS*, 432(1):176–193, June 2013. doi: 10.1093/mnras/stt428. URL https://ui.adsabs.harvard.edu/abs/2013MNRAS.432..176P.

R. Pakmor, A. Bauer, and V. Springel. Magnetohydrodynamics on an unstructured moving grid. *MNRAS*, 418(2):1392–1401, Dec. 2011. doi: 10.1111/j.1365-2966.2011.19591.x. URL https://ui.adsabs.harvard.edu/abs/2011MNRAS.418.1392P.

R. Pakmor, C. Pfrommer, C. M. Simpson, R. Kannan, and V. Springel. Semi-implicit anisotropic cosmic ray transport on an unstructured moving mesh. *MNRAS*, 462 (3):2603–2616, 07 2016a. ISSN 0035-8711. doi: 10.1093/mnras/stw1761. URL https://doi.org/10.1093/mnras/stw1761.

R. Pakmor, V. Springel, A. Bauer, P. Mocz, D. J. Munoz, S. T. Ohlmann, K. Schaal, and C. Zhu. Improving the convergence properties of the moving-mesh code AREPO. *MNRAS*, 455(1):1134–1143, 11 2016b. ISSN 0035-8711. doi: 10.1093/mnras/stv2380. URL https://doi.org/10.1093/mnras/stv2380.

C. Pfrommer. Lecture notes on "The Physics of Galaxy Clusters", 2022a. URL https://pages.aip.de/pfrommer/Lectures/clusters.pdf.

C. Pfrommer. Lecture notes on "Modern Computational Astrophysics: Concepts and Applications", 2022b. URL https://pages.aip.de/pfrommer/Lectures/computational_astrophysics.html.

C. Pfrommer, V. Springel, T. A. Enßlin, and M. Jubelgas. Detecting shock waves in cosmological smoothed particle hydrodynamics simulations. *MNRAS*, 367(1): 113–131, 03 2006. ISSN 0035-8711. doi: 10.1111/j.1365-2966.2005.09953.x. URL https://doi.org/10.1111/j.1365-2966.2005.09953.x.

C. Pfrommer, R. Pakmor, K. Schaal, C. M. Simpson, and V. Springel. Simulating cosmic ray physics on a moving mesh. *MNRAS*, 465(4):4500–4529, Mar. 2017. doi: 10.1093/mnras/stw2941. URL https://ui.adsabs.harvard.edu/abs/2017MNRAS.465.4500P.

K. G. Powell, P. L. Roe, T. J. Linde, T. I. Gombosi, and D. L. De Zeeuw. A Solution-Adaptive Upwind Scheme for Ideal Magnetohydrodynamics. *Journal of Computational Physics*, 154(2):284–309, Sept. 1999. doi: 10.1006/jcph.1999.6299. URL https://ui.adsabs.harvard.edu/abs/1999JCoPh.154..284P.

J. E. Pringle and A. King. *Astrophysical Flows*. , 2007. URL https://ui.adsabs.harvard.edu/abs/2007asfl.book.....P.

A. K. Raychaudhuri. *Classical Theory of Electricity and Magnetism*. 2366-8857. Springer Singapore, 2022. ISBN 978-981-16-8139-4. doi: https://doi.org/10.1007/978-981-16-8139-4.

L. F. S. Rodrigues, A. P. Snodin, G. R. Sarson, and A. Shukurov. Fickian and non-Fickian diffusion of cosmic rays. *MNRAS*, 487(1):975–980, July 2019. doi: 10.

1093/mnras/stz1354. URL https://ui.adsabs.harvard.edu/abs/2019MNRAS.487..975R.

P. L. Roe and D. S. Balsara. Notes on the eigensystem of magnetohydrodynamics. *SIAM Journal on Applied Mathematics*, 56(1):57–67, 1996. ISSN 00361399. URL http://www.jstor.org/stable/2102521.

D. Ryu, J. P. Ostriker, H. Kang, and R. Cen. A Cosmological Hydrodynamic Code Based on the Total Variation Diminishing Scheme. *ApJ*, 414:1, Sept. 1993. doi: 10.1086/173051. URL https://ui.adsabs.harvard.edu/abs/1993ApJ...414...1R.

M. Salem and G. L. Bryan. Cosmic ray driven outflows in global galaxy disc models. *MNRAS*, 437(4):3312–3330, Feb. 2014. doi: 10.1093/mnras/stt2121. URL https://ui.adsabs.harvard.edu/abs/2014MNRAS.437.3312S.

K. Schaal and V. Springel. Shock finding on a moving mesh – I. Shock statistics in non-radiative cosmological simulations. *MNRAS*, 446(4):3992–4007, 12 2015. ISSN 0035-8711. doi: 10.1093/mnras/stu2386. URL https://doi.org/10.1093/mnras/stu2386.

R. Schlickeiser. *Cosmic Ray Astrophysics*. , 2002. URL https://ui.adsabs.harvard.edu/abs/2002cra..book.....S.

R. Schlickeiser and F. Jenko. Cosmic ray transport in non-uniform magnetic fields: consequences of gradient and curvature drifts†. *Journal of Plasma Physics*, 76:317–327, Aug. 2010. doi: 10.1017/S0022377809990444. URL https://ui.adsabs.harvard.edu/abs/2010JPlPh..76..317S.

V. A. Semenov, A. V. Kravtsov, and B. Diemer. Entropy-Conserving Scheme for Modeling Nonthermal Energies in Fluid Dynamics Simulations. *arXiv e-prints*, art. arXiv:2107.14240, July 2021. URL https://ui.adsabs.harvard.edu/abs/2021arXiv210714240S.

M. Shalaby, T. Thomas, and C. Pfrommer. A New Cosmic-Ray-driven Instability. *ApJ*, 908(2):206, Feb. 2021. doi: 10.3847/1538-4357/abd02d. URL https://ui.adsabs.harvard.edu/abs/2021ApJ...908..206S.

A. Shalchi. *Nonlinear Cosmic Ray Diffusion Theories*, volume 362. Astrophysics and Space Science Library, 2009. doi: 10.1007/978-3-642-00309-7. URL https://ui.adsabs.harvard.edu/abs/2009ASSL..362.....S.

A. Shalchi and I. Kourakis. Analytical description of stochastic field-line wandering in magnetic turbulence. *Physics of Plasmas*, 14(9):092903–092903, Sept. 2007. doi: 10.1063/1.2776905. URL https://ui.adsabs.harvard.edu/abs/2007PhPl...14i2903S.

P. Sharma, P. Colella, and D. F. Martin. Numerical Implementation of Streaming Down the Gradient: Application to Fluid Modeling of Cosmic Rays and Saturated Conduction. *arXiv e-prints*, art. arXiv:0909.5426, Sept. 2009. URL https://ui.adsabs.harvard.edu/abs/2009arXiv0909.5426S.

J. Skilling. Cosmic Rays in the Galaxy: Convection or Diffusion? *ApJ*, 170:265, Dec. 1971. doi: 10.1086/151210. URL https://ui.adsabs.harvard.edu/abs/1971ApJ...170..265S.

J. Skilling. Cosmic ray streaming - I. Effect of Alfvén waves on particles. *MNRAS*, 172:557–566, Sept. 1975. doi: 10.1093/mnras/172.3.557. URL https://ui.adsabs.harvard.edu/abs/1975MNRAS.172..557S.

V. Springel. E pur si muove: Galilean-invariant cosmological hydrodynamical simulations on a moving mesh. *MNRAS*, 401(2):791–851, Jan. 2010. doi: 10.1111/j.1365-2966.2009.15715.x. URL https://ui.adsabs.harvard.edu/abs/2010MNRAS.401..791S.

V. Springel and L. Hernquist. Cosmological smoothed particle hydrodynamics simulations: a hybrid multiphase model for star formation. *MNRAS*, 339(2):289–311, Feb. 2003. doi: 10.1046/j.1365-8711.2003.06206.x. URL https://ui.adsabs.harvard.edu/abs/2003MNRAS.339..289S.

P. A. Sturrock. *Plasma Physics, An Introduction to the Theory of Astrophysical, Geophysical and Laboratory Plasmas*. 1994.

K. Takahashi, S. Yamada, and Yamada. Exact Riemann solver for ideal magnetohydrodynamics that can handle all types of intermediate shocks and switch-on/off waves. *Journal of Plasma Physics*, 80(2):255–287, Apr. 2014. doi: 10.1017/S0022377813001268.

T. Thomas and C. Pfrommer. Cosmic-ray hydrodynamics: Alfvén-wave regulated transport of cosmic rays. *MNRAS*, 485(3):2977–3008, May 2019. doi: 10.1093/mnras/stz263. URL https://ui.adsabs.harvard.edu/abs/2019MNRAS.485.2977T.

T. Thomas and C. Pfrommer. Comparing different closure relations for cosmic ray hydrodynamics. *MNRAS*, 509(4):4803–4816, Feb. 2022. doi: 10.1093/mnras/stab3079. URL https://ui.adsabs.harvard.edu/abs/2022MNRAS.509.4803T.

T. Thomas, C. Pfrommer, and T. Enßlin. Probing Cosmic-Ray Transport with Radio Synchrotron Harps in the Galactic Center. *ApJL*, 890(2):L18, Feb. 2020. doi: 10.3847/2041-8213/ab7237. URL https://ui.adsabs.harvard.edu/abs/2020ApJ...890L..18T.

T. Thomas, C. Pfrommer, and R. Pakmor. A finite volume method for two-moment cosmic ray hydrodynamics on a moving mesh. *MNRAS*, 503(2):2242–2264, May 2021. doi: 10.1093/mnras/stab397. URL https://ui.adsabs.harvard.edu/abs/2021MNRAS.503.2242T.

E. F. Toro. *Riemann Solvers and Numerical Methods for Fluid Dynamics*. Springer-Verlag Berlin Heidelberg, 3 edition, 2009. doi: https://doi.org/10.1007/b79761.

E. F. Toro, M. Spruce, and W. Speares. Restoration of the contact surface in the HLL-Riemann solver. *Shock Waves*, 4(1):25–34, July 1994. doi: 10.1007/BF01414629.

M. Torrilhon, E. T. Hochschule, and M. Torrilhon. Exact solver and uniqueness conditions for riemann problems of ideal magnetohydrodynamics. research report 2002-06, eidgenössische technische hochschule, seminar für angewandte mathematik, 2002.

B. Vaidya, A. Mignone, G. Bodo, P. Rossi, and S. Massaglia. A Particle Module for the PLUTO Code. II. Hybrid Framework for Modeling Nonthermal Emission from Relativistic Magnetized Flows. *ApJ*, 865(2):144, Oct. 2018. doi: 10.3847/1538-4357/aadd17. URL https://ui.adsabs.harvard.edu/abs/2018ApJ...865..144V.

B. van Leer. Towards the Ultimate Conservative Difference Scheme. V. A Second-Order Sequel to Godunov's Method. *Journal of Computational Physics*, 32(1): 101–136, July 1979. doi: 10.1016/0021-9991(79)90145-1.

M. Vogelsberger, D. Sijacki, D. Kereš, V. Springel, and L. Hernquist. Moving mesh cosmology: numerical techniques and global statistics. *MNRAS*, 425(4):3024–3057, 10 2012. ISSN 0035-8711. doi: 10.1111/j.1365-2966.2012.21590.x. URL https://doi.org/10.1111/j.1365-2966.2012.21590.x.

H. J. Volk and J. F. McKenzie. Characteristics of cosmic ray shocks in the presence of wave dissipation. In *International Cosmic Ray Conference*, volume 9 of *International Cosmic Ray Conference*, pages 246–249, Jan. 1981. URL https://ui.adsabs.harvard.edu/abs/1981ICRC....9..246V.

M. Weber, T. Thomas, and C. Pfrommer. Comparing energy and entropy formulations for cosmic ray hydrodynamics. *arXiv e-prints*, art. arXiv:2205.12288, May 2022. URL https://ui.adsabs.harvard.edu/abs/2022arXiv220512288W.

R. Weinberger, V. Springel, and R. Pakmor. The AREPO Public Code Release. *ApJS*, 248(2):32, June 2020. doi: 10.3847/1538-4365/ab908c. URL https://ui.adsabs.harvard.edu/abs/2020ApJS..248...32W.

G. Winner, C. Pfrommer, P. Girichidis, and R. Pakmor. Evolution of cosmic ray electron spectra in magnetohydrodynamical simulations. *MNRAS*, 488(2):2235–2252, Sept. 2019. doi: 10.1093/mnras/stz1792. URL https://ui.adsabs.harvard.edu/abs/2019MNRAS.488.2235W.

H. Yan and A. Lazarian. Cosmic Ray Transport Through Gyroresonance Instability in Compressible Turbulence. *ApJ*, 731(1):35, Apr. 2011. doi: 10.1088/0004-637X/731/1/35. URL https://ui.adsabs.harvard.edu/abs/2011ApJ...731...35Y.

H. Y. K. Yang and M. Ruszkowski. The Spatially Uniform Spectrum of the Fermi Bubbles: The Leptonic Active Galactic Nucleus Jet Scenario. *ApJ*, 850(1):2, Nov. 2017. doi: 10.3847/1538-4357/aa9434. URL https://ui.adsabs.harvard.edu/abs/2017ApJ...850....2Y.

G. P. Zank. *Transport Processes in Space Physics and Astrophysics*, volume 877. "", 2014. doi: 10.1007/978-1-4614-8480-6. URL https://ui.adsabs.harvard.edu/abs/2014LNP...877.....Z.

G. P. Zank, J. Y. Lu, W. K. M. Rice, and G. M. Webb. Transport of energetic charged particles in a radial magnetic field. Part 1. Large-angle scattering. *Journal of Plasma Physics*, 64(4):507–541, Nov. 2000. doi: 10.1017/S0022377800008709. URL https://ui.adsabs.harvard.edu/abs/2000JPlPh..64..507Z.

E. G. Zweibel. The microphysics and macrophysics of cosmic rays. *Physics of Plasmas*, 20(5):055501, May 2013. doi: 10.1063/1.4807033. URL https://ui.adsabs.harvard.edu/abs/2013PhPl...20e5501Z.

E. G. Zweibel. The basis for cosmic ray feedback: Written on the wind. *Physics of Plasmas*, 24(5):055402, May 2017. doi: 10.1063/1.4984017. URL https://ui.adsabs.harvard.edu/abs/2017PhPl...24e5402Z.

Declaration of Authorship

I hereby certify that I have written this thesis independently and that I have not used any sources or auxiliaries other than those indicated.

Matthias Weber